VTRC
Virginia Transportation
Research Council

We Bring Innovation to Transportation

Implementation of a Precast Inverted T-Beam System in Virginia:
Part II: Analytic and Field Investigations

http://www.virginiadot.org/vtrc/main/online_reports/pdf/19-r2.pdf

FATMIR MENKULASI, Ph.D., P.E.
Assistant Professor
Department of Civil and Environmental Engineering
Wayne State University

THOMAS COUSINS, Ph.D., P.E.
Professor
Glenn Department of Civil Engineering
Clemson University

C.L. ROBERTS-WOLLMANN, Ph.D., P.E.
Professor
Via Department of Civil and Environmental Engineering
Virginia Polytechnic Institute and State University

Final Report VTRC 19-R2

VIRGINIA TRANSPORTATION RESEARCH COUNCIL
530 Edgemont Road, Charlottesville, VA 22903-2454
vtrc.virginiadot.org

Standard Title Page - Report on Federally Funded Project

1. Report No.: FHWA/VTRC 19-R2	2. Government Accession No.:	3. Recipient's Catalog No.:

4. Title and Subtitle: Implementation of a Precast Inverted T-Beam System in Virginia: Part II: Analytic and Field Investigations	5. Report Date: August 2018 6. Performing Organization Code:
7. Author(s): Fatmir Menkulasi, Ph.D., P.E., Thomas Cousins, Ph.D., P.E., and C.L. Roberts-Wollmann, Ph.D., P.E.	8. Performing Organization Report No.: VTRC 19-R2
9. Performing Organization and Address: The Charles E. Via, Jr. Department of Civil and Environmental Engineering Virginia Polytechnic Institute and State University Blacksburg, VA	10. Work Unit No. (TRAIS): 11. Contract or Grant No.: 101740
12. Sponsoring Agencies' Name and Address: Virginia Department of Transportation, 1401 E. Broad Street, Richmond, VA 23219 Federal Highway Administration, 400 North 8th Street, Room 750, Richmond, VA 23219-4825	13. Type of Report and Period Covered: Final Contract 14. Sponsoring Agency Code:

15. Supplementary Notes:

16. Abstract:

The inverted T-beam superstructure is a bridge system that provides an accelerated construction alternative for short-to-medium-span bridges. The system consists of adjacent precast inverted T-beams with a cast-in-place concrete topping. This bridge system is expected to not experience the reflective cracking problems manifested in short-to-medium-span bridges constructed with traditional adjacent voided slab or adjacent box beams. This report presents the results of three phases of a comprehensive research project to develop and implement an inverted T-beam system for Virginia. The three phases are: investigation of time-dependent and temperature effects, investigation of end zone stresses, and live load testing.

The first investigation is of time-dependent effects in composite bridges with precast inverted T-beams. The analysis was performed for a two-span continuous bridge. An analytical study was performed to quantify the stresses generated as a result of differential shrinkage, creep and temperature gradient at various sections in both directions. At the cross-sectional level, an elastic sectional analysis approach using the age-adjusted effective modulus method was used to perform the investigation. At the structure level, the effects of uniform temperature changes, thermal gradients and differential shrinkage and creep were investigated and quantified in terms of axial restraint forces and restraint moments. It is shown that, by paying attention to detailing and by selecting a mix design for the cast-in-place topping that has relatively low shrinkage and high creep, the potential for excessive cracking can be reduced.

The second investigation is of the stresses in the end zones of such a uniquely shaped precast element. The transfer of prestressing force creates vertical and horizontal tensile stresses in the end zones of the beam. A series of three-dimensional (3D) finite element analyses were performed to investigate the magnitude of these tensile stresses. Various methods of modeling the prestressing force, including the modeling of the transfer length, were examined and the effect of notches at the ends of the precast beams was explored. Existing design methods were evaluated; strut-and-tie models, calibrated to match the results of 3D finite element analyses, are proposed as alternatives to existing methods to aid designers in sizing reinforcing in the end zones.

The final section reports the results of live load testing performed on the first inverted T-beam bridge in Virginia on U.S. 360 over the Chickahominy River. A finite element model of Phase I of the U.S. 360 Bridge was created and the live load distribution factors were analytically determined. Live load tests using a stationary truck were performed on Phase I of the U.S. 360 Bridge with the purpose of quantifying live load distribution factors and validating the results from the finite element analyses. It is concluded that it is appropriate to estimate live load distribution factors using AASHTO provisions for cast-in-place slab span bridges.

17 Key Words: Inverted T-beam, time-dependent effects, end zone, stresses, live load test, distribution factors, finite element analyses	18. Distribution Statement: No restrictions. This document is available to the public through NTIS, Springfield, VA 22161.

19. Security Classif. (of this report): Unclassified	20. Security Classif. (of this page): Unclassified	21. No. of Pages: 76	22. Price:

Form DOT F 1700.7 (8-72) Reproduction of completed page authorized

FINAL REPORT

IMPLEMENTATION OF A PRECAST INVERTED T-BEAM SYSTEM IN VIRGINIA: PART II: ANALYTIC AND FIELD INVESTIGATIONS

Fatmir Menkulasi, Ph.D., P.E.
Assistant Professor
Department of Civil and Environmental Engineering
Wayne State University

Thomas Cousins, Ph.D., P.E.
Professor
Glenn Department of Civil Engineering
Clemson University

C.L. Roberts-Wollmann, Ph.D., P.E.
Professor
Via Department of Civil and Environmental Engineering
Virginia Polytechnic Institute and State University

VTRC Project Manager
Bernard L. Kassner, Ph.D., P.E., Virginia Transportation Research Council

In Cooperation with the U.S. Department of Transportation
Federal Highway Administration

Virginia Transportation Research Council
(A partnership of the Virginia Department of Transportation
and the University of Virginia since 1948)

Charlottesville, Virginia

August 2018
VTRC 19-R2

DISCLAIMER

The project that is the subject of this report was done under contract for the Virginia Department of Transportation, Virginia Transportation Research Council. The contents of this report reflect the views of the authors, who are responsible for the facts and the accuracy of the data presented herein. The contents do not necessarily reflect the official views or policies of the Virginia Department of Transportation, the Commonwealth Transportation Board, or the Federal Highway Administration. This report does not constitute a standard, specification, or regulation. Any inclusion of manufacturer names, trade names, or trademarks is for identification purposes only and is not to be considered an endorsement.

Each contract report is peer reviewed and accepted for publication by staff of the Virginia Transportation Research Council with expertise in related technical areas. Final editing and proofreading of the report are performed by the contractor.

ABSTRACT

The inverted T-beam superstructure is a bridge system that provides an accelerated construction alternative for short-to-medium-span bridges. The system consists of adjacent precast inverted T-beams with a cast-in-place concrete topping. This bridge system is expected to not experience the reflective cracking problems manifested in short-to-medium-span bridges constructed with traditional adjacent voided slab or adjacent box beams. This report presents the results of three phases of a comprehensive research project to develop and implement an inverted T-beam system for Virginia. The three phases are: investigation of time-dependent and temperature effects, investigation of end zone stresses, and live load testing.

The first investigation is of time-dependent effects in composite bridges with precast inverted T-beams. The analysis was performed for a two-span continuous bridge. An analytical study was performed to quantify the stresses generated as a result of differential shrinkage, creep and temperature gradient at various sections in both directions. At the cross-sectional level, an elastic sectional analysis approach using the age-adjusted effective modulus method was used to perform the investigation. At the structure level, the effects of uniform temperature changes, thermal gradients and differential shrinkage and creep were investigated and quantified in terms of axial restraint forces and restraint moments. It is shown that, by paying attention to detailing and by selecting a mix design for the cast-in-place topping that has relatively low shrinkage and high creep, the potential for excessive cracking can be reduced.

The second investigation is of the stresses in the end zones of such a uniquely shaped precast element. The transfer of prestressing force creates vertical and horizontal tensile stresses in the end zones of the beam. A series of three-dimensional (3D) finite element analyses were performed to investigate the magnitude of these tensile stresses. Various methods of modeling the prestressing force, including the modeling of the transfer length, were examined and the effect of notches at the ends of the precast beams was explored. Existing design methods were evaluated; strut-and-tie models, calibrated to match the results of 3D finite element analyses, are proposed as alternatives to existing methods to aid designers in sizing reinforcing in the end zones.

The final section reports the results of live load testing performed on the first inverted T-beam bridge in Virginia on U.S. 360 over the Chickahominy River. A finite element model of Phase I of the U.S. 360 Bridge was created and the live load distribution factors were analytically determined. Live load tests using a stationary truck were performed on Phase I of the U.S. 360 Bridge with the purpose of quantifying live load distribution factors and validating the results from the finite element analyses. It is concluded that it is appropriate to estimate live load distribution factors using AASHTO provisions for cast-in-place slab span bridges.

FINAL REPORT

IMPLEMENTATION OF A PRECAST INVERTED T-BEAM SYSTEM IN VIRGINIA: PART II: ANALYTIC AND FIELD INVESTIGATIONS

Fatmir Menkulasi, Ph.D., P.E.
Assistant Professor
Department of Civil and Environmental Engineering
Wayne State University

Thomas Cousins, Ph.D., P.E.
Professor
Glenn Department of Civil Engineering
Clemson University

C.L. Roberts-Wollmann, Ph.D., P.E.
Professor
Via Department of Civil and Environmental Engineering
Virginia Polytechnic Institute and State University

INTRODUCTION

Prefabricated Bridge Construction

Prefabricated bridge construction typically consists of individual elements that are fabricated off-site and delivered to the project site ready to be erected. This allows the concurrent production of the individual elements as opposed to cast-in-place concrete construction, in which the casting of a certain component can be done only if the supporting element is in place. The fabrication of elements off-site also eliminates the need to construct and remove formwork at the bridge site, work in close proximity to traffic, or operate in areas that are over water. The accelerated bridge construction offered by precast elements has been embraced by engineers and is being widely used in the United States.

Similar to structural steel building and bridge construction, the fabrication of a concrete bridge structure in individual pieces raises the question of how these components will be connected. In prefabricated bridge construction, these connections may deteriorate over time and create the need for bridge rehabilitation or replacement. It is in this area that cast-in-place concrete construction has an advantage over prefabricated construction because it reduces the number of joints, which are the problematic areas, and it offers a higher degree of redundancy, which in some cases is desirable. The challenge that engineers face today is how to design structures that consist of prefabricated elements but emulate the durability and redundancy of monolithic construction.

FHWA Scanning Tour

The Federal Highway Administration (FHWA) and the American Association of State Highway and Transportation Officials (AASHTO) initiated a scanning tour in April 2004 to explore state-of-the-art technologies for rapid construction already being implemented in other industrialized countries (Ralls et al., 2005). A team of eleven members (three representatives from FHWA, four representatives from state departments of transportation, one representative from county engineers, one university representative, and two representatives from industry) visited Japan, the Netherlands, Belgium, Germany, and France with the objective to identify international uses of prefabricated bridge elements and systems and to identify decision processes, design methodologies, construction techniques, costs, and maintenance and inspection issues associated with use of the technology. The team was interested in all aspects of design, construction, and maintenance of bridge systems composed of multiple elements that are fabricated and assembled off-site.

One of the systems identified in the scanning tour for implementation in the United States was the Poutre-Dalle system (Figure 1). This system was observed in France and "poutre-dalle" in French means beam-slab. The system consists of a series of adjacent precast inverted T-beams that serve as formwork for the cast-in-place topping. After the cast-in-place topping is placed, the system behaves as a composite slab. It eliminates the need for installing formwork on site and provides a connection between the precast and cast-in-place components through the transverse hooked bars protruding from the webs of the precast inverted T-beam. The Poutre-Dalle system is intended for short-to-medium-span bridges with spans ranging from 20 to 65 ft. The motivation for the adoption of such a system is related to reflective cracking problems associated with traditional systems used for short-to-medium-span bridges. These traditional systems typically feature composite bridges constructed with adjacent precast voided slabs and adjacent box beams (Figure 2).

Figure 1. Poutre-Dalle System (Ralls et al., 2005)

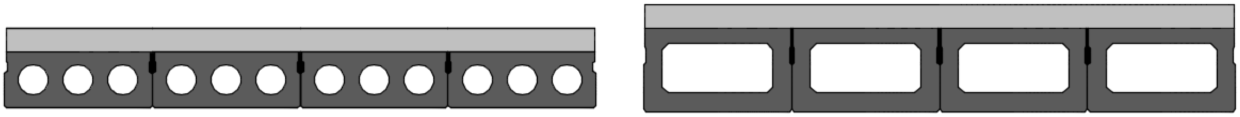

Figure 2. Voided Slab and Adjacent Box Beam Systems

One of the causes of reflective cracking is the transverse bending of the bridge when subject to concentrated loads such as vehicular loads (Figure 3). The only resisting mechanism against interface bond failure, if transverse post-tensioning is not applied in the adjacent box or voided slab system, is the tensile bond strength between the precast beams and the grout in the shear keys. The Poutre-Dalle system offers two improvements with respect to resistance against reflective cracking caused by transverse bending. First, it provides a thicker cast-in-place concrete topping over the longitudinal joints, and second, it offers a horizontal interface in addition to the vertical interface between the precast and cast-in-place components. The combination of these two interfaces emulates monolithic construction while preserving the benefits of prefabricated elements. In addition, the transverse hooked bars help arrest any potential cracks over the longitudinal joint or at the precast web cast-in-place topping interface.

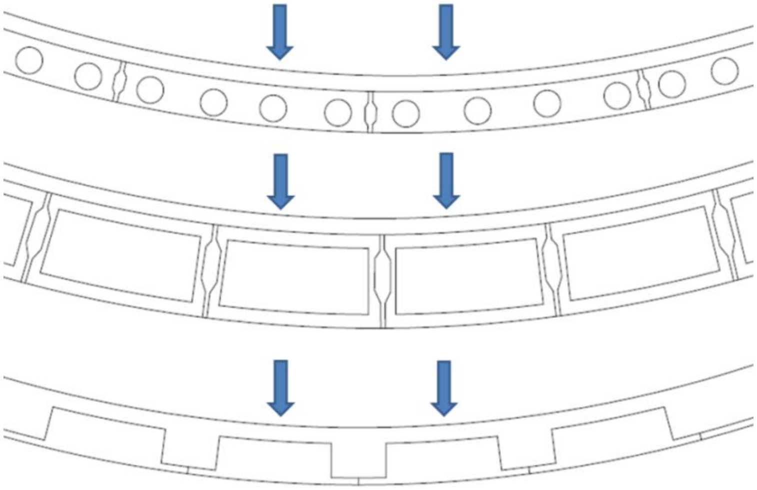

Figure 3. Deformed Shapes in Transverse Direction

Inspired by the Poutre-Dalle systems observed in France, engineers in Minnesota developed a similar system, which featured the same precast inverted T-beam shape and the extended transverse bars. The 180^o hook at the ends of the transverse bars was changed to a 90^o hook as shown in Figure 4(a). This was done to allow the placement of a “drop-in” reinforcing cage over the trough area to serve as additional reinforcing in the region above the longitudinal joint (Figure 4(b)). This system was targeted for implementation in the state of Minnesota for bridges with spans ranging from 20 ft to 65 ft. The first two bridges built with this system are located in Center City, Minnesota, and Waskish Township, Minnesota (Hagen et al., 2005) Over the course of seven years (2005 to 2012), researchers at the University of Minnesota investigated a variety of issues related to the design and construction of this new system. These issues included studies on reflective cracking, crack control reinforcing, composite action, transverse live load distribution, restraint moments, skew effects and stresses at the end zones. This research was presented in a series of technical reports (Hagen et al., 2005, Bell et al., 2006, Smith et al., 2007, Smith et al., 2008, Dimaculangan and Lesch, 2010, French et al., 2011).

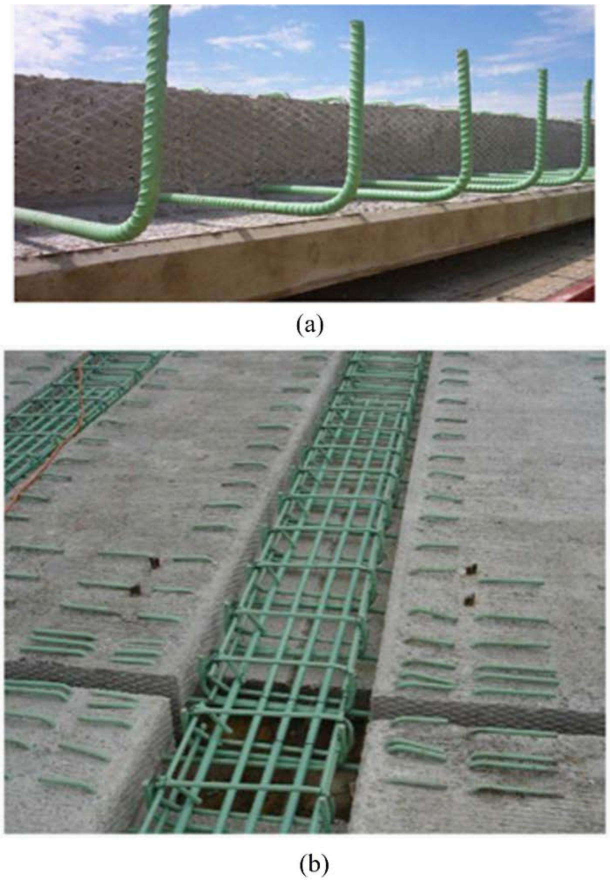

Figure 4. (a) Photograph of the Bars in the Precast Inverted T-Beam, (b) Photograph of the Reinforcement Cage Installed Above the Precast Longitudinal Joint (Hagen et al., 2005)

The inverted T-beam system developed in Minnesota was implemented on twelve bridges between 2005 and 2011 (Halverson et al., 2012). During this time, the original concept underwent a number of modifications to improve performance in different design generations. To determine the effects of these design modifications on performance, a series of field inspections was done for five existing inverted T-beam bridges (Halverson et al., 2012). Field inspections were conducted using two separate, but related, procedures: crack mapping and core examinations. Figure 5 shows a crack map and the locations where the cores were extracted for Bridge No. 33008 near Mora, Minnesota. Cores 1 and 2 revealed a full-depth reflective crack and a ½-in deep from surface shrinkage crack, respectively. Cores 3 and 4 revealed a 5¼-in deep reflective crack from the joint and a 3½-in deep shrinkage crack from surface. Figure 5 suggests that the extent of longitudinal and transverse surface cracking is extensive. Although the inverted T-beam system showed promise with respect to addressing reflective cracking concerns compared to the traditional voided slab system, the fabrication challenges presented by the extended transverse bars and the surface cracking observed in Minnesota's bridges prompted the need for additional research.

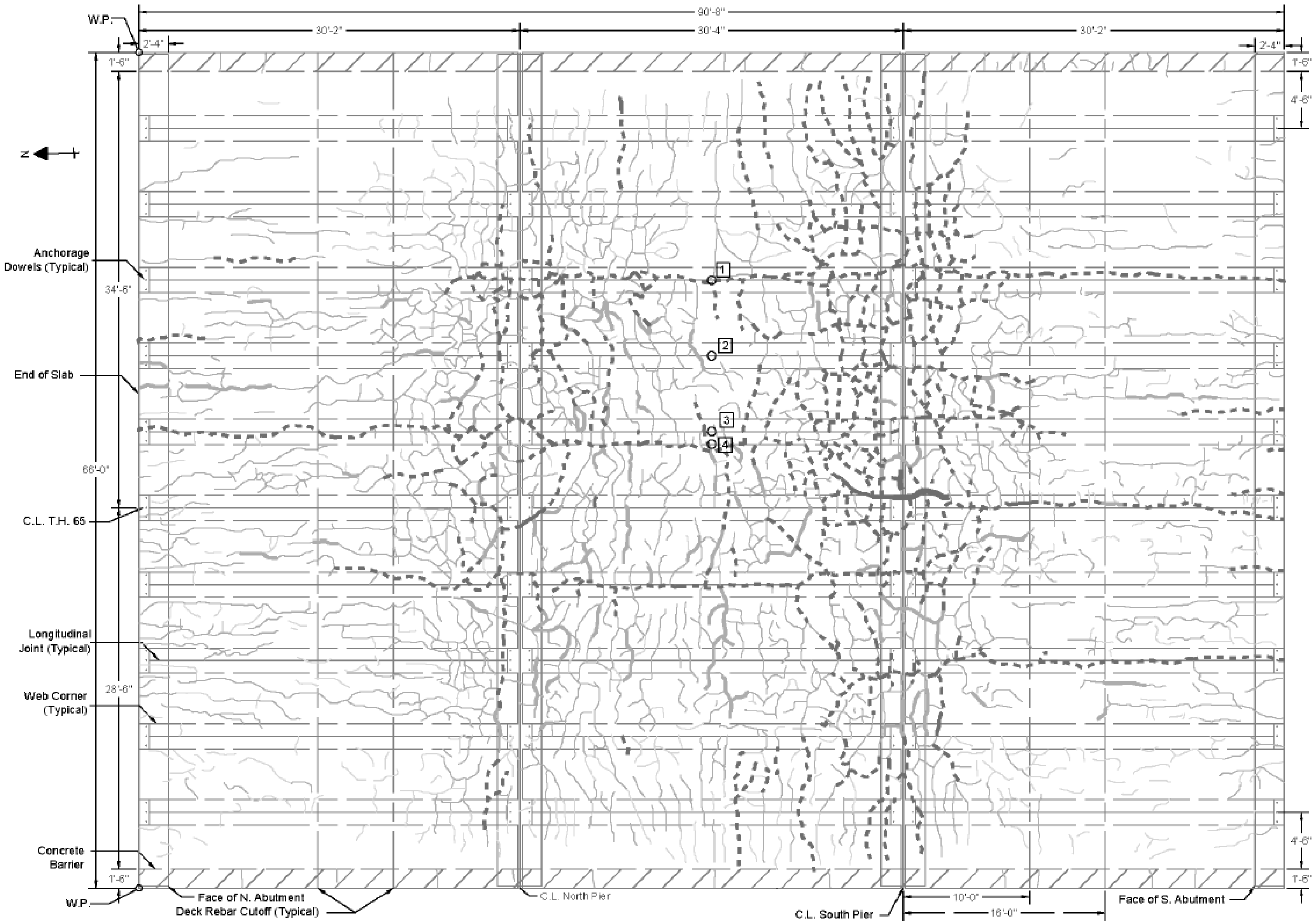

Figure 5. Crack Map for Bridge No. 33008, Inspection No. 3, June 16 and August 10, 2011, With Core Specimen Locations Indicated (Halverson et al., 2012)

PURPOSE AND SCOPE

Being aware of reflective cracking problems present in short-to-medium-span bridges built with adjacent voided slabs and adjacent box beam systems, the Virginia Department of Transportation expressed interest in implementing the precast inverted T-beam system for the first time in Virginia. The application was a bridge replacement project near Richmond, VA on U.S. 360 and featured four bridges (Figure 6). Three of these bridges were targeted to be replaced with the traditional adjacent voided slab system and one of them with the new inverted T-beam system. In addition, the bridge that was targeted for replacement using the inverted T-beam system (B607) was identical in terms of number of spans, span lengths, bridge width, traffic volume and environmental conditions with one of the neighboring bridges, which was scheduled to be replaced using the traditional adjacent voided slab system (B608). Both were two span continuous bridges with span lengths of approximately 43 ft (Figure 7). This provided an opportunity to observe the relative performances of these two bridges over time. There are multiple objectives of this project, and they are presented in the following sections. Other aspects of the investigation are presented in Part I of this report.

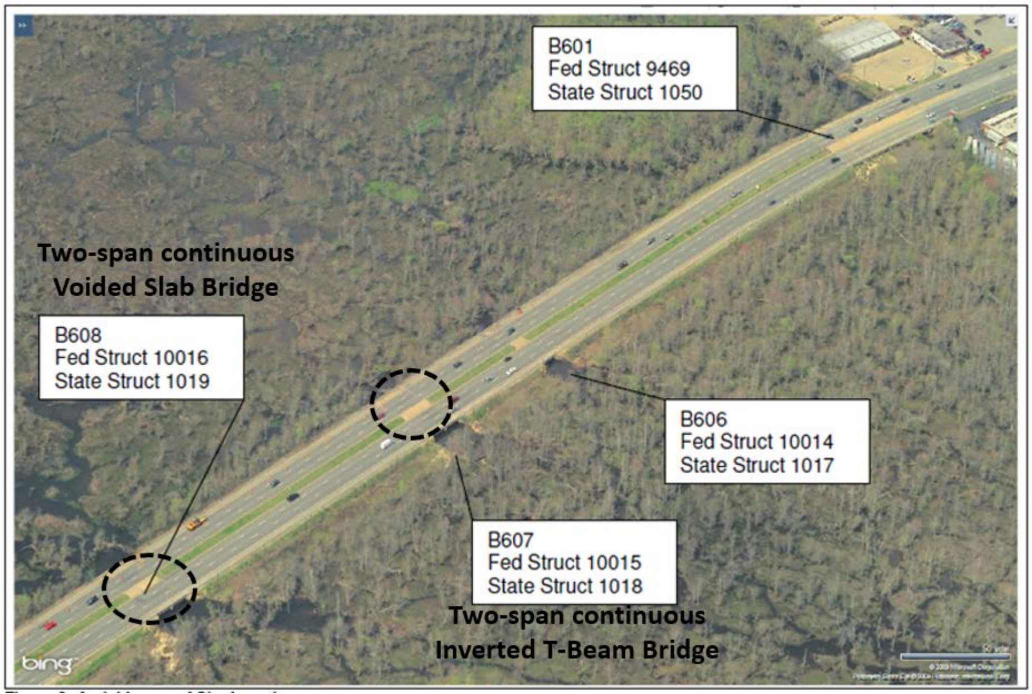

Figure 6. Aerial View of the Site Featuring Four Bridge Replacements (Hill and Lowe, 2010)

Investigation of Time-Dependent Behavior

Bridges constructed with prefabricated elements offer many advantages over conventional construction methods, but many existing bridges with precast components have durability issues, such as excessive cracking, which results in significant maintenance and replacement costs. This can eclipse the advantages that would otherwise be associated with these types of systems. Time-dependent effects, such as differential shrinkage between the cast-in-place and precast components, are a major reason for the development of this cracking.

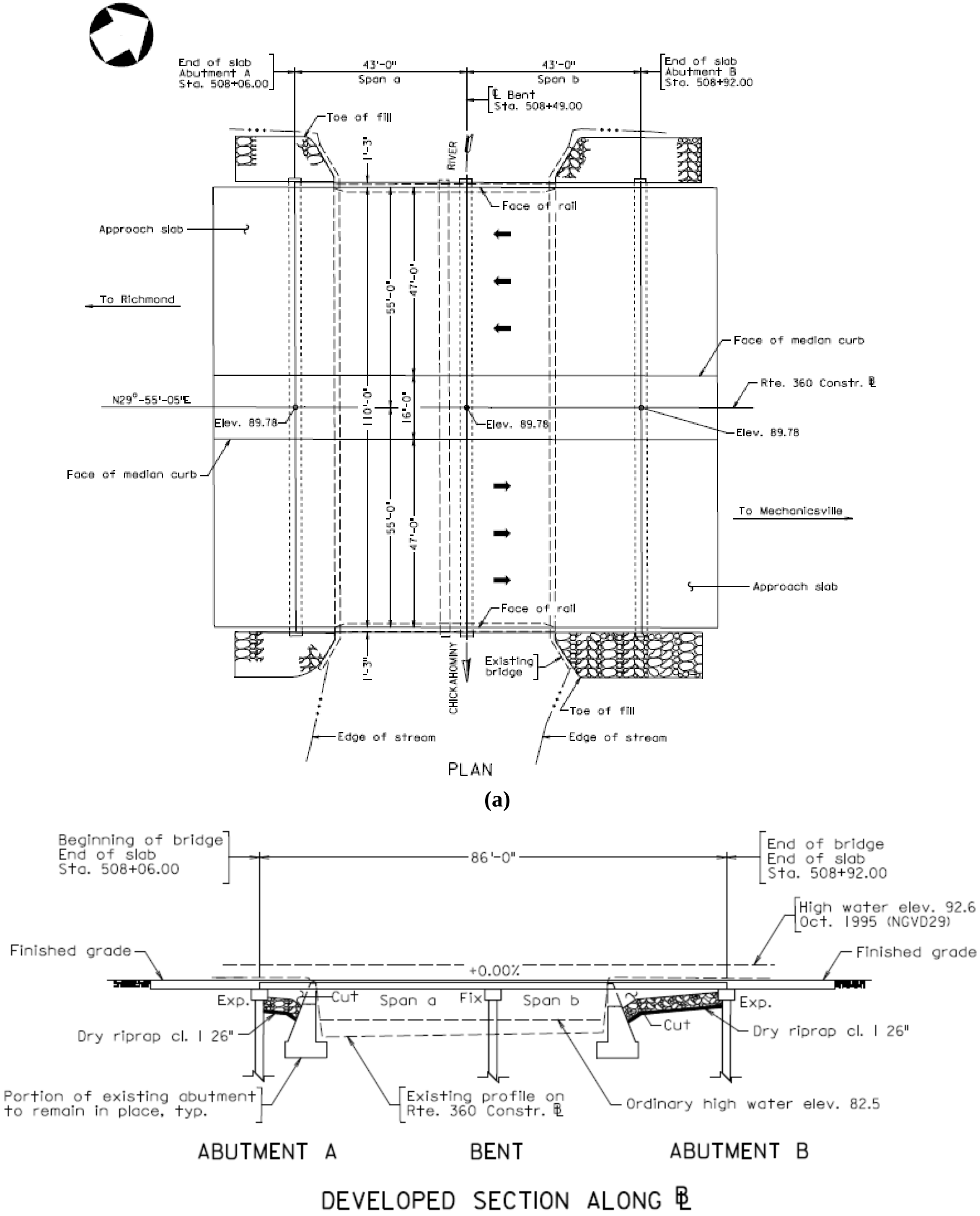

(a)

(b)

Figure 7. Preliminary (a) Plan and (b) Elevation of the U.S. 360 Bridge Over the Chickahominy River (Hill and Lowe, 2010)

In conventional cast-in-place, shored construction, the self-weight of concrete causes compressive stresses in the top surface of the deck in positive moment regions, and tensile stresses in negative moment regions. Additionally, tensile stresses created due to time-dependent effects are limited to differential shrinkage between cast-in-place concrete and reinforcing steel and those created due to temperature gradients. Consequently potential cracking is limited to negative moment regions because elsewhere compressive stresses due to the self-weight of concrete counterbalance any tensile stresses created due to time-dependent effects. The situation is different in systems that involve precast elements. Because the precast components provide support to the cast-in-place topping, the weight of the topping causes stress in the precast beams. As a result, the effects of differential shrinkage are more pronounced and can cause critical stress situations in the topping.

The first objective of the research presented in this report was to quantify the stresses developed as a result of differential shrinkage, shrinkage induced creep, negative and positive temperature gradients and a uniform decrease in temperature by performing a time-dependent analysis at the cross-sectional and structural level.

Investigation of Stresses in the End Zones

End regions of prestressed members are subject to high concentrated loads during the transfer of the prestressing force. Accordingly, the state of stress in these regions is complicated and cannot be predicted by the Euler-Bernoulli beam theory, in which plane sections are assumed to remain plane. According to Saint Venant's principle (Love, 1927), the disturbance caused by the concentrated forces at the ends of the member diminishes after a distance h from the end of the member, where h is the overall depth of the member. In pretensioned concrete members, the transfer of the prestressing force into the surrounding concrete creates tensile stresses in the end zones. These stresses are characterized as spalling, splitting and bursting stresses. Spalling stresses are vertical tensile stresses that occur near the end face at the centroid of the member. Splitting stresses are circumferential tensile stresses that occur around each individual prestressing strand along the transfer length and result from the radial compressive stresses caused by bond. Bursting stresses are vertical tensile stresses that occur along the line of the prestressing force, beginning a few inches into the member and extending through the transfer length. When these tensile stresses exceed the modulus of rupture of concrete, cracks form, which may compromise the shear and flexural strength of the member near that region as well as its durability. Because of the unique shape of the cross-section of the precast beam, the diffusion of the prestressing force will occur in both the vertical and horizontal planes.

The second objective of the research presented in this report was to quantify tensile stresses in the end zones in both planes and determine whether these stresses are high enough to cause cracking. A series of 3-D finite element analyses were performed to investigate the magnitude of these tensile stresses. Various methods of modeling the prestressing force including the modeling of the transfer length are examined and the effect of notches at the end of the precast beams is explored. Existing design methods are evaluated, and strut-and-tie models, calibrated to match the results of 3-D finite element analyses, are proposed as alternatives to existing methods to aid engineers in sizing reinforcing in the end zones.

Live Load Testing

The final objective of the research presented in this report was to determine the Live Load Distribution Factors (LLDFs) for composite bridges constructed with adjacent precast inverted T-beams with tapered webs. LLDFs for moment were determined by performing a live load test on Phase I of the U.S. 360 Bridge and measuring longitudinal strains at mid-span of the east span. The longitudinal strains at mid-width of each beam were divided by the sum of longitudinal strains to compute LLDF for moment in each girder. In addition, LLDFs for moment were computed using a finite element model of Phase I of the U.S. 360 Bridge using the same approach. After the results from the finite element model were validated based on field test results, the model was used to calculate LLDFs for shear. The measured and computed LLDFs were compared with each other and those calculated using the AASHTO's methods to determine which method is best suited to be used in the design of this new bridge system.

METHODS

This part of the final report presents two analytical studies and live load testing. The two analytical studies investigated time-dependent behavior of the inverted T-beam system and the behavior and design of the end region of the beams. The methods used in each study and the live load tests are presented in the following sections.

Investigation of Time-Dependent Behavior

To promote a comfortable ride and to reduce the likelihood of leakage to the substructure many engineers design precast beam bridges as continuous for live loads. Continuity is provided by placing a cast-in-place concrete topping over the precast elements, which creates a continuity diaphragm at the interior supports. Additionally, reinforcing steel is provided to connect the bottom of the precast beams over interior supports. The age of the precast beams when this continuity is established plays an important role in the development of time-dependent effects. The analysis performed assumed a precast girder age of 90 days or more, before continuity is established. At this age most of the shrinkage and creep in the precast girder has occurred.

The advantage of specifying a high age for continuity is the reduction of positive restraint moments at the intermediate supports. These positive restraint moments may develop due to creep of the precast beam, as well as due to positive thermal gradients. These positive restraint moments can be high enough to overcome the effects of negative live load moments (Halverson et al., 2012). In addition, these positive restraint moments can be high enough to result in the positive moment connection over the piers not providing 100% continuity.

One of the disadvantages of waiting for 90 days is that the differences in shrinkage and creep properties between the precast and cast-in-place components become more pronounced. Because the age of continuity for the bridge under consideration was assumed to be 90 days, the ultimate shrinkage strain and creep coefficient for the precast girder were neglected. The corresponding values for the cast-in-place topping were taken as follows:

$$\epsilon_{shdeck} = -466 \times 10^{-6}, \quad \phi_{deck} = 1.87 \qquad \text{Eq. 1}$$

These values were based on testing of seven different concrete mixes with a design compressive strength at 28 days of $f'_c = 4000$ psi. The goal was to identify a mix with low shrinkage and high creep. The results of this study are presented in Part I of this report, and the properties of the NWA-FA mix were used in the analysis.

Differential Shrinkage and Shrinkage-Induced Creep

Regardless of the boundary conditions, the inherent difference in shrinkage and creep properties between the cast-in-place topping and precast girders will cause self-equilibrating stresses at the cross-sectional level. Even if the composite beam is used in a single span simply supported bridge, these self-equilibrating stresses will form along the entire span of the bridge. The difference in shrinkage properties is exacerbated by the difference in age between the two components. As a result, when the topping is placed, it will tend to shrink while the majority of the shrinkage in the precast component has already taken place. The restraint provided by the precast component to the free shrinkage of the deck will create a tensile force in the deck while the free shrinkage of the deck will exert a compressive force on the precast beam.

In addition, because the centroids of the precast and cast-in-place components are at different locations, this differential shrinkage will cause a positive curvature. The curvature will result in a prestress gain in the bottom layer of prestressing in the precast beam, whereas the compression force from the shrinkage of the deck will cause a prestress loss. Another advantage of the precast inverted T-beam system is that the difference between the centroids of the cast-in-place and precast components is smaller compared to a similar voided slab or adjacent box girder system. Consequently the curvature induced due to differential shrinkage is smaller.

Mild steel in the deck will provide an additional level of restraint against the free shrinkage of the deck and will therefore increase the tensile stresses in the concrete topping. Figure 8 shows the idealized locations of mild steel and prestressing steel used in the time-dependent analysis. The amount of mild steel and prestressing steel was based on the design of the U.S. 360 Bridge per 2010 AASHTO LRFD Bridge Design Specifications (AASHTO, 2013).

The quantification of forces and stresses created due to differential shrinkage and shrinkage induced creep can be done using the principles of equilibrium, compatibility and material constitutive relationships. Menn (1990) provides detailed guidance on how this analysis can be performed. Some of the theoretical background provided in Menn is presented here for convenience. Figure 9 shows composite cross-section 2 and the change in strain and forces due to differential shrinkage and shrinkage induced creep. The internal forces created because of the shrinkage of the cast-in-place topping will cause the cast-in-place and precast components to creep over time. This shrinkage induced creep is captured by using the age-adjusted effective modulus method. The aging coefficient is assumed to be 0.7.

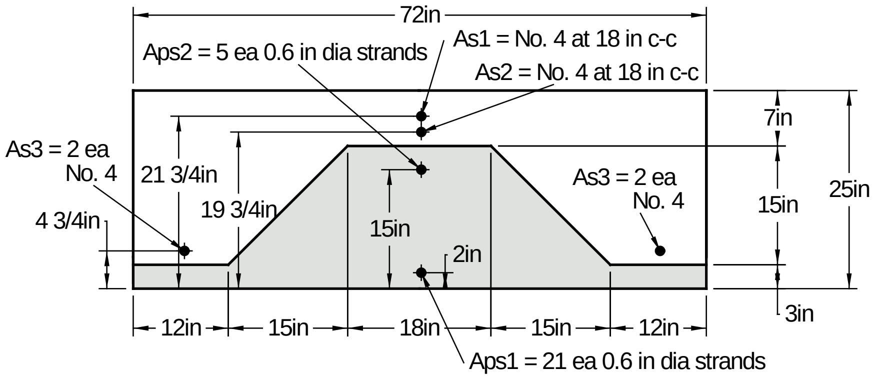

Section 1 - Transverse Section

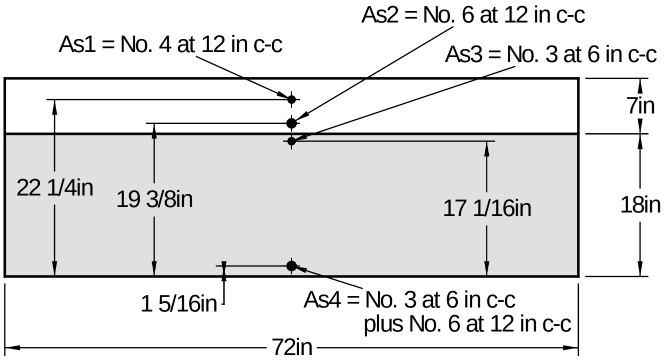

Section 2 - Longitudinal Section through Precast Web

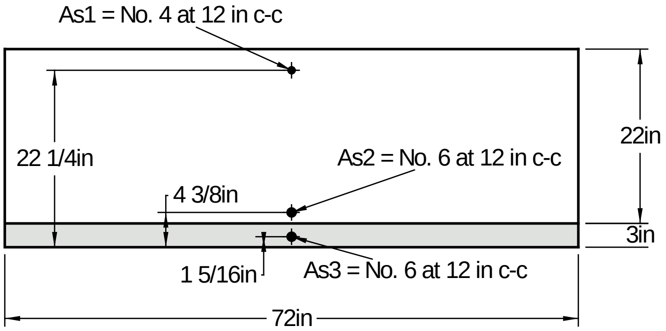

Section 3 - Longitudinal Section through Precast Flange

Figure 8. Idealized Locations of Mild Steel and Prestressing Steel Used in Time-dependent Analysis. Note: c-c = center-to-center; dia = diameter.

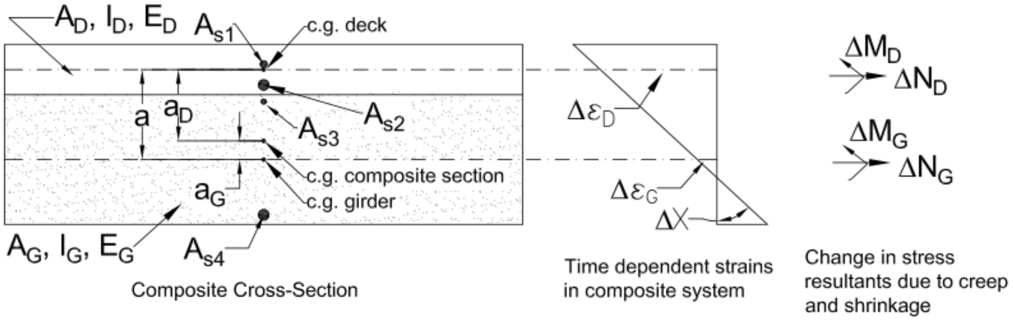

Figure 9. Forces in Composite Section 2 Due to Differential Shrinkage and Creep. Note: c.g. = center of gravity.

$$\Delta\varepsilon_D = \frac{\Delta N_D}{E_D\, A_D}\,(1+\mu\varphi_D) + \varepsilon_{SHD} \tag{Eq. 2}$$

$$\Delta X = \frac{\Delta M_D}{E_D\, I_D}\,(1+\mu\varphi_D) \tag{Eq. 3}$$

$$\Delta\varepsilon_s = \frac{\Delta N_s}{E_s\, A_s} \tag{Eq. 4}$$

$$\Delta\varepsilon_G = \frac{\Delta N_G}{E_G\, A_G}\,(1+\mu\varphi_G) + \varepsilon_{SHG} \tag{Eq. 5}$$

$$\Delta X = \frac{\Delta M_G}{E_G\, I_G}\,(1+\mu\varphi_G) \tag{Eq. 6}$$

$$\Delta N_D + \Delta N_G + \Delta N_{s1} + \Delta N_{s2} + \Delta N_{s3} + \Delta N_{s4} = 0 \tag{Eq. 7}$$

$$\Delta M_G + \Delta M_D - \Delta N_D a - \Delta N_{s1} a_{s1} - \Delta N_{s2} a_{s2} + \Delta N_{s3} a_{s3} + \Delta N_{s4} a_{s4} = 0 \tag{Eq. 8}$$

$$\Delta\varepsilon_D = \Delta\varepsilon_G - \Delta X\,(y_{Dbottom} - y_{Gbottom}) \tag{Eq. 9}$$

$$\Delta\sigma_D = \left(\frac{\Delta N_D}{A_D} + \frac{(\Delta M_D)}{I_D}\,y\right) \tag{Eq. 10}$$

$$\Delta\sigma_G = \left(\frac{\Delta N_G}{A_G} + \frac{(\Delta M_G)}{I_G}\,y\right) \tag{Eq. 11}$$

$$\Delta\sigma_S = \left(\frac{\Delta N_S}{A_S}\right) \tag{Eq. 12}$$

where

A_D = area of cast-in-place deck
A_G = area of precast girder
A_s = area of mild steel
a = distance between the centroid of cast-in-place deck and centroid of precast girder.
a_D = distance between the centroid of the cast-in-place deck and centroid of composite section
a_G = distance between the centroid of the girder and centroid of the composite section
E_D = modulus of elasticity of the cast-in-place deck
E_G = modulus of elasticity of the precast girder
E_s = modulus of elasticity of mild steel
I_D = moment of inertia of the cast-in-place deck
I_G = moment of inertia of the precast girder
y = distance from centroid
$\Delta\varepsilon_D$ = change in strain at the centroid of deck due to time-dependent effects
$\Delta\varepsilon_G$ = change in strain at the centroid of girder due to time-dependent effects
$\Delta\varepsilon_s$ = change in strain in mild steel due to time-dependent effects
ΔX = change in curvature due to time-dependent effects
ΔN_D = change in axial force in the deck due to time-dependent effects

ΔN_G = change in axial force in the girder due to time-dependent effects
ΔN_s = change in force in mild steel due to time-dependent effects
ΔM_D = change in moment in the deck due to time-dependent effects
ΔM_G = change in moment in the girder due to time-dependent effects
$\Delta \sigma_D$ = change in stress in deck due to time-dependent effects
$\Delta \sigma_G$ = change in stress in precast girder due to time-dependent effects
$\Delta \sigma_s$ = change in stress in mild steel due to time-dependent effects
ε_{SHD} = ultimate shrinkage strain of the deck
ε_{SHG} = ultimate shrinkage strain of the precast girder
φ_D= creep coefficient for the deck
φ_G= creep coefficient for the precast girder
μ = aging coefficient

For example, the change in strain at the centroid of deck and girder can be determined by computing elastic and creep strains due to the change in axial force plus the strain due to free shrinkage (Equations 2 and 5). Similarly, the change in curvature can be determined by calculating elastic and creep curvatures due to the change in moment (Equations 3 and 6). The change in strain in any given steel layer can simply be determined by computing the elastic strain due to the change in axial force in the corresponding layer (Equation 4). In addition, because there are no externally applied axial forces or moments the sum of the change in axial forces and moments needs to be equal to zero (Equations 7 and 8). Assuming that there is a perfect bond between the cast-in-place deck, precast inverted T and reinforcing steel, the axial strains at the centroid of each component can related by utilizing the curvature and the relative distances (principle of compatibility). Equation 9 provides one such example. By using Equations 2-9, a set of 15 equations and unknowns can be created and solved simultaneously. The unknowns include changes in strain and forces in each component and the change in curvature. After solving for the unknowns, the change in stress at any given location in the precast inverted T-beam, deck or at any layer of mild steel can be calculated using Equations 10-12. The assumptions made during this analysis were as follows:

- Plane sections remain plane.
- Sections are uncracked.
- Creep and shrinkage properties represent the average behavior of the entire cross-sections, or components thereof, in drying conditions.
- Tensile creep is the same as compressive creep.

Temperature Gradient

Temperature gradients create effects similar to the ones created by differential shrinkage. Because temperature can vary through the depth of the cross-section, some parts of the cross-section will tend to contract or expand more than the other parts. The temperature gradient used in this study was obtained from the AASHTO LRFD Bridge Design Specifications (AASHTO 2013) for the U.S. 360 Bridge near Richmond, Virginia. The positive and negative temperature gradients have a bi-linear shape and are shown in Figure 10. Assuming plane sections remain plane, this bi-linear variation in temperature will cause self-equilibrating stresses in the cross-section. These stresses can be calculated using the principles of equilibrium, compatibility and material constitutive relationships (Gilbert, 1988). A sensitivity analysis for the creep and aging coefficients was not done because it was assumed that the temperature gradient would develop over a period of 8 hours. As a result, the changes in creep and aging coefficients over such a short period of time would be negligible.

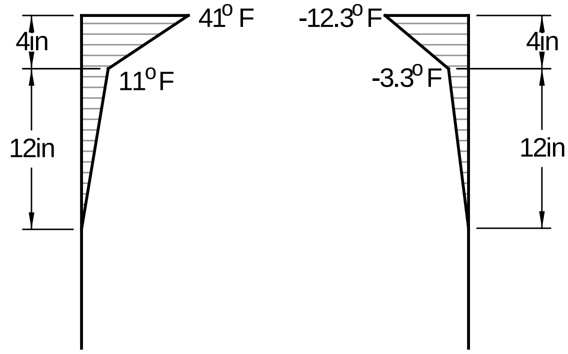

Positive Vertical Temperature Gradient

Negative Vertical Temperature Gradient

Figure 10. Positive and Negative Temperature Gradients for the U.S. 360 Bridge, Near Richmond, Virginia

Some of the theoretical background presented in Gilbert (1988) for the calculation of self-equilibrating stresses due to thermal gradients is presented here for convenience. Figure 11 illustrates this approach by taking Section 2 as an example and the negative temperature gradient shown in Figure 10. If all the fibers in the composite cross-section were free to contract independently to accommodate the imposed negative temperature gradient, then the result would be the free strain diagram shown in Figure 11. If the section were fully restrained from contracting, stresses would develop at each fiber equal to the restrained strain times the modulus of elasticity. The resultants of these restrained stresses (axial force and bending moment) can be calculated using Equations 13 and 14. In a simply supported beam, with no axial or moment restraint, the self-equilibrating stresses are the fully restrained stresses, minus the stresses calculated with the axial and moment restraints, because these restraints are released. These self-equilibrating stresses can be computed using Equations 15-17.

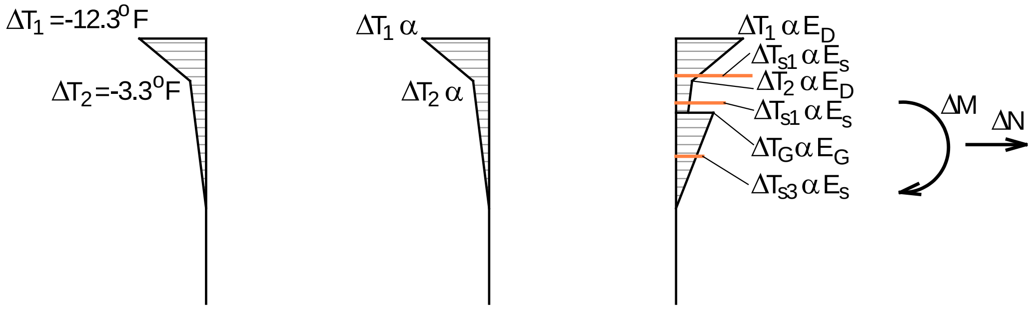

Negative Vertical Temperature Gradient

Free Strains (compressive)

Restraint Stresses (tensile)

Forces to Restrain Temperature Strains

Figure 11. Approach for Calculating Self-Equilibrating Stresses Due to Thermal Gradients (Section 2)

$$\Delta N = \int \alpha T(y) E b \, dy \qquad \text{Eq. 13}$$

$$\Delta M = \int \alpha T(y) E b y \, dy \qquad \text{Eq. 14}$$

$$\Delta \sigma_D = \Delta \mathrm{T(y)} \alpha E_D - \left(\frac{\Delta N}{A_{tr}} + \frac{\Delta M y}{I_{composite}} \right) n_D \qquad \text{Eq. 15}$$

$$\Delta \sigma_G = \Delta \mathrm{T(y)} \alpha E_G - \left(\frac{\Delta N}{A_{tr}} + \frac{\Delta M y}{I_{composite}} \right) \qquad \text{Eq. 16}$$

$$\Delta \sigma_s = \Delta T(y) \alpha E_s - \left(\frac{\Delta N}{A_{tr}} + \frac{\Delta M y}{I_{composite}} \right) n_s \qquad \text{Eq. 17}$$

where

A_{tr} = transformed area of the composite cross-section, in^2
b = width of cross-section at distance y from centroid of cross-section, in
E = modulus of elasticity
$I_{composite}$ = transformed moment of inertia of the composite cross-section, in^4
n_D = modular ratio of deck concrete relative to beam concrete
n_s = modular ratio of steel relative to beam concrete
$T(y)$ = temperature at distance y from centroid of cross-section
α = coefficient of thermal expansion
ε_1 = free strain at location 1 due to temperature gradient
ε_2 = free strain at location 2 due to temperature gradient
$\Delta\sigma_s$ = restrained stress in steel due to temperature gradient
$\Delta\sigma_D$= restrained stress in deck due to temperature gradient
$\Delta\sigma_G$= restrained stress in girder due to temperature gradient
ΔN = change in axial force due to restrained stress as a result of temperature gradient
ΔM = change in moment due to restrained stress as a result of temperature gradient

Time-Dependent and Temperature Analysis at the Structural Level

The indeterminacy of the superstructure plays an important role when it comes to evaluating the effects of differential shrinkage, creep and temperature at the structure level. For example axial contraction as a result of a uniform decrease in temperature in the longitudinal direction of the two-span continuous bridge can cause significant tensile stresses in the topping and in the precast beam if not accommodated. Temperature gradients and differential shrinkage can also cause tensile stresses if movements are restrained. The following discussion illustrates some of the effects that these phenomena can have if the bearing details at the abutments do not allow axial movements.

Another type of restraint at the structure level in multi-span bridges is the moment restraint at the intermediate supports. The restraint moments develop because the curvatures created by the differential shrinkage and temperature gradients are not allowed to freely take place due to the continuity of the bridge at the interior supports. The assumptions made at the structural level to perform a time-dependent analysis were as follows:

- The axial restraint provided by the abutments in the longitudinal direction was rigid.
- Plane sections remain plane.
- Sections are uncracked.
- Creep and shrinkage properties represent the average behavior of the entire cross-sections, or components thereof, in drying conditions.
- Tensile creep is the same as compressive creep.

Axial Restraint at the Abutments (Differential Shrinkage, Temperature Gradient, Uniform Temperature)

In a statically determinate structure the bridge superstructure will be free to contract and expand axially and therefore there will be only axial strains and no stresses. However, if this axial movement is restrained, the restraining axial force will create significant stresses in the superstructure. The calculation of these stresses can be performed by imposing the principle of compatibility that requires the total axial deformation to be zero at all bearings where this deformation is restrained. The restraining force can be calculated using the force method of structural analysis in which the axial deformation due to differential shrinkage, temperature gradient and uniform temperature changes must be equal to the axial deformation caused by the restraining force. The uniform temperature change used in this investigation was based the AASHTO LRFD Bridge Design Specifications (2013) and was calculated to be 70^{o}F.

Moment Restraint at the Intermediate Support

Restraint moments at the intermediate supports are another source for developing tensile stresses in the deck that can lead to excessive transverse cracking. These moments are developed as a result of the restraint to the curvatures induced by creep of concrete under sustained loads and prestressing, differential shrinkage and temperature gradients. The calculation of restraint moment (M_r) due to prestressing, sustained loads and differential shrinkage is based on Equation 18 (Peterman and Ramirez, 1998):

$$M_r = \underbrace{\left(\frac{3}{2}\,\alpha M_p - \alpha M_{dprecast}\right)\left[\Delta\left(1 - e^{-\varphi_1}\right)\right]}_{Term\ 1} \underbrace{- \alpha M_{dCIP}\left(1 - e^{-\varphi_2}\right)}_{Term\ 2} \underbrace{- \frac{3}{2}\,\alpha M_s\left(\frac{1-e^{-\varphi_2}}{\varphi_2}\right)}_{Term\ 3} \qquad \text{Eq. 18}$$

where

M_p = moment caused by prestressing force about centroid of composite member

M_S = differential shrinkage moment

$M_{dprecast}$ = mid-span moment due to dead load of precast members

M_{dCIP} = mid-span moment due to dead load of the cast-in-place topping

ϕ_1 = creep coefficient for creep effects initiating when prestress force is transferred to the precast panels

ϕ_2 = creep coefficient for creep effects initiating when the cast-in-place topping is cast

α = factor that accounts for the relative flexural stiffnesses of the spans and diaphragm
Δ $(1-e^{-\phi_1})$ = change in expression $(1-e^{-\phi_1})$ occurring from time the cast-in-place topping is cast to time corresponding to restraint moment calculation

The first term represents the restraint moment due to creep of the precast member due to prestressing force and the weight of the precast member. The second term represents the restraint moment due to creep of the precast member due to the cast-in-place topping weight. The third term represents the restraint moment due to differential shrinkage. Peterman and Ramirez (1998) provide additional information for the calculation of some of the terms defined including an equation for the calculation of differential shrinkage moment. However, this equation does not account for the restraint provided by steel in the precast member, so the calculation of differential shrinkage moment was based on Menn's method (Menn, 1990), which considers all the aforementioned effects.

Investigation of Stresses in the End Zone

Background

AASHTO LRFD Specifications (2013) require that reinforcing be provided in pre-tensioned anchorage zones to resist 4% of the total prestressing force. The Specifications also require that this reinforcing be placed within a distance that is equal to *h/4* from the end of the beam, where *h* is the overall dimension of the precast member in the direction in which splitting resistance is evaluated. These provisions, labeled as splitting provisions, are intended to resist spalling forces. For the remainder of this section, the tensile stresses on the loaded face of the beam are referred to as spalling stresses. The value of *h* and the direction in which the reinforcing required to resist the spalling forces is oriented, depends on the shape of the member. For example, for pretensioned I-girders or bulb tees, *h* represents the overall depth of the member and the end zone reinforcing is placed vertically within a distance equal to *h/4* from the end of the member. For pretensioned solid or voided slabs, *h* represents the overall width of the section and the end zone reinforcing is placed horizontally within *h/4*. For pretensioned box or tub beams with prestressing strands located in both the bottom flange and the webs, end zone reinforcing is placed both horizontally and vertically within h/4, where "h" is the lesser of the overall width or height of the member. Although not specifically addressed in AASHTO, the confinement required by AASHTO 5.10.10.2 should help control the bursting and splitting stresses that develop in the transfer length region (French et al., 2011). It should be noted that the Specifications require that end zone reinforcing be provided in the vertical plane, horizontal plane or both planes depending on the geometry of the pre-tensioned member, the strand pattern or the eccentricity in the plane under consideration.

Because the inverted T-beam system featuring adjacent precast inverted T-beams with tapered webs and cast-in-place topping is a new bridge system, there is a need to evaluate the applicability of the current Specification provisions for pretensioned anchorage zones. The U.S. 360 Bridge is a two-span continuous bridge. The design span for the precast inverted T-beams is 41.5 ft. The design concrete compressive strength at transfer is $f'_{ci} = 5$ ksi. Figure 12(a) shows an isometric view of the end of the precast beam featuring recessed precast flanges at bearing locations to avoid high flexural stresses at the precast web-flange intersection. The recession of the precast flanges allows the precast web to resist the reaction at the support and prevents the transverse bending of the 4 in flanges, which would take place if the flanges are not recessed. Also, as a practical measure, recessing the corners reduces the possibility of cracking and spalling the corners during handling. The length of precast flange recession is 12 in. Three 6 in by 9 in by ½ in elastomeric bearing pads (70 durometer hardness) were provided at the ends of each precast inverted T-beam and were located within the width of the precast web. The rest of the bearing area was covered with ½ in preformed asphalt joint filler.

Figure 12(b) and (c) show the end zone reinforcing at Sections 1 and 2, respectively. End zone mild steel reinforcing consists of AASHTO required confinement steel, and features No.4 stirrups. The first four rows of confinement steel are placed at 3 in on center with the first row at 2 in from the end face. The rest of the confinement steel is placed at 6 in on center. In addition, four legs of No.4 extended stirrups are provided at the same spacing as the confinement steel. Beyond a distance equal to 1.5*d*, where *d* is the effective depth of the member, the spacing of closed and extended stirrups is 12 in. Past the flange cuts, horizontal transverse steel consisting of No.4 at 8 in on center is provided to resist the wet weight of cast-in-place concrete topping

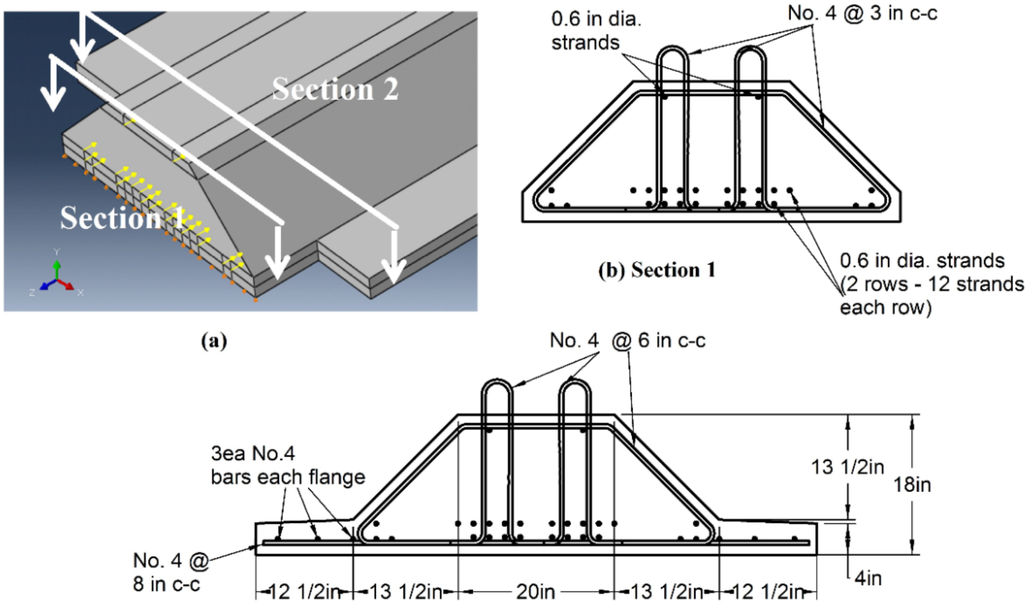

(a)

(b) Section 1

(c) Section 2

Figure 12. (a) Isometric View of Precast Section, (b) Section 1, (c) Section 2. Note: dia. = diameter, c-c = center-to-center, and each = each.

and transverse bending moments due to live loads. All prestressing steel is concentrated within the footprint of the precast web. The bottom two layers of prestressing consist of 24 0.6-in diameter strands (twelve strands in each layer). The top layer consists of two 0.6 in diameter strands. The jacking force for each Grade 270 strand was 44 kips. The eccentricity of the strand group is 2.99 in. In addition to the 26 fully stressed strands described, four additional strands stressed only to 1 kip were provided to facilitate the placement of extended stirrups. Longitudinal normal stresses during transfer were kept below AASHTO allowable stresses without the need to resort to strand debonding.

Gergely et al. (1963) state that the horizontal cracks that frequently form in the end region of prestressed concrete members when the prestressing strand is released and the prestressing force is transferred to the concrete section are defined as spalling cracks. If unrestrained, these cracks can extend into the precast member and negatively affect the flexural and shear strength and durability of the member. Studies performed by Fountain (1963) suggest that these cracks cannot be eliminated, however vertically oriented reinforcing steel can limit crack width and propagation.

Gergely et al. (1963) showed that the distribution of the tensile stresses in the end region depends on the eccentricity of the prestressing force in the member. For example, in a concentrically loaded member, forces distribute symmetrically through the vertical member height until a uniform stress distribution is established at a distance *h* from the end of the member (Saint Venant's principle (Love, 1927)). In such a member, the spalling forces developed at the end face are smaller than the bursting forces that develop at a distance *h/2* from the end of the member (Figure 13(a)). Conversely, in an eccentrically loaded member the spalling forces developed near the end face are higher than the bursting forces developed a certain distance away from the end of the member (Figure 13(b)).

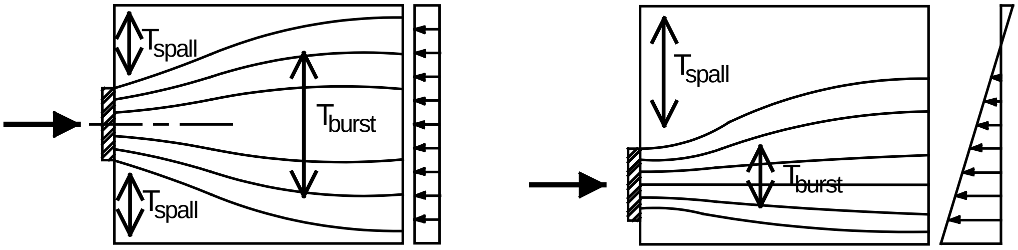

(a) Concentrically prestressed member (b) Eccentrically prestressed member

Figure 13. Flow of Stresses in the End Zone

French et al. (2011) performed an evaluation of the stresses in the end zones of precast inverted T-beams with straight webs to determine the applicability of the AASHTO provisions on pretensioned anchorage zones. Because the overall depth of precast inverted T-beams is relatively shallow compared to I-girders, the requirement to place the vertical steel in the end zone within a distance equal to *h/4* from the end of the member results in congestion problems. However, as stated earlier, the placement of vertical steel in the end zones of wide and shallow members (solid or voided slabs) is relaxed by allowing the designer to spread this steel within a distance *h/4* where *h* is the width of the member rather than its depth. According to French et al., such a relaxation may not be appropriate when trying to control spalling stresses, because in eccentrically loaded members, the magnitude of spalling stresses diminishes quickly away from the end of the member.

The evaluation that French et al. (2011) performed included experimental and numerical studies. The experimental study was performed on laboratory bridge specimens, constructed with precast inverted T-beams, which featured various configurations of end zone reinforcing. The experimental results revealed that the 12 in deep precast sections had sufficient strength to resist the tensile stresses created in the end zone even in cases where no vertical steel was present. These findings were corroborated with the results of numerical studies that showed certain inverted-T members did not require spalling reinforcement, specifically those members with depths less than 22 in for which the expected concrete strength was higher than the expected tensile stresses due to the development of prestress.

In contrast, for deep inverted T-beams, it was numerically determined that larger amounts of spalling reinforcement than specified by AASHTO's provisions for splitting resistance are required. It was also concluded that the reinforcement should be placed as close to the end of the beam as possible (i.e., within *h/4* of the end of the member, where *h* represents the depth of the member). For the numerical study, finite element modeling was used to determine the magnitude and location of spalling and bursting stresses by employing several simplifications to reduce the complexity and computational requirements of the model. The flanges were neglected to allow the system to be modeled as a two-dimensional rectangular slab. As a result, spalling and bursting stresses were only investigated in the vertical plane.

Some of the suggested modifications to AASHTO (2013) Article 5.10.10.1 that resulted from this study are presented here:

- For all sections other than rectangular slabs and shallow inverted-T sections with heights less than 22 in, the spalling resistance of pretensioned anchorage zones provided by reinforcement in the ends of pretensioned beams shall be taken as:

$$P_r = f_s A_s \qquad \text{Eq. 19}$$

where

f_s = stress in steel not to exceed 20 ksi

A_s = total area of reinforcement located within the distance h/4 from the end of the beam, in^2

h = overall dimension of precast member in the direction in which spalling resistance is being evaluated, in.

The resistance shall not be less than 4% percent of the total prestressing force at transfer.

- In pretensioned anchorage zones of rectangular slabs and shallow inverted-T sections with heights less than 22 in, vertical reinforcement in the end zones is not required if:

$$\sigma_s < f_r \qquad \text{Eq. 20}$$

where

$$\sigma_s = \frac{P}{A}\left(0.1206\frac{e^2}{h\,d_b} - 0.0256\right) \geq 0 \qquad \text{Eq. 21}$$

$$f_r = 0.23\sqrt{f'_{ci}} \qquad \text{Eq. 22}$$

where

σ_s = maximum spalling stress on the end face, ksi
f_r = direct tensile strength as defined by Article C5.4.2.7, ksi
P = prestressing force at transfer, kips
A = gross cross-sectional area of concrete, in^2
e = strand eccentricity, in
h = overall depth of precast member, in
d_b= prestressing strand diameter, in
f'_{ci} = concrete compressive strength at transfer, ksi

Where end zone vertical reinforcement is required, it shall be located within the horizontal distance *h/4* from the end of the beam and shall be determined as:

$$A_s = \frac{P\,(0.02\frac{e^2}{h\,d_b} - 0.01)}{f_s} \qquad \text{Eq. 23}$$

The resistance shall not be less than 4%of the total prestressing force at transfer. In all cases, the reinforcement shall be as close to the end of the beam as practicable. Reinforcement used to satisfy this requirement can also be used to satisfy other design requirements.

In the suggested modifications presented, the modulus of rupture is taken equal to $0.23\sqrt{f'_{ci}}$. The commentary of Article C5.4.2.6 in AASHTO states that: “Most modulus of rupture test data on normal weight concrete is between $0.24\sqrt{f'_c}$ and $0.37\sqrt{f'_c}$ . ..The given values may be unconservative for tensile cracking caused by restrained shrinkage, anchor zone splitting, and other tensile forces caused by effects other than flexure. The direct tensile strength should be used for these cases.” In addition, the commentary of Article C5.4.2.7 in AASHTO states: “For normal weight concrete with specified compressive strengths up to 10 ksi, the direct tensile strength may be estimated as f’$_r$ = $0.23\sqrt{f'_c}$”. Accordingly, the estimation of the tensile strength based on $0.23\sqrt{f'_{ci}}$ to determine the likelihood of cracking at the end zones because of the diffusion of the prestressing force is consistent with AASHTO’s commentary.

As stated earlier, because the precast inverted T-beam with tapered webs features a unique shape, there was a need to evaluate the applicability of the current provisions given in the

AASHTO LRFD Specifications, as well as the recommendations made by French et al. (2011) for the vertical plane.

The numerical study performed by French et al. (2011) was based on 2D finite element models using shell elements and by modeling only the precast web. The presence of precast flanges was ignored to make possible such an idealization in 2D. In this study, the precast beams are modeled as 3D components using 3D continuum elements for concrete and 3D embedded truss elements for prestressing strands. As a result, tensile stresses in the end zones are investigated in the vertical plane as well as in the horizontal plane. Such 3D modeling was essential for the precast inverted T-beams with the tapered webs, because, in this case a 2D idealization would not be justified.

Investigation Using Finite Element Analysis

The precast inverted T-beam section used in the construction of the U.S. 360 Bridge was modeled using 3D continuum elements using the commercially available finite element software ABAQUS (2012). Initially, stresses and deflections due to the self-weight of the member were computed using a 2 in mesh with the purpose of comparing them with those calculated using the Euler-Bernoulli beam theory. Table 1 shows a comparison between stresses and deflections computed using finite element analysis and those based on "hand calculations" using the Euler-Bernoulli beam theory. This comparison was carried out for the top and bottom fibers at mid-span of the beam. The difference in the results is very small, which demonstrates that a 2 in mesh can properly capture the effects of the self- weight of the member. Mid-span deflections were identical whereas the small differences in top and bottom stresses can be attributed to the 3D state of stress in the finite element model compared to the 1D stress state employed in the beam line theory used in hand calculations.

Table 1. Comparison of Stress and Deflections Due to Self-Weight

Measurement	Location	FEA*	Euler-Bernoulli	% Difference
Max. longitudinal stress, ksi	Mid-span - Top	1.16	1.17	0.9
Max. longitudinal stress, ksi	Mid-span - Bottom	0.72	0.74	3.0
Deflection, in	Mid-span	0.64	0.64	0.0

*FEA = Finite Element Analysis.

U.S. 360 Bridge Girder (41.5-ft Span)

The implementation of the inverted T-beam system in the U.S. 360 Bridge provided a good opportunity to observe the performance of a unique precast shape immediately after prestress transfer. The modulus of elasticity for the precast beam at transfer was calculated based on the formula provided in Article 5.4.2.4 of AASHTO LRFD Specifications (2013) as a function of the design compressive strength at transfer and was 4287 ksi. Poisson's ratio was used as 0.2 (based on Article 5.4.2.5 of AASHTO LRFD Specifications). Linear elastic finite element analyses, which are appropriate up to the initiation of cracking, were performed to investigate stresses in the end zones in the vertical and horizontal planes. Various methods of modeling the prestressing force were considered with the purpose of identifying the most accurate modeling technique. In all the modeling techniques presented in the following sections, only the effect of the fully stressed 26 strands was considered. The effect of the four additional top strands used for constructability and stressed only to 1 kip was considered negligible.

Vertical Plane - Case 1

The prestressing force in Case 1 was modeled as a series of concentrated loads at the ends of the precast beam simulating a condition similar to a post-tensioned beam (Figure 14). As stated earlier, concrete in the precast beam was modeled using 3D continuum elements. The advantage of this modeling technique is simplicity. The strands are not modeled and the entire prestressing force is assumed to be applied at the ends of the precast beam. This modeling technique does not take into consideration the transfer length for the prestressing force. The magnitude of the prestressing force in each strand was taken as the jacking force. The magnitude of normal longitudinal stresses away from the end zones was similar to that calculated using hand calculations based on the principles of linear elastic mechanics of materials. However, in the end zones high spalling stresses are created because the application of the prestressing force was unrealistically high. This was because the concentrated loads representing the force in the strands were applied entirely at the nodes of the elements at the end faces of the precast beam. These concentrated forces created high stress concentrations in the vicinity where they were applied as well as along the depth the precast beam at the ends.

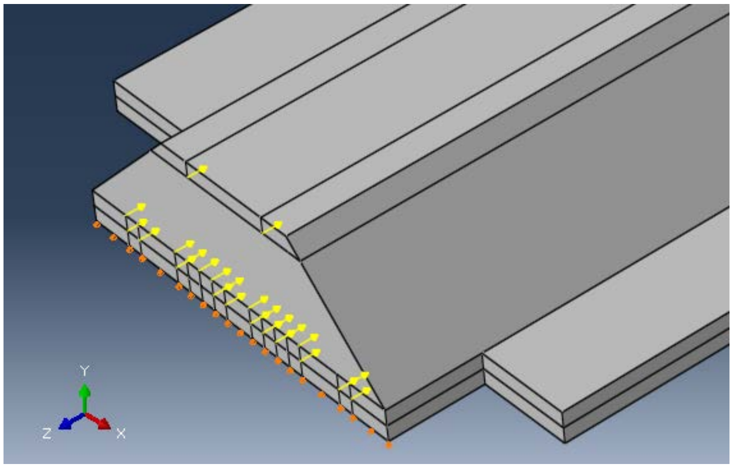

Figure 14. Prestressing Applied as Point Loads at the Ends

Vertical Plane - Case 2

In this case, the prestressing strands were modeled as embedded truss elements in perfect bond with 3D continuum elements used for concrete. The prestressing force in the strands was modeled as an initial condition, which simulates the tensile stress in the pretensioned strands. This modeling capability is available in ABAQUS. A uniform tensile stress was applied along the length of the strands and the cross-sectional area of the strands was kept constant along the span of the precast beam. This modeling technique while more realistic than the previous one, still does not take into consideration the transfer length because it assumes that the prestressing force is constant along the length of the precast beam starting at the face of the beam.

Vertical Plane - Case 3

The modeling technique utilized in this case is similar to that used in Case 2 with the exception that the transfer length was modeled by incrementally varying the cross-sectional area of the prestressing strands along the transfer length. The transfer length was taken equal to 60 strand diameters as given in Article 5.11.4.1 of AASHTO LRFD Specifications (2103). By keeping the magnitude of the prestress constant and by incrementally varying the cross-sectional area of the strands within the transfer length the amount of prestressing force transferred to the surrounding concrete varies linearly within the transfer length.

Vertical Plane - Case 4

The flanges of the precast beam were cut by approximately 1 ft at the ends to avoid high flexural stresses at the intersection of the precast flange and web at the bearing points. A finite element model without this cut was created to determine whether the presence of the cut has an adverse effect on the stresses at the end zones.

Horizontal Plane

The diffusion of the prestressing force was also investigated in the horizontal plane. Because the prestressing force introduced at the top layer consisted of only two 0.6 in diameter strands and because these strands were located near the top corners of the precast web, there was limited space for the prestressing force to diffuse. Accordingly, normal tensile stresses in the horizontal plane at the top portion of the beam were negligible. However, the distribution of the prestressing force introduced at the bottom two layers (24 0.6 in diameter strands) caused normal tensile stresses in the horizontal plane that were higher in magnitude. This is because the strands at these two layers were located within the footprint of the precast web and the prestressing force at this location could diffuse horizontally outwards toward the precast flanges. In addition, the magnitude of the prestressing force at the bottom two layers was the majority of the prestressing force introduced in the entire section.

Other Cases Investigated

Because the precast inverted T-beam bridge system can be used for short-to-medium-span bridges with spans ranging from 20 ft to approximately 60 ft, two additional cases that represent the extreme spans in this range were investigated.

20-ft Span

A composite bridge featuring 20 ft long spans was designed based on AASHTO LRFD Specifications (2013) with the purpose of determining the number of prestressing strands required to resists the effects of the design loads. The cross-sectional dimensions for the precast and cast-in-place components, as well as the number and position of prestressing strands are shown in Figure 15. Material properties for the precast beam, cast-in-place concrete and prestressing strands were the same ones used for the U.S. 360 Bridge. The prestressing force

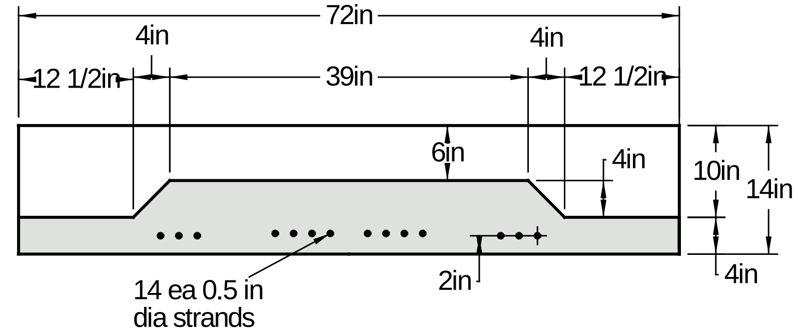

Figure 15. Typical Composite Bridge Cross-Section for a 20-ft Long Span (Mild Reinforcing Not Shown). Note: each = each, dia = diameter.

was modeled as described in Case 3 for the 41.5 ft span because that was determined to be the most accurate modeling technique. The eccentricity of the prestressing force is 1.47 in.

60-ft Span

A composite bridge featuring a 60-ft long span was designed based on AASHTO LRFD Specifications to represent a long span for the inverted T-beam system. The cross-sectional dimensions for the precast beam and the cast-in-place topping are shown in Figure 16. The eccentricity of the prestressing force is 3.94 in. The material properties for the precast beam, cast-in-place topping and prestressing strands were identical to the ones used for the U.S. 360 Bridge.

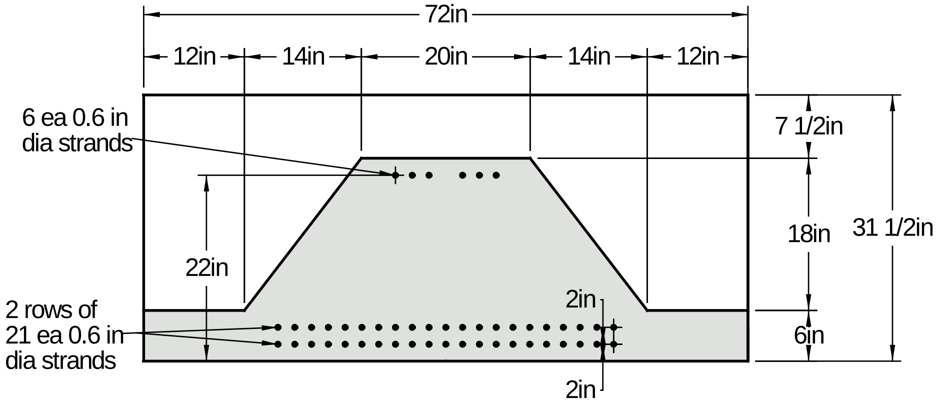

Figure 16. Typical Composite Bridge Cross-Section for a 60-Ft Long Span (Mild Reinforcing Not Shown for Clarity). Note: dia = diameter, ea = each.

Live Load Testing

This section describes the live load testing of the U.S. 360 Bridge. As mentioned previously, the U.S. 360 Bridge is a two-span continuous bridge. Each span length, measured as the distance from the center of the intermediate support to the edge of the superstructure at the abutments is 43 ft. The west span is called *span a* and the east span is called *span b* (Figure 7). Figure 17 shows the construction phases of the U.S. 360 Bridge. As can be seen from Figure 17, the adjacent precast inverted T-beam system is used to replace an existing bridge constructed

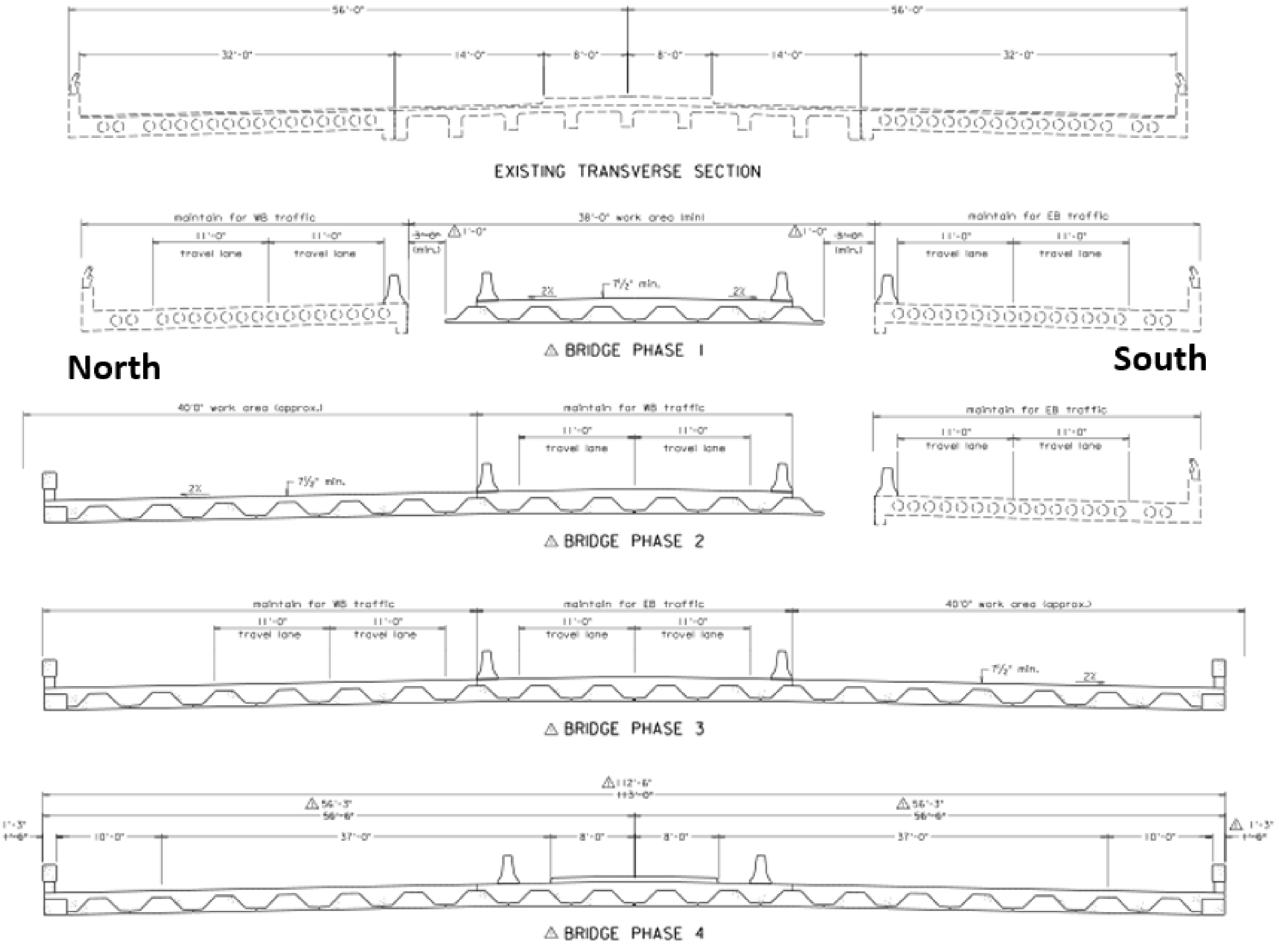

Figure 17. Construction Phasing of U.S. 360 Bridge

with a combination of voided slab and T-beam structures. The width of the new completed bridge from outside edge of barrier to outside edge of barrier is 112 ft – 6 in. The width of bridge during Phase I is 36 ft. The live load test described in this section was conducted during the construction of Phase I of the bridge. When the live load test was conducted, only the east barrier was installed on the bridge. The barrier consisted of seven precast units, each 12 ft long. The connection between the precast barrier units consisted of an unbonded dowel type connection, which was intended to provide a loose mechanical connection between the precast units in case of a lateral impact. This connection did not provide any continuity for moment or any shear transfer between the precast units. The connection between the barrier and the cast-in-place topping featured post-installed anchors only on the traffic side.

Figure 18 shows the cross-sectional dimensions and reinforcing details for a typical composite transverse cross-section. The depth of the precast inverted T-beams is 18 in and the depth of the cast-in-place concrete topping is 7.5 in. The transverse connection between the adjacent precast inverted T-beams features discrete embedded steel plates and welded bars (Figure 19). The embedded steel plates are located at the precast flanges and are spaced at 2 ft on center in the longitudinal direction. Each embedded steel plate is inclined to receive a field installed smooth connector rod, which is welded to each embedded steel plate with a partial penetration weld. In addition two No.4 bars are welded to the back of each embedded steel plate with a full penetration weld and are lapped with the No.4 bars coming from the other side. Detail B shows the top view of this connection and Section C-C shows a section through it. The non-shrink grout and the waterproofing membrane may be omitted provided that there is a 21.5 in deep cast-in-place concrete topping over the longitudinal joints. This type of transverse connection is intended to provide a continuous tension tie in the transverse direction to resist the effects of transverse bending due to vehicular loads and emulate the behavior of a monolithic slab span bridge.

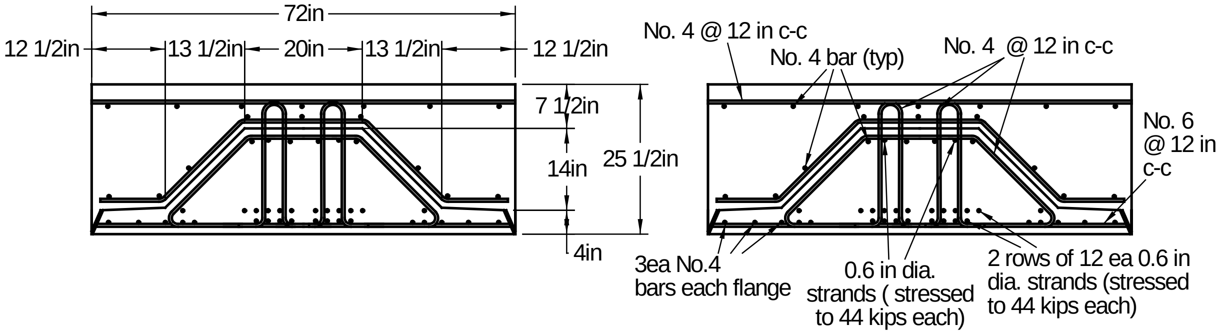

(a) (b)

Figure 18. (a) Typical Composite Cross-Section, (b) Typical Reinforcing Details. Note: c-c = center-to-center, typ = typical, ea = each.

Live Load Distribution Factors

One of the key design parameters for this bridge type is the live load distribution factor (LLDF). For cast-in-place slab span bridges AASHTO (2013) uses the equivalent strip width

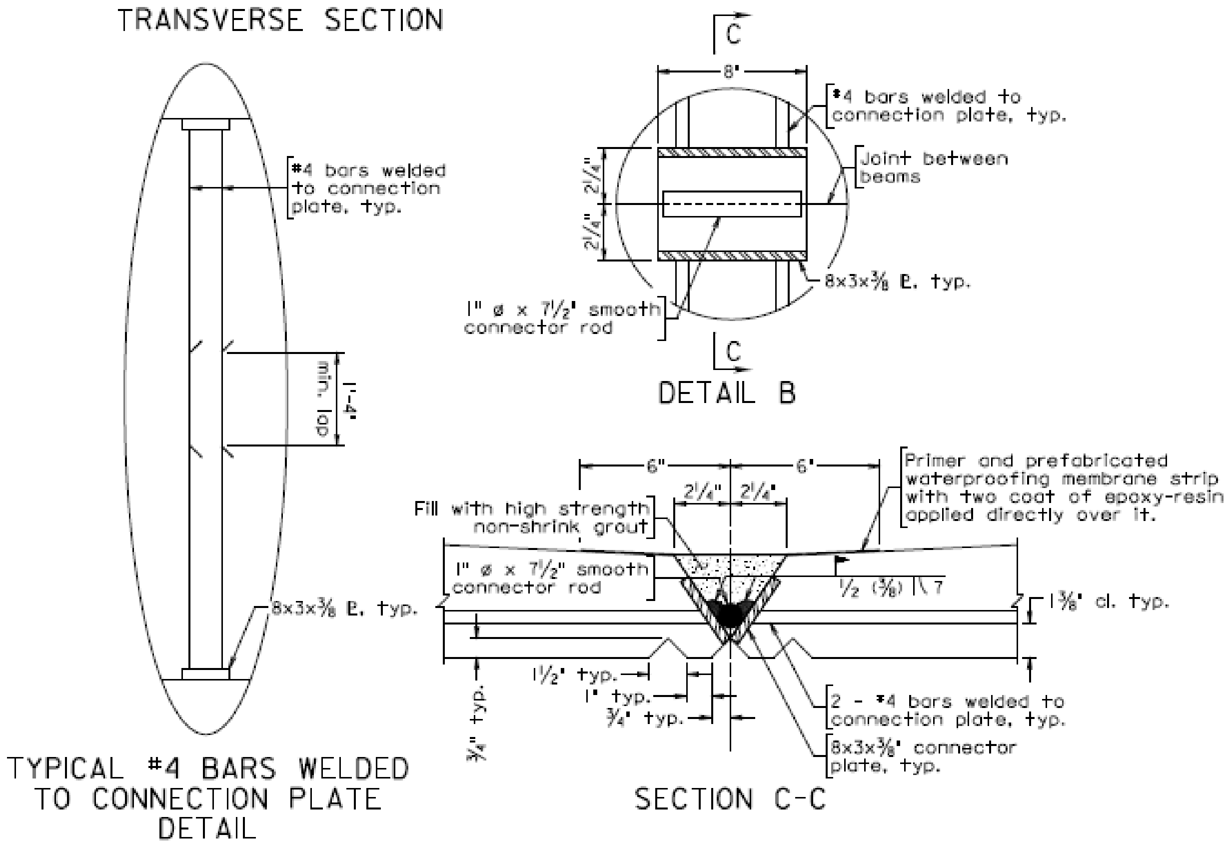
TRANSVERSE SECTION

TYPICAL #4 BARS WELDED TO CONNECTION PLATE DETAIL

DETAIL B

SECTION C-C

Figure 19. Transverse Connection Between Adjacent Precast Inverted T-Beams

method to determine how wide a strip can be used to resist design live loads. Equations 24 and 25 can be used to determine the equivalent strip width for one design lane loaded and for two or more design lanes loaded, respectively. In Equation 24 the strip width has been divided by 1.20 to account for the multiple presence effect.

$$E = 10.0 + 5.0\sqrt{L_1 W_1} \qquad \text{Eq. 24}$$

$$E = 84.0 + 1.44\sqrt{L_1 W_1} \leq \frac{12.0\,W}{N_L} \qquad \text{Eq. 25}$$

where

E = equivalent width, in

L_1 = modified span length taken equal to the lesser of the actual span or 60.0, ft

W_1 = modified edge-to-edge width of bridge taken to be equal to the lesser of the actual width or 60.0 for multilane loading, or 30.0 for single-lane loading

W = physical edge-to-edge width of bridge, ft

N_L = number of design lanes as specified in Article 3.6.1.1.1 of AASHTO.

Alternatively, for precast solid, voided, or cellular concrete boxes with shear keys and a cast-in-place concrete overlay AASHTO provides the equations shown in Table 2 for the calculation of live load distribution factors. The multiple presence factors have been included in

Table 2. Live Load Distribution Factors for Precast Solid, Voided or Cellular Concrete Boxes with Shear Keys and a Cast-in-Place Concrete Overlay*

Type of Superstructure	Distribution Factors	Range of Applicability
Moment in interior beams	One Design Lane Loaded: $g_{interior} = k\left(\frac{b}{33.3L}\right)^{0.5}\left(\frac{I}{J}\right)^{0.25}$ where: $k = 2.5\ (N_b)^{-0.2} \geq 1.5$ Two or More Design Lanes Loaded: $g_{interior} = k\left(\frac{b}{305}\right)^{0.6}\left(\frac{b}{12.0L}\right)^{0.2}\left(\frac{I}{J}\right)^{0.06}$	$30 \leq b \leq 60$ $20 \leq L \leq 120$ $5 \leq N_b \leq 20$
Moment in exterior beams	One Design Lane Loaded: $g = e\ g_{interior}$ $e = 1.125 + \frac{d_e}{30} \geq 1.0$ Two or More Design Lanes Loaded: $g = e\ g_{interior}$ $e = 1.04 + \frac{d_e}{25} \geq 1.0$	$d_e \leq 2.0$
Shear in interior beams	One Design Lane Loaded: $g_{interior} = \left(\frac{b}{130L}\right)^{0.15}\left(\frac{I}{J}\right)^{0.05}$ Two or More Design Lanes Loaded: $g_{interior} = \left(\frac{b}{156}\right)^{0.4}\left(\frac{b}{12.0L}\right)^{0.1}\left(\frac{I}{J}\right)^{0.05}\left(\frac{b}{48}\right)$ $\frac{b}{48} \geq 1.0$	$35 \leq b \leq 60$ $20 \leq L \leq 120$ $5 \leq N_b \leq 20$ $25{,}000 \leq J \leq 610{,}000$ $40{,}000 \leq I \leq 610{,}000$
Shear in exterior beams	One Design Lane Loaded: $g = e\ g_{interior}$ $e = 1.25 + \frac{d_e}{20} \geq 1.0$ Two or More Design Lanes Loaded: $g = e\ g_{interior}\left(\frac{48}{b}\right)$ $\frac{48}{b} \geq 1.0$ $e = 1 + \left(\frac{d_e + \frac{b}{12} - 12}{40}\right)^{0.5} \geq 1.0$	$d_e \leq 2.0$ $35 \leq b \leq 60$

*AASHTO, 2013.

the approximate equations for distribution factors provided in Table 2 for both single and multiple lanes loaded. The equations are based on evaluation of several combinations of loaded lanes with their appropriate multiple presence factors and are intended to account for the worst-case scenario. The following notation applies to Table 2:

N_b = number of beam, stingers or girders
b = width of beam, in
L = span of beam, ft
I = moment of inertia of the composite section, in^4

J = polar moment of inertia, in^4
g = distribution factor
d_e = horizontal distance from the centerline of the exterior web of exterior beam at deck level to the interior edge of curb or traffic barrier, ft.

Table 3 provides a comparison of live load distribution factors calculated based on AASHTO's methods for cast-in-place slab span and adjacent box structure systems. The method used for cast-in-place slab span systems does not distinguish between an interior and exterior strip. It also does not differentiate between live load distribution factors used for moment and shear. In contrast, the method used for adjacent box structure systems provides different equations for calculating live load distribution factors in interior and exterior beams, as well as for moment and shear.

The live load distribution factors shown in Table 3 were calculated for Phase I of the U.S. 360 Bridge as well as for the completed bridge. The differences in live load distribution factors between Phase I and the completed bridge are negligible and are primarily related to the difference in the number of beams and the width of the bridge. The live load distribution factors calculated for moment assuming an adjacent box structure system are similar to those calculated assuming a cast-in-place slab span system. However, there is a significant difference between the live load distribution factors for shear assuming an adjacent box girder system and those calculated assuming a cast-in-place slab span system. It should be noted that because the width of precast inverted T-beams is 72 in, it is outside the range of applicability of beam widths ($30 \leq b \leq 60$) for the adjacent box structure systems. However, LLDFs were calculated using for both systems because they represent the available options to the engineer when designing a composite bridge system with adjacent precast inverted T-beams.

Table 3. Comparison of Calculated Live Load Distribution Factors

Analysis Phase	Beam Location	Factor Type	Cast-in-place Slab Span System	Adjacent Voided/Box Structures
Phase I	Interior	Shear	0.52	0.86
		Moment		0.47
	Exterior	Shear		0.86
		Moment		0.47
Completed Bridge	Interior	Shear	0.46	0.86
		Moment		0.40
	Exterior	Shear		0.86
		Moment		0.42

Previous Studies

French et al. (2011) combined numerical modeling with observations from a live load truck test on a bridge in Center City, MN along with load distribution tests of laboratory bridge specimens to determine the applicability of current live load distribution factors in AASHTO for cast-in-place slab-span bridges. The numerical modeling, field tests and laboratory tests were conducted for composite bridges constructed with adjacent precast inverted T-beams with straight webs and covered with a cast-in-place topping. In addition, the transverse connection between adjacent members featured transverse bars with 90^{o} hooks that protruded from the sides of the precast webs and lapped with those extending from the adjacent member. A total of nine finite element models were created which featured bridges built with monolithic slab-spans and those built with precast inverted T-beams with longitudinal joints. Most of the bridge models featuring precast inverted T-beams incorporated the presence of a 3 in longitudinal joint with the exception of one model which featured a 15 in longitudinal crack, which extended to within 3 in of the extreme compression fiber. The purpose of the model with an induced crack was to simulate the presence of a reflective crack.

The numerical models illustrated that the longitudinal curvatures measured in the inverted T-beam system with a reflective crack extending to within 3 in of the extreme compression fiber and a tandem load greater than that which could be physically applied in the field, were only 84 percent of the longitudinal curvatures predicted using the AASHTO's distribution factors for cast-in-place slab span bridges. This observation suggested that Minnesota's precast inverted T-beam system could reasonably and conservatively be designed using the current live load distribution factors for monolithic slab type bridges.

In addition, the results from the live load truck test on the Center City Bridge suggested that the measured longitudinal curvatures were approximately one third the magnitude calculated using monolithic slab span equations.

Laboratory tests were conducted on specimens with and without induced reflective cracking to investigate the capability of the system to transfer load from one beam to the adjacent beam. Little variation in the measured longitudinal curvatures was observed in the unloaded panels compared to loaded panels, which suggested that the load was effectively transferred across the longitudinal joint despite the presence and increase in the size of reflective cracking induced in/near the joint.

As stated earlier, the studies performed by French et al. (2011) were conducted on the precast inverted T-beam system with straight precast webs. In addition, the connection between adjacent precast members featured extended bars that protruded from the precast webs and lapped with the extended bars from the adjacent members. The precast inverted T-beam system used in Virginia features tapered precast webs and the connections between adjacent precast members consist of discrete embedded steel plates and welded bars (Figure 19). Therefore, the purpose of the research presented in this section was to determine the applicability of the available methods in AASHTO for calculating live load distribution factors for Virginia's inverted T-beam system.

Preliminary Analytical Investigation

Before the live load test on Phase I of the U.S. 360 Bridge was conducted, a beam line model representing the two-span continuous beam was created in RISA with the purpose of determining the position of the controlled vehicle (VDOT truck) on the East span (*span b*, see Figure 7) that created the worst case positive bending moment at mid-span. The beam line model consisted of a prismatic beam section supported on rollers supports at the abutments and on two pin supports at the intermediate pier. The distance between the pin supports at the intermediate pier represented the distance between the centerlines of bearing of the precast inverted T-beams. The distance from the roller supports to the end of the beam line represents the distance from the centerline of bearing of the precast inverted T-beams to the edge of the superstructure. The moment envelope for the moving controlled vehicle is shown in Figure 20. The maximum positive moment was 237 ft-kips. The maximum positive moment at mid-span was approximately 210 ft-kips. To create the worst case positive moment at mid-span, the inner rear axle was positioned at mid-span (Figure 21). This truck position was used during field testing to create maximum longitudinal strains.

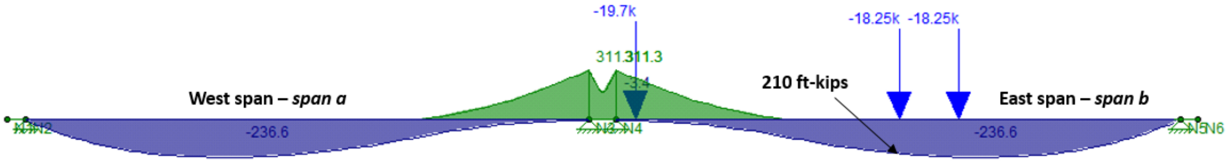

Figure 20. Moment Envelope Due to Moving Controlled Vehicle

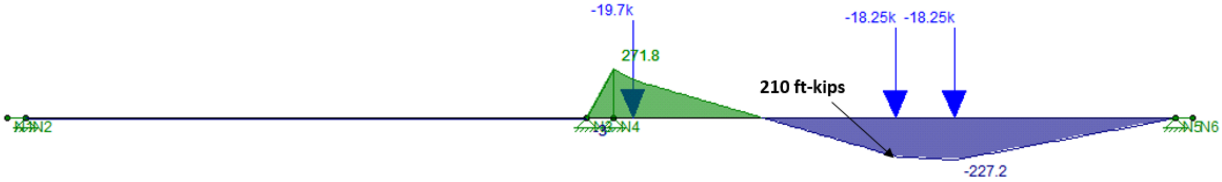

Figure 21. Controlled Vehicle Position to Create the Maximum Positive Moment at Mid-Span

Table 4 provides a summary of service level design moments, the moments created by the controlled vehicle and the positive and negative cracking moments for a typical composite section. The design live load moments were based on a LLDF calculated assuming a cast-in-place slab span. The goal of the live load test was to create measurable longitudinal tensile strains at the bottom of each precast inverted T-beam but not exceed the service level design moments nor cause any cracking on the bridge. The maximum longitudinal mid-span tensile strain created due to the controlled vehicle on the east span calculated using the positive moment from the beam line model and the LLDF assuming a cast-in-place slab span is 31 microstrain. A preliminary test on the strain gages showed that they could report reasonably stable strain measurements within the range of +- 1 microstrain. The maximum positive design moment due to superimposed loads is 396 ft-kips and the maximum positive moment due to the controlled vehicle is 123 ft-kips. In addition, the maximum negative design moment due to superimposed loads is 355 ft-kips and the maximum negative moment due to the controlled vehicle is 162 kips. The positive and negative cracking moments due to superimposed loads are 558 ft-kips and 423 ft-kips, respectively. As can be seen the moments created due to the controlled vehicle were smaller than the service level design moments and cracking moments.

Field Testing

The live load test was conducted on Phase I of the U.S. 360 Bridge (Figure 22) and was executed the day before this phase was opened to traffic. Each precast inverted T-beam was instrumented with surface mounted gages oriented in the longitudinal direction. The gages were manufactured by Bridge Diagnostic Incorporated and are referred to herein as BDI gages. These gages were placed at mid-span of the east span. Figure 23 illustrates the location of gages at the bottom of each precast inverted T-beam. With the exception of the exterior precast inverted T-beams, BDI gages were installed at mid-width of each beam and at 6 in from the edge of the precast flange. For the two exterior beams only two gages were installed, one at mid-width and another one at 6 in away from the edge of the precast flange.

Table 4. Service Level Moments for Each Composite Beam (ft-kip)

Service I Design Moments*		**Maximum Controlled Vehicle Moment*^**		**Cracking Moment▼**	
Component	**Moment ft-kip**	**Component**	**Moment ft-kip**	**Component**	**Moment ft-kip**
Inverted T-beam (M_{invT})	173	+Truck ($+M_{truck}$)	123	+Cracking ($+M_{crack}$)	558
Deck (M_{deck})	231				
+Design Live Load ($+M_{live}$)	336				
-Design Live Load ($-M_{live}$)	248				
+Superimposed Dead Load ($+M_{superD}$)	60	-Truck ($-M_{truck}$)	162	-Cracking ($-M_{crack}$)	423
-Superimposed Dead Load ($-M_{superD}$)	107				
$+M_{service} = M_{invT}+M_{deck}+M_{live}+M_{superD}$	800				
$+M_{super} = +M_{live}+M_{superD}$	396				
$-M_{super} = -M_{live}-M_{superD}$	355				

*Design live load moments based on LLDF = 0.52.
^Based on beam-line model.
▼For composite beam and due to superimposed loads.
Note: (+) = positive, (-) = negative.

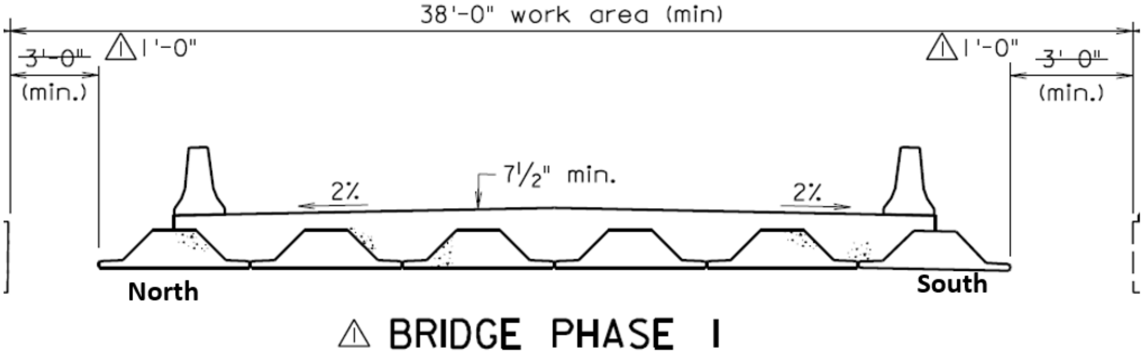

Figure 22. U.S. 360 Bridge - Phase I

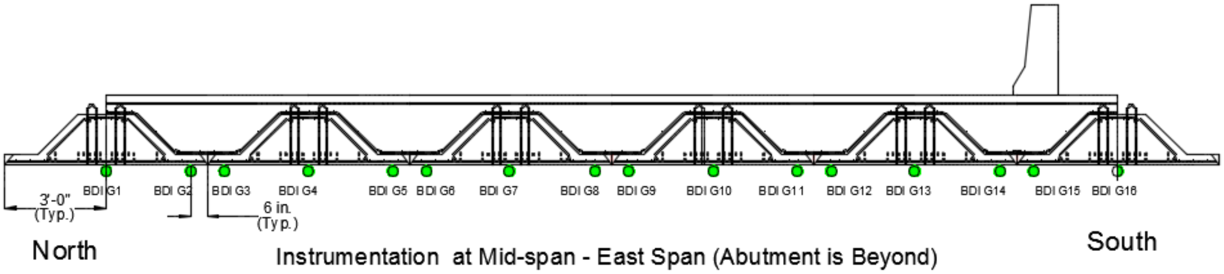

Figure 23. Location of Surface-Mounted BDI Gages

The VDOT truck used for load testing was a three-axle dump truck that was loaded with gravel from a nearby rock quarry and weighed before it arrived at the bridge site. The truck weight was 56.2 kips when filled with gravel. The weight of the front axle was 19.7 kips and the combined weight of the rear axles was 36.5 kips. The distance between the front axle and the near most rear axle was 19 ft 1 in and the distance between the rear axles was 4ft 4 in (Figure 24).

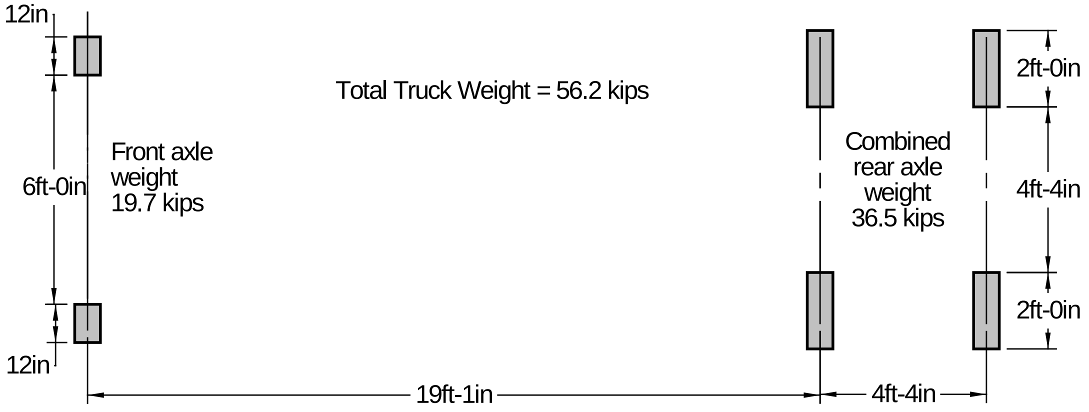

Figure 24. Truck Axle Weight and Distances

Four static truck tests were conducted. As stated earlier, the truck was positioned such that the inner rear axle aligned with the mid-span of the east span to create the maximum positive moment at mid-span, which is where the longitudinal strain gages were installed. Four transverse truck positions were investigated with the purpose of measuring longitudinal strains under each precast beam and investigating the distributions of these strains across the width of the bridge (Figure 25).

The truck position for Test 1 was selected such that the tires were predominately over the precast webs and the center of the truck aligned with the center of the bridge. The truck position for Test 2 was selected such that the wheel loads were predominately over the longitudinal joints. Figure 25 shows the location of the front wheels in the transverse cross-section of Phase I for each truck configuration. Because the width of the rear wheels was greater than the front wheels they covered a larger area of the precast webs in Test 1 and a larger area of the longitudinal joints in Test 2. The truck configuration for Test 3 was selected such that the south most precast beams would carry the majority of the load. During this test the truck was positioned such that the side of the wheels was aligned with inner edge of the barrier. Finally, the truck configuration for Test 4 was selected such that the north most precast beams carried the majority of the load. Tests 1 and 2 were intended to induce maximum longitudinal strains in the interior beams, whereas Tests 3 and 4 were intended to induce maximum longitudinal strains in the exterior beams. LLDFs were calculated by dividing the longitudinal strains at mid-width of each beam by the sum of the longitudinal strains at mid-width of all beams.

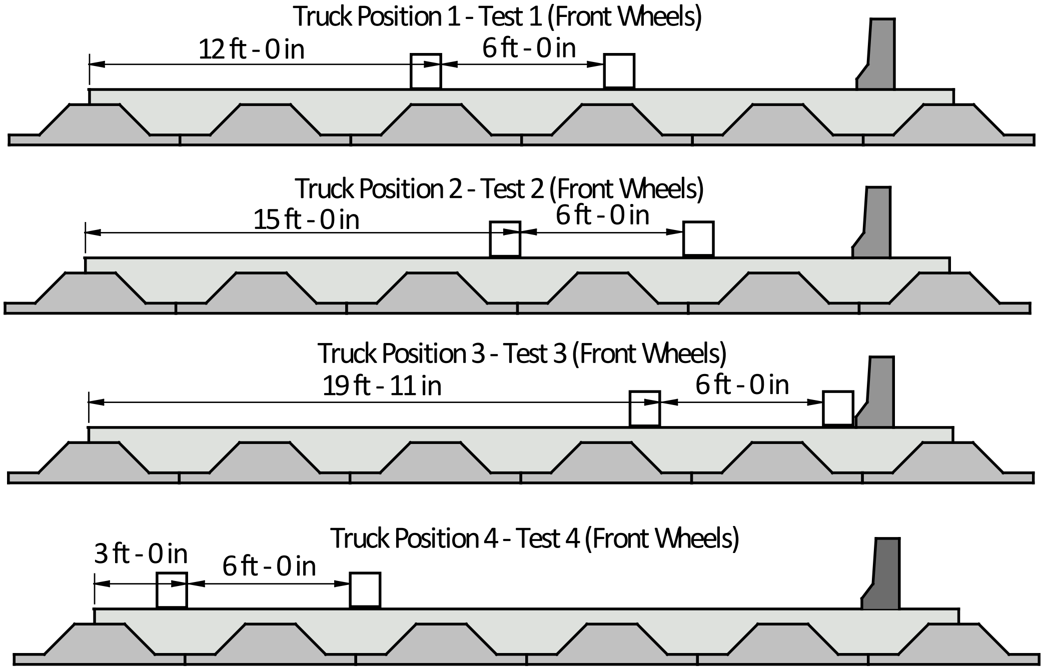

Figure 25. Location of Controlled Vehicle During Live Load Tests

Finite Element Analyses

After the live load test was completed two finite element models of Phase I of the U.S. 360 Bridge were created with the purpose of determining whether the behavior of the bridge could be accurately simulated using finite element analyses and to investigate additional cases which were outside the scope of the live load test. The commercially available finite element software ABAQUS (2012) was used to conduct the analyses. One of the finite element models had no barriers whereas the other had one continuous barrier. The actual behavior of the bridge was expected to be bracketed by the results from these two models because the actual barrier provided some additional stiffness along the east edge of the bridge but was not continuous. 3D solid elements were used to model the individual precast inverted T-beams, the cast-in-place topping and the continuity diaphragm. The bond between the precast surfaces and the cast-in-place topping was modeled as a perfect bond. In addition, the bond between the top of the cast-in-place topping and the bottom of the barrier was also modeled as a perfect bond in the model that featured the barrier. The boundary conditions were modeled as roller supports at the abutments and pin supports at the intermediate pier. Truck wheel loads matched those of the controlled vehicle used during the live load test. The wheel loads were applied as a uniformly distributed pressure over the tire prints illustrated in Figure 24. No dynamic load allowance was used to be consistent with the four static truck tests conducted in the field. Because no cracking was expected during the live load test a linear elastic analysis was conducted. The moduli of elasticity were based on the design compressive strengths and were calculated using the equations in AASHTO. Poisson's ratio was taken as 0.2.

Both models were loaded with all four truck positions investigated during the live load test so that longitudinal strains recorded during the live load test could be compared with those obtained analytically. Longitudinal strains were recorded at the same locations where the BDI gages were installed on the bridge. Figure 26 shows longitudinal strain contours for Truck Position 4.

Because AASHTO's method for calculating LLDFs in adjacent box structures yields different values for moment and shear, four additional cases were investigated in both models with the purpose of calculating live load distribution factors for shear. In these four additional cases the position of the controlled vehicle in the model in the longitudinal direction was chosen such that it caused the maximum shear at the critical section near the intermediate support (Figure 27). The locations of the truck in the transverse direction matched those used at mid-span. LLDFs for shear were calculated by dividing each beam reaction at the interior support by the sum of reactions. This additional investigation was performed to determine whether there is a significant difference between LLDFs calculated based on longitudinal strains at mid-span and those calculated based on the beam reaction at the intermediate support.

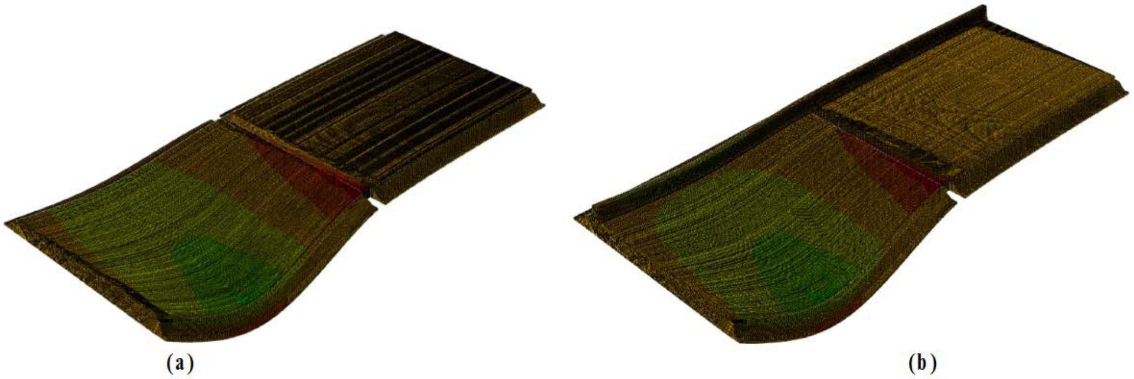

Figure 26. Longitudinal Strain Contours Due to Truck Position 4; (a) No Barrier, (b) With One Continuous Barrier

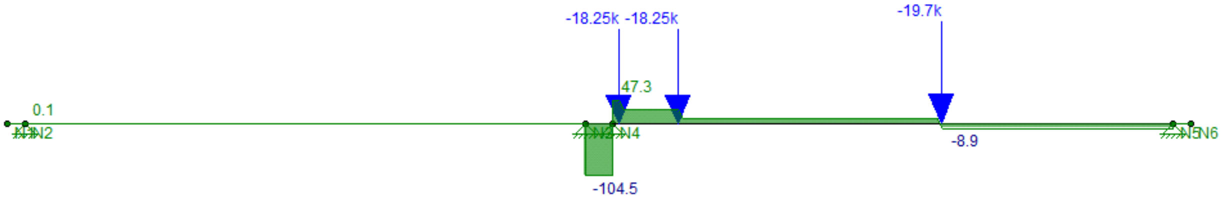

Figure 27. Controlled Vehicle Position to Create the Maximum Shear at the Critical Section

RESULTS

Investigation of Time-dependent and Temperature Effects

Figure 28(a) shows the stress distributions in Sections 1, 2 and 3 caused by differential shrinkage and shrinkage induced creep. In the figure, tensile stresses are positive and compressive stresses are negative. The stress distribution shown for Section 1 applies at the portion of this section where the thickness of the precast inverted T-beam is 18 in and the thickness of the cast-in-place topping is 7 in. The maximum tensile stresses at the bottom of the cast-in-place topping in Sections 1, 2 and 3 are 0.370 ksi, 0.496 ksi and 0.487 ksi, respectively. The modulus of rupture (f_r) for the deck is 0.474 ksi (based on $7.5\sqrt{f'c}$ where f'_c= 4000 psi). This highlights the potential of differential shrinkage to cause longitudinal cracking in the deck. The maximum tensile stresses at the bottom of the deck and at the bottom of precast inverted T-beam in Section 1 are lower than the ones in Section 2. As mentioned earlier, this is due to the fact that the moment arm between the centroids of the cast-in-place topping and the precast beam in Section 1 is lower than in Section 2. This promotes the utilization of the inverted T-beam

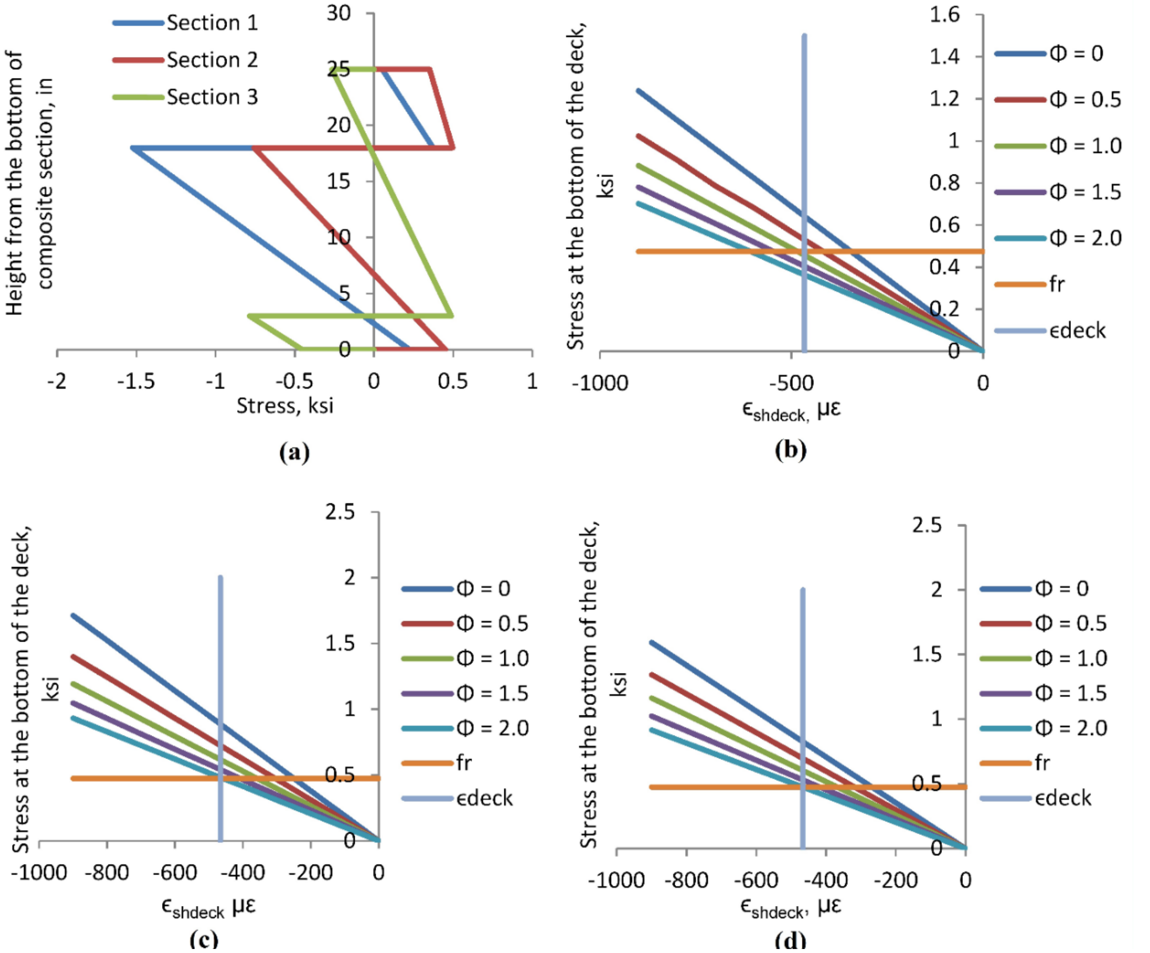

(a) (b)

(c) (d)

Figure 28. (a) Stress Distribution Due to Differential Shrinkage and Shrinkage Induced Creep in All Three Cross-Sections; (b) , (c), and (d) Sensitivity of Tensile Stress at the Bottom of the Deck to Shrinkage and Creep Properties of the Deck for Sections 1, 2, and 3, Respectively.

system as opposed to a voided slab system or adjacent box girder system, considering that Section 2 represents a similar section in the transverse direction in both of these systems, in addition to the longitudinal direction. The compressive stress at the top of the precast inverted T-beam is higher in Section 1 than in Section 2 due the higher volume of concrete. However, given that the weakness of the concrete is its tensile strength, this will not control design.

Figures 28(b), (c), and (d) show the sensitivity of the tensile stress at the bottom of the deck to shrinkage and creep properties of the deck for Sections 1, 2, and 3, respectively. The horizontal and the vertical lines represent the modulus of rupture and the ultimate shrinkage strain for the deck, respectively. For example in Section 1 for a creep coefficient $\phi=2$, there is a 78 psi decrease in the tensile stress for every 100 $\mu\epsilon$ decrease in the ultimate shrinkage strain of the topping mix (ϵ_{shdeck}). Similarly, for an ultimate shrinkage strain of $\epsilon_{shdeck} = -500\text{x}10^{-6}$ there is a 119 psi decrease in the tensile stress for every increase by 0.5 in the creep coefficient. Clearly a mix with lower free shrinkage and high creep will be ideal from the standpoint of reducing tensile stresses as a result of differential shrinkage. High creep properties are desired to relieve the stresses developed as a result of differential shrinkage. Low shrinkage in the deck is desired to minimize the amount of differential shrinkage, provided that most of the shrinkage in the precast beam has already taken place.

The presence of mild steel in the deck restrains the free shrinkage of the deck and as a result creates additional tensile stresses. Figure 29 shows the sensitivity of the tensile stress at the bottom of the deck to the amount of mild steel. In Figure 29(a) A_{smild1}, A_{smild2} and A_{smild3} represent the variation in areas of mild steel in the deck in the longitudinal direction at different elevations. These are denoted as A_{s1}, A_{s2} and A_{s3} in Figure 8 - Section 1, respectively. In Figure 29(b) and (c) A_{smild1} and A_{smild2} represent the variation in areas of mild steel in the deck in the transverse direction at different elevations. These are denoted as A_{s1} and A_{s2} in Figure 8, Section 2 and Section 3, respectively. The vertical lines in Figure 29 represent the actual amounts of mild steel in the deck, which were based on the design of the U.S. 360 Bridge per AASHTO LRFD Bridge Design Specifications. It can be seen that while the magnitude of the tensile stress at the bottom of the deck increases with an increase in the amount of mild steel, this increase is almost negligible. As a result mild steel needs to be provided in the deck in both directions to control the width of potential cracks and it does not significantly increase the likelihood of cracking.

Figure 30 shows stress distributions in Sections 1, 2 and 3 due to negative and positive temperature gradients. The largest negative temperature gradient tensile stress is at the top of the deck and is slightly higher than the largest tensile stress created as a result of a positive temperature gradient (0.15 ksi versus 0.11 ksi). These stresses are lower than the modulus of rupture (0.474 ksi) for the concrete topping. Therefore, temperature gradients alone cannot create high enough tensile stresses to cause cracking. However, when the effects of differential shrinkage and temperature gradients are combined, then these stresses exceed the rupture stress.

Table 5 presents a summary of the stresses created at the top and bottom of the deck, respectively. The top of the deck is likely to experience longitudinal cracking above the web of the precast girder due to the combined effects of differential shrinkage and temperature gradient. The bottom of the deck will be subject to transverse and longitudinal cracking. It is important to note that the analysis performed at the cross-sectional level shows stress distributions that apply along the entire bridge superstructure. Therefore, if the tensile stresses in the deck are higher than its modulus of rupture, cracks could potentially develop along the entire bridge length and width.

Time-Dependent and Temperature Analysis at the Structural Level

Figure 31(a) shows the stress distribution in the composite cross-section due to axial restraint at the abutments. The axial stresses due to axial restraint against negative temperature gradient in the topping and the precast beam are small (0.042 ksi and 0.060 ksi, respectively). However, the axial stresses due to axial restraint against differential shrinkage and a uniform decrease in temperature are at least 35% greater than the modulus of rupture (0.641 ksi and 0.906 ksi due to differential shrinkage and 0.965 ksi and 1.501 ksi due to a uniform decrease in temperature). The sensitivity of the stress in deck to the shrinkage and creep properties of the deck is illustrated in Figure 31(b). The horizontal and vertical lines represent the modulus of rupture and ultimate shrinkage strain for the deck, respectively. If the creep coefficient is assumed to be $\phi = 2.0$ then there is a 136 psi decrease in the tensile stress in the deck for every 100 $\mu\epsilon$ decrease in shrinkage strain.

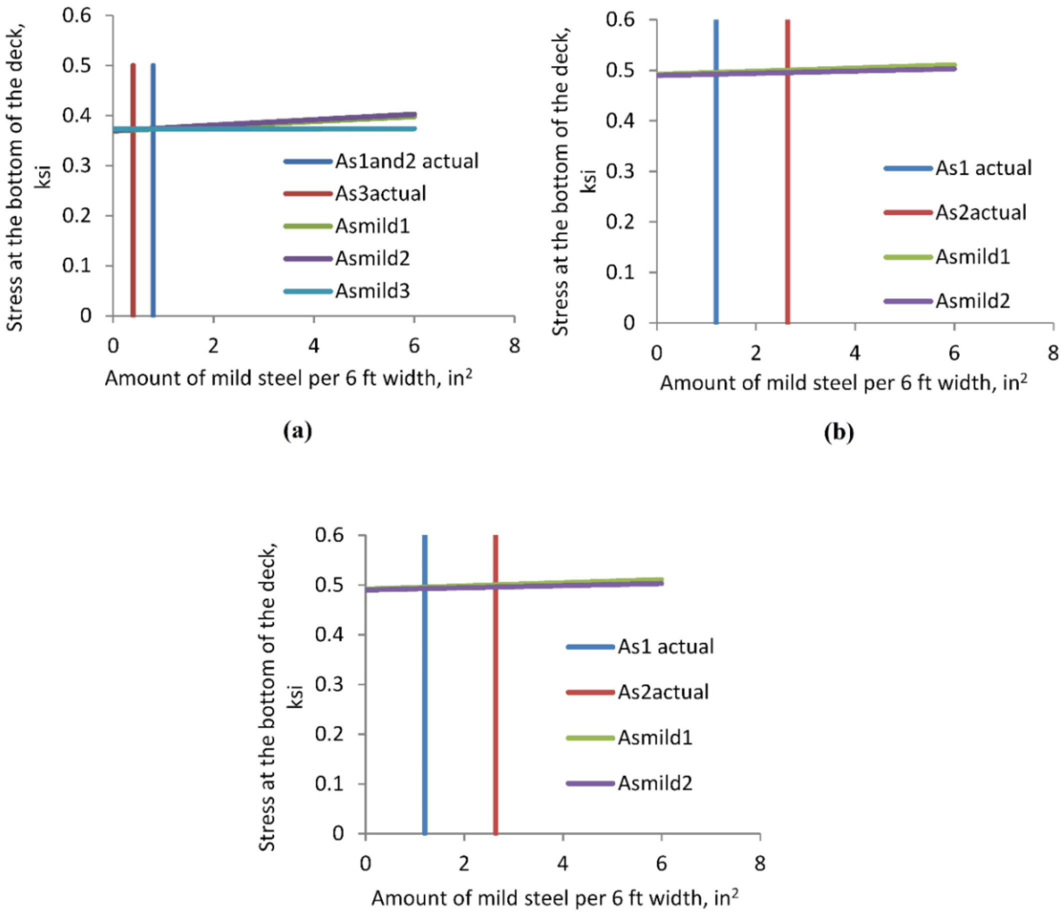

(a)

(b)

(c)

Figure 29. Sensitivity of Tensile Stress at the Bottom of the Deck to the Amount of Mild Steel in Sections 1, 2, and 3, Respectively

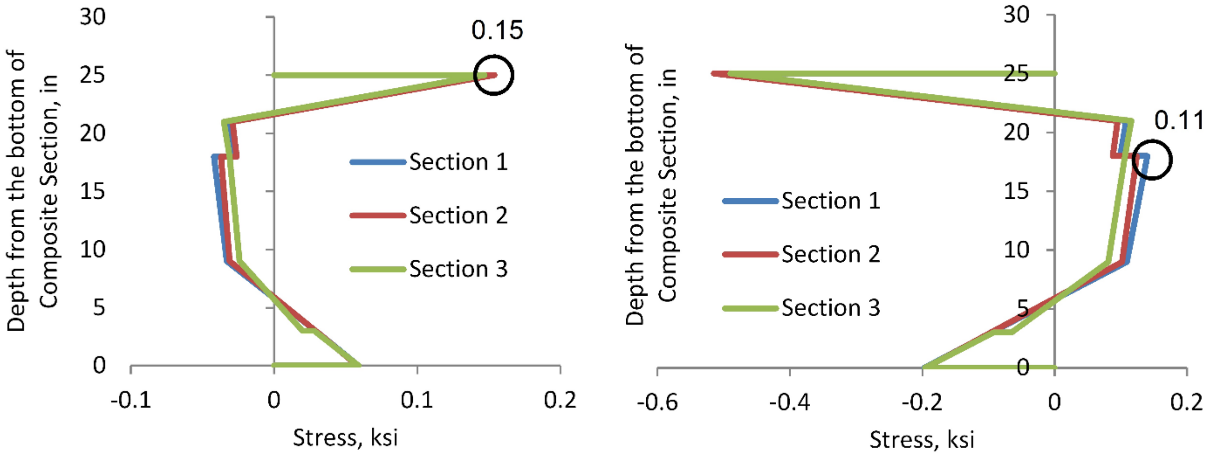

(a) (b)

Figure 30. (a) Stress Distribution - Negative Temperature Gradient, (b) Stress Distribution - Positive Temperature Gradient

Table 5. Tensile Stresses at the Top and Bottom of the Deck Due to Differential Shrinkage and Temperature Gradient

Tensile stresses at the top of the deck					
Section	**Differential Shrinkage, ksi**	**Temperature Gradient, ksi**	**Total, ksi**	**f_r, ksi**	**Total/f_r**
1	0.052	0.150	0.202	0.474	0.43
2	0.352	0.154	0.506	0.474	1.07
3	-0.264	0.150	-0.114	0.474	N/A

Tensile stresses at the bottom of the deck					
Section	**Differential Shrinkage, ksi**	**Temperature Gradient, ksi**	**Total, ksi**	**f_r, ksi**	**Total/f_r**
1	0.373	0.100	0.473	0.474	1.0
2	0.496	0.090	0.586	0.474	1.24
3	0.487	0.020	0.507	0.474	1.07

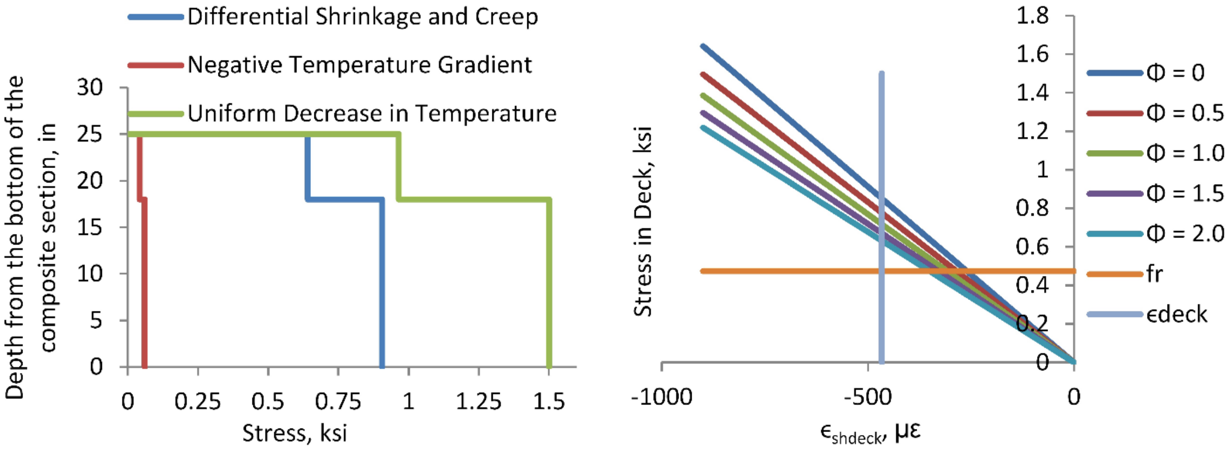

(a) (b)

Figure 31. (a) Stress Distribution in Section 1 Due to Potential Axial Restraint at the Abutments in the Longitudinal Direction; (b) Sensitivity of Stress in Deck to Shrinkage and Creep Properties of the Deck

Similarly, if the free ultimate shrinkage strain of the deck is assumed to be $\epsilon = -500\ \mathrm{x}10^{-6}$, then there is an 81 psi decrease in the tensile stress in the deck for every increase by 0.5 in the creep coefficient. As a result, to reduce the likelihood of excessive transverse cracking, axial movement in the longitudinal direction should be accommodated at the abutments. If this movement is restrained, then a topping mix with low shrinkage and high creep will help reduce the tensile stresses. Tensile stresses developed as a result of axial restraints at the abutments in the longitudinal direction due to differential shrinkage, negative temperature gradient and a uniform decrease in temperature apply not only to the entire bridge superstructure but are also constant throughout the depth of the cross-sections. These high tensile stresses have the potential to develop full depth transverse cracks. In addition to the obvious serviceability and durability problems that these high tensile stresses can create, full depth cracks in regions of small moment can cause reductions in shear strength.

Figure 32(a) shows how the stress in the deck due to a uniform decrease in temperature is affected by creep and aging coefficients. The calculation of the restraining axial force at the abutments due to a uniform change in temperature was based on Equation 26. This equation was derived based on the principle of deformation compatibility and the fact that the deck concrete will creep and age whereas the precast girder has already aged and crept when continuity is established. For a fixed aging coefficient of 0.7, the higher the creep coefficient the lower the tensile stress. The tensile stress values in the deck vary from 1.50 ksi when the creep coefficient is zero to 0.97 ksi when the creep coefficient is 2.0. The corresponding values for the precast beam are 2.32 ksi and 1.50 ksi, respectively. Similarly, for a fixed creep coefficient in the deck equal to 2.0, the higher the aging coefficient the lower the tensile stress. This is illustrated in Figure 32(b). The tensile stress values in the deck vary from 0.965 ksi when the aging coefficient is 0.7 to 0.89 ksi when the aging coefficient is 1.0. The corresponding values for the precast beam are 1.50 ksi and 1.384 ksi, respectively. This highlights the advantage of a concrete mix that has high creep and does not age significantly. The influence of a higher creep coefficient is more pronounced in reducing the tensile stresses in the deck and the precast beam compared to the aging coefficient. Consequently priority should be given to a mix that has high creep.

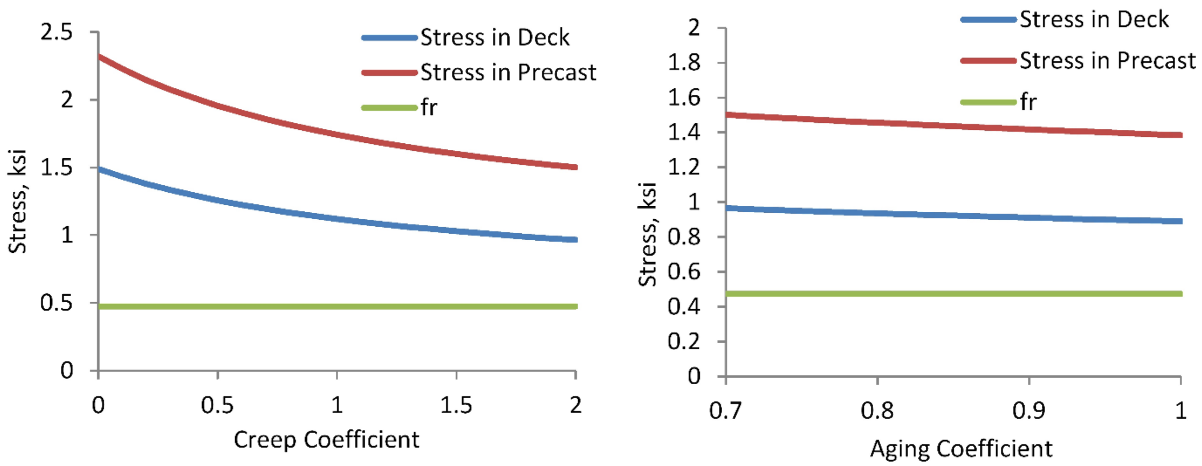

(a) (b)

Figure 32. Sensitivity of Stress in Deck and in the Precast Inverted T-Beam Due to a Uniform Decrease in Temperature to (a) Creep Coefficient and (b) Aging Coefficient

$$N_{restraint} = \frac{\alpha \Delta T_{uniform} E_G A_{transformed}}{1+\frac{A_D \mu_D \varphi_D}{A_D + A_G(1+\mu_D \varphi_D)}} \qquad \text{Eq. 26}$$

where

α = coefficient of thermal expansion
$\Delta T_{uniform}$ = uniform change in temperature
E_G = modulus of elasticity of the precast inverted T
$A_{transformed}$ = transformed area of the composite section
A_D, A_G = area of the deck, area of precast inverted T
μ_D = aging coefficient for deck concrete
φ_D = creep coefficient for deck concrete

It should be noted that in the analysis performed in this study the axial restraining stiffness of the abutments was taken equal to infinity. Additionally, the creep coefficient for the precast beams was taken equal to zero because, as stated earlier, it is believed that if the age of continuity is at least 90 days most of the creep in the precast beams has already taken place. In reality the axial restraining stiffness of the abutments will be smaller than infinity and the creep coefficient for the precast beam will be higher than zero. As a result, the stresses created in the deck and the precast beam may be slightly lower than the values presented in this report.

Table 6 provides a summary of differential shrinkage moments calculated using various methods. The method proposed by Peterman and Ramirez (1998) is simple to use and estimates a differential shrinkage moment which is only 11% different from the one calculated using Menn's Method (Menn, 1990). The PCA method (Mattock 1961, Freyermuth, 1969) provides a more conservative estimate of the differential shrinkage moment. This is a result of the fact that the PCA Method does not account for the restraining effect that the precast girder and reinforcing steel have on the free shrinkage of the deck. In this paper, only one time step was used to calculate the differential shrinkage moment using the CTL method (Oesterle et al., 1989).

Table 6. Summary of Differential Shrinkage Moments Using Various Methods

Method	Differential Shrinkage Moment, ft-kips	% difference with Menn's Method
Menn (1990)	646	——
PCA (Mattock 1961, Freyermuth (1969)	1393	216%
CTL (Oesterle et al., 1989)*	724	12%
Peterman and Ramirez (1998)	714	11%

Note: * Using only one time step.

Tensile stresses developed as a result of moment restraint due to differential shrinkage and negative/positive temperature gradients are maximum at the intermediate support and reduce linearly toward the abutments (for a two-span continuous bridge). Because a positive temperature gradient causes a positive restraint moment at the intermediate support its effects were not investigated because the focus of this paper was potential cracking on the top surface of the deck. As stated earlier the analysis performed in this study assumes an age of continuity equal to at least 90 days, which represents a best case scenario for reducing positive restraint moments, and a worst case scenario for developing negative restraint moments.

Figure 33(a) shows the stresses in the composite cross-section due the negative restraint moments caused by differential shrinkage and negative temperature gradients. The corresponding maximum tensile stresses in the deck are 1.291 ksi and 0.145 ksi, respectively. The stresses at the top of the precast inverted T-beam due to negative temperature gradient and differential shrinkage are 0.098 ksi and 0.870 ksi, respectively. Table 7 provides a summary of these values as well as the ratio of the total tensile stress due to negative temperature gradient and differential shrinkage to the modulus of rupture. The tensile stresses created as a result of

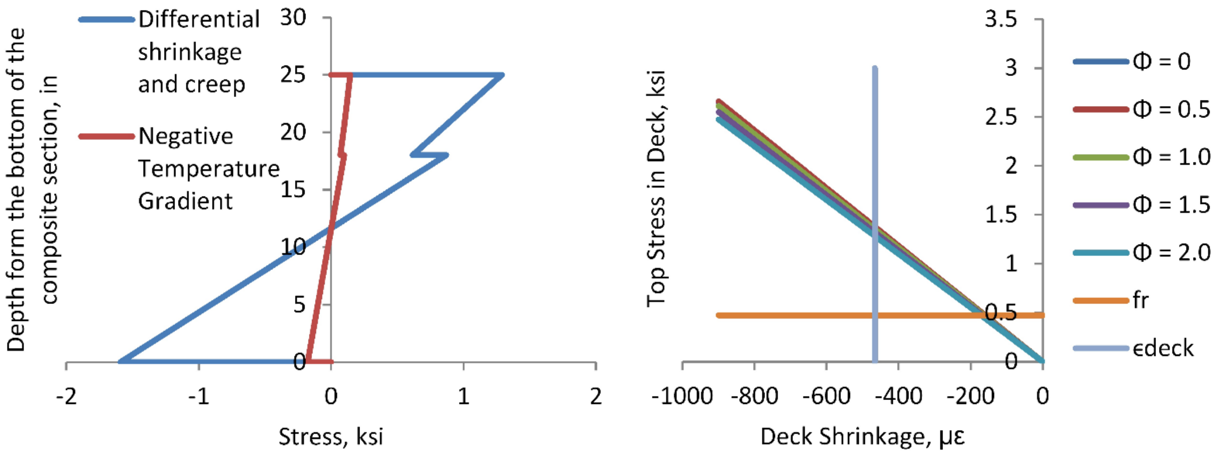

(a) **(b)**

Figure 33. (a) Stress Distribution in Section 1 Due to Differential Shrinkage/Creep and Negative Temperature Gradient; (b) Sensitivity of Tensile Stress at the Top of Deck to Shrinkage and Creep Properties of the Deck

negative temperature gradient are smaller than the modulus of rupture for the deck (0.474 ksi), whereas those created from differential shrinkage are more than 2.7 times. It can be seen that the sum of negative restraint moments creates tensile stresses in the deck and precast inverted T-beam that are well past the modulus of rupture.

Table 7. Stresses Due to Negative Restraint Moments

Location	**Negative Temperature Gradient, ksi**	**Differential Shrinkage, ksi**	**Total, ksi**	**f_r, ksi**	**Total/f_r**
Top of the deck	0.145	1.291	1.436	0.474	3.03
Top of precast section	0.098	0.87	0.968	0.671	1.44

Figure 33(b) shows the sensitivity of the maximum tensile stress in deck to the shrinkage and creep properties of the deck. The horizontal and vertical lines represent the modulus of rupture and the ultimate shrinkage strain for the deck, respectively. It can be seen that while the maximum tensile stress in the deck is sensitive to the ultimate shrinkage strain, it is not that sensitive to the creep coefficient of the deck. If the creep coefficient is assumed to be 2.0 than there will be a 275 psi decrease in the tensile stress for every 100 $\mu\varepsilon$ reduction in the free ultimate shrinkage strain of the deck.

The negative moments due to superimposed dead and live loads at service for the U.S. 360 Bridge are 107 kip-ft and 219 kip-ft, respectively. The restraint moment due to differential shrinkage and shrinkage induced creep is 909 kip-ft, which is nearly 2.8 times greater than the sum of the negative moments due to dead and live loads. The negative restraint moment due to negative temperature gradient is 102 kip-ft, which is slightly lower than the negative moment due to superimposed dead loads. Table 8 summarizes the magnitudes of negative moments at the interior support. This highlights the significance of negative restraint moments developed as a result of time-dependent effects in terms of magnitude. Menn (1990) states the following in his book *Prestressed Concrete Bridges*: “Theoretically no sectional forces are present at the ultimate limit state due to restrained deformations in ductile systems. In general, restrained deformations are significant only for the behavior of structures under service load conditions with regards to cracking and deflections.” This is due to the fact that a ductile system can accommodate imposed curvatures and axial strains by the formation of plastic hinges and yielding of the reinforcing steel. Consequently, while these high restraint moments do not present a safety concern they do need to be controlled to reduce the likelihood of excessive cracking. In this regard, specifying an optimized age of continuity in which the competing effects of negative and positive restraint moments would cancel each other as much as possible is essential. High positive restraint moments negate the effects of negative live load moments and may render a continuous design even more expensive than a design based on simply supported beams. High negative moments may create excessive cracking on the bridge decks and reduce the service life of bridges.

Table 8. Negative Moments at Interior Support

Load Cases	Moments, ft-kips
Superimposed Dead Load ($M_{negsuperDL}$)	107
Superimposed Live Load ($M_{negsuperLL}$)	219
Shrinkage + Creep ($M_{negSH+CR}$)	909
Negative Temperature Gradient (M_{negTG})	102
Ratios	
$M_{negSH+CR}$ / ($M_{negsuperDL}$ + $M_{negsuperLL}$) = 2.8	
M_{negTG} / ($M_{negsuperDL}$ + $M_{negsuperLL}$) = 0.3	

Investigation of End Zone Stresses

This section presents the results of the studies of the end zone stresses in the inverted-T beams.

U.S. 360 Bridge Girder (41.5 ft Span)

Vertical Plane - Case 1

A distribution of normal stresses along the depth of the precast beams is shown in Figure 34(a). Figure 34(b) also shows a longitudinal cut and illustrates how the magnitude of the spalling stresses diminishes away from the ends of the precast beam. The maximum tensile stress estimated at the nodes of the elements along the depth of the precast beam was 2.44 ksi, which is much higher than the modulus of rupture of the precast beam when the strands were detensioned. The modulus of rupture was taken equal to $0.23\sqrt{f'_c}$, where f'_c is in ksi. For a design compressive strength at transfer equal to f'_{ci} = 5 ksi the modulus of rupture is approximately 0.51 ksi. Because a visual inspection of the 37 precast beams used in the construction of the U.S. 360 Bridge (36 production beams + 1 trial), showed no signs of cracking at the end zones, such a modeling technique was deemed unrealistically conservative for designing the pretensioned anchorage zones. This conclusion is corroborated by previous studies, which report that tensile stresses in the end zone are affected by the transfer length (Base, 1958). In addition, Uijl (1983) concludes that longer transfer lengths in pretensioned systems result in smaller bursting and spalling stresses. Shorter transfer lengths concentrate the transfer of forces, which result in larger bursting and spalling stresses, more similar to the case of post-tensioned systems. Many theories developed from post-tensioned experiments can provide conservative estimates of the spalling and bursting stresses in pre-tensioned members, because they simulate the case of a very short transfer length (French et al., 2011).

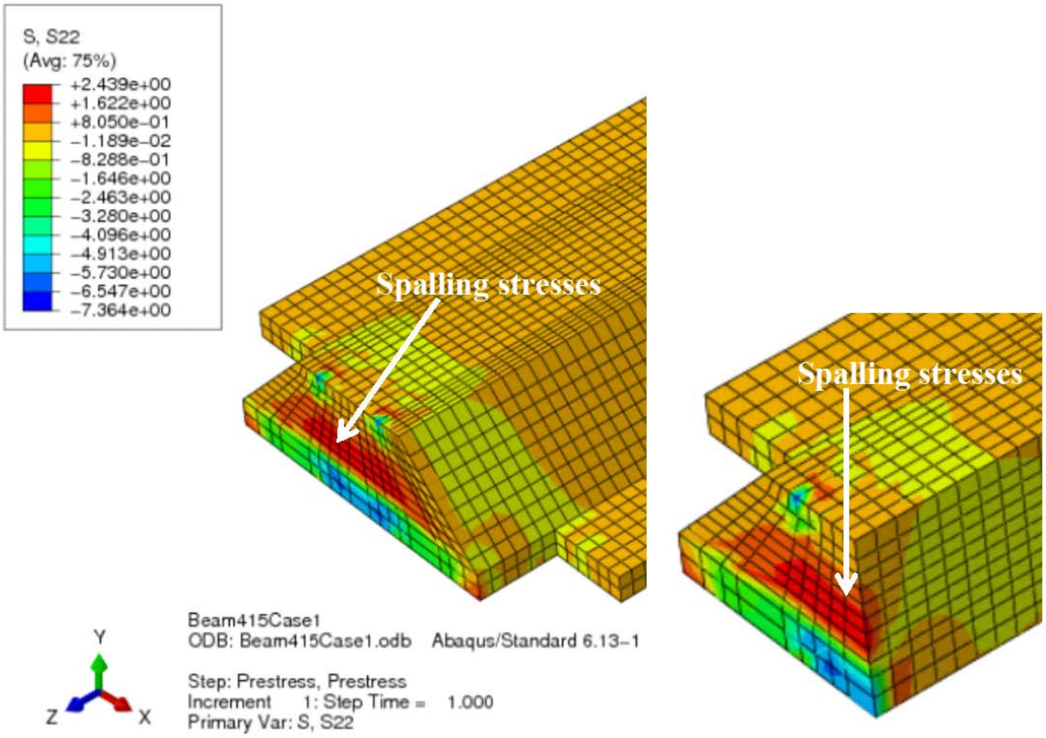

(a) (b)

Figure 34. Normal Stress Contours Along the Depth of the Precast Beam – Case 1 (a) Full Beam, (b) Longitudinal Cut (units – ksi)

Vertical Plane - Case 2

Figure 35(a) shows the normal stress contours along the depth of the precast beam for Case 2. Figure 35(b) shows a longitudinal cut highlighting how the magnitude of the vertical tensile stresses diminishes away from the end of the precast beam highlighting once again that spalling stresses are the dominant type of tensile stress in the end zones. The maximum spalling stress in this case is approximately 2.0 ksi, which is lower compared to the previous case but still unrealistic because no cracking was observed during the visual inspection of the 37 precast beams.

Vertical Plane - Case 3

This modeling technique is more realistic compared to the previous two techniques. The computed maximum vertical tensile stress between the top and bottom layers of strands is approximately equal to 0.40 ksi. This is smaller than the modulus of rupture (0.51 ksi) for the precast beam when the strands were de-tensioned and corroborates the fact that no cracks were observed during the visual inspection of the 37 precast beams.

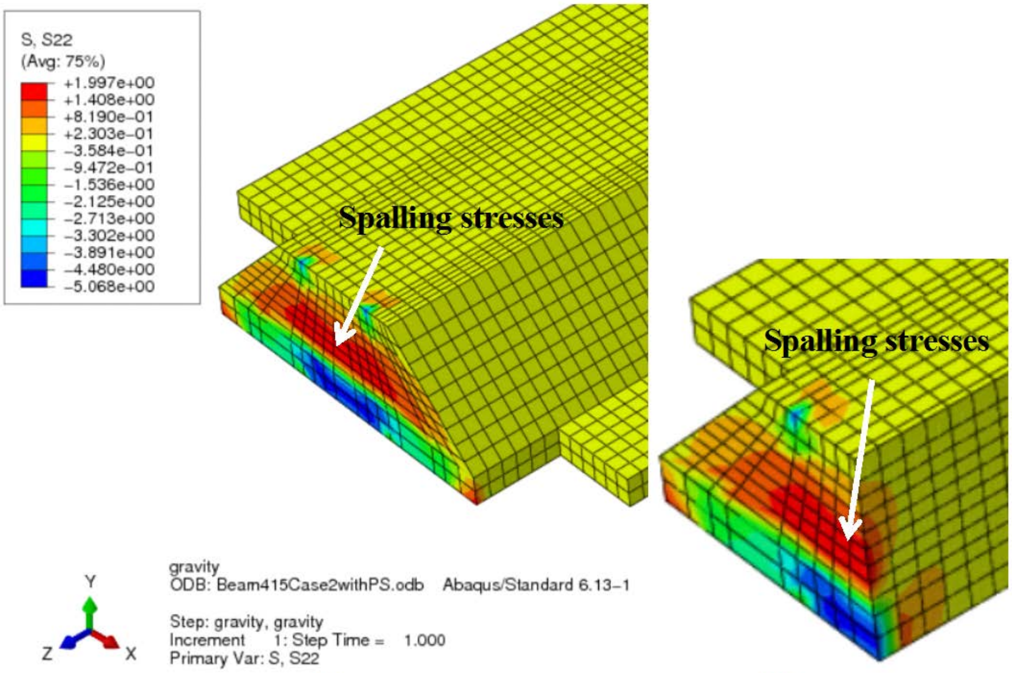

(a) (b)

Figure 35. Normal Stress Contours Along the Depth of the Precast Beam – Case 2, (a) Full Beam, (b) Longitudinal Cut (units – ksi)

Figure 36(a) and (b) show the vertical normal stress contours at the ends of the precast beam and a longitudinal cut at mid-width of the beam. The predominance of spalling stresses in precast beams in which the prestressing force is applied eccentrically toward the bottom of the beam, occurs because there is a greater concrete area above the prestressing force through which the stresses distribute. This requires that the prestressing force spreads over a larger vertical distance, creating a larger spalling force near the end region (Figure 36(b)) (French et. al., 2011). Hawkins (1960) and Gergely et al. (1963) corroborate this phenomenon and report that as eccentricity increases so does the magnitude of the maximum tensile stress in the spalling zone.

There are two isolated locations at the bottom corners of the precast beam where the tensile stress is around 0.90 ksi, however this higher concentration of stress is isolated only at the corner node of the corresponding element and diminishes quickly. These isolated higher concentrations of tensile stress at the bottom corners of the precast beam are believed to be a result of stress concentrations at these corners. Because the visual inspection of the 37 precast beams did not show any signs of cracking at these areas, these isolated stress concentrations are not believed to be detrimental to the structural integrity of the precast beam and its performance. In addition, the provision of AASHTO required confinement steel should help control the width of any potential cracks at these locations.

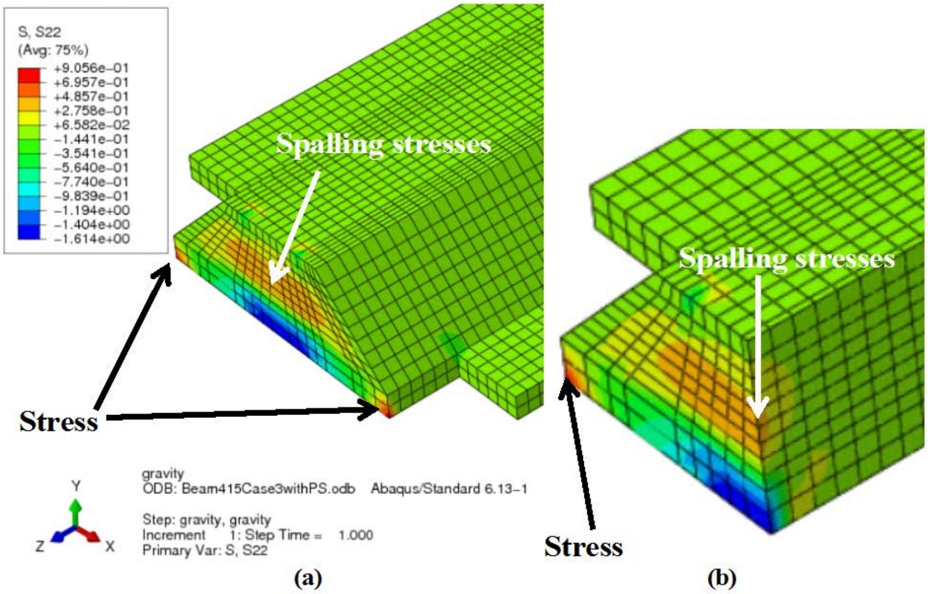

Figure 36. Normal Stress Contours Along the Depth of the Precast Beam – Case 3, (a) Full Beam, (b) Longitudinal Cut (units ksi)

Vertical Plane - Case 4

Figure 37 shows the normal stress contours along the depth of the precast beam. With the flange cut eliminated the stress concentration at the bottom of the intersection between the precast flange and the precast web still exists. The magnitude of vertical tensile tresses at this location is approximately 1.34 ksi, which is higher compared to Case 3. As a result, cutting the precast flanges at the end zones reduces the vulnerability of cracking at the intersection between the precast flange and the precast web.

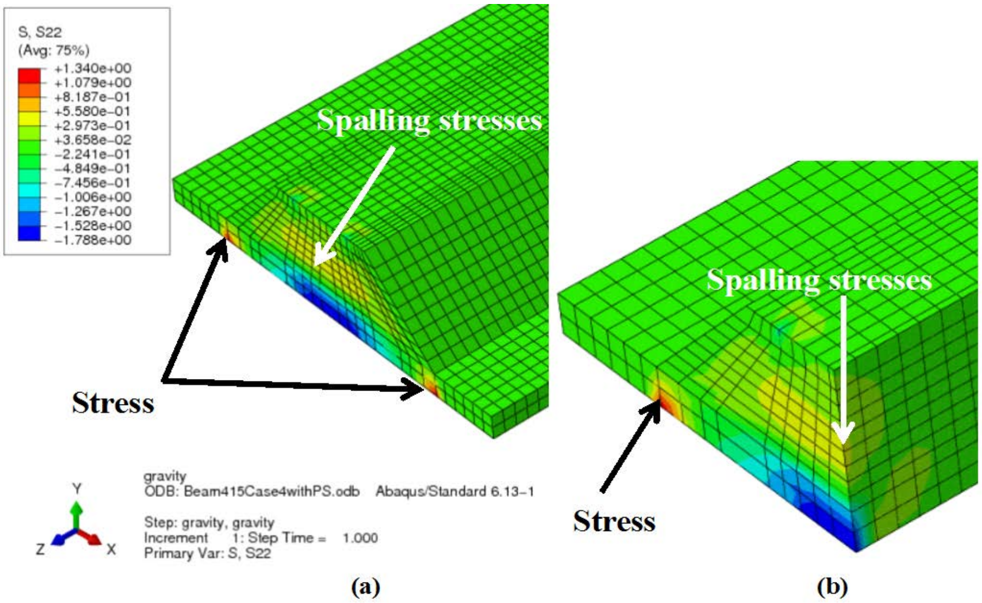

Figure 37. Normal Stress Contours Along the Depth of the Precast Beam – Case 4, (a) Full Beam, (b) Longitudinal Cut

Horizontal Plane

The maximum normal tensile stress in the horizontal plane toward the bottom of the precast beam was only approximately 0.20 ksi, which is lower than the modulus of rupture at transfer (0.51 ksi). As a result, tensile stresses created because of the diffusion of the prestressing force in the horizontal plane were lower than the ones created in the vertical plane. Figure 38 shows horizontal normal stress contours toward the bottom of the precast beam. It can be seen that the distribution of these normal tensile stresses is fairly uniform past 12 to18 in from the end of the beam. Because the prestressing force at the bottom two layers was symmetric about the vertical axis, there was no eccentricity in the horizontal plane. Accordingly, tensile stresses created because of the diffusion of the prestressing force in the horizontal plane were predominantly bursting stresses.

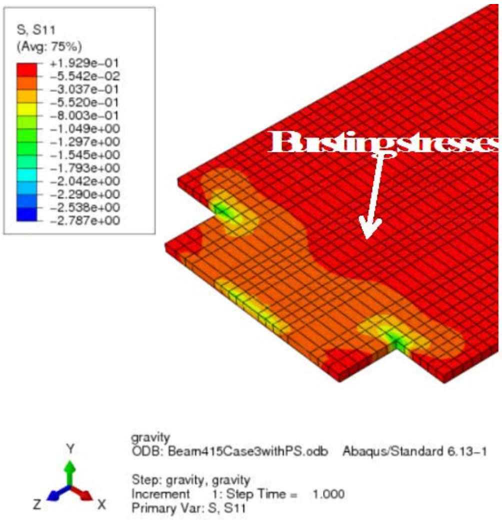

Figure 38. Normal Stress Contours in the Horizontal Plane (units ksi)

Other Cases Investigated

20-ft Span

The magnitude of the vertical normal tensile stresses at the end zones was negligible with the exception of two isolated locations at the bottom corners of the precast web where the tensile stress was 1.30 ksi (Figure 39). However, as discussed previously for the precast beams used in the U.S. 360 Bridge, these higher tensile stresses isolated only at the bottom corners of the precast web are not considered detrimental to the structural integrity and serviceability of the precast beam. In the horizontal plane, the maximum tensile stress was equal to approximately 0.21 ksi, which is still lower than the modulus of rupture of the precast beam at transfer (0.51 ksi). The creation of bursting stresses in the horizontal plane in the case of precast inverted T-beams with tapered webs is due to the diffusion of the prestressing force toward the flanges of the precast beam. This confirms the approach presented in AASHTO LRFD Specifications, which suggests that for pretensioned solid or voided slabs, end zone reinforcing should be placed in the horizontal plane. However, for rectangular solid or voided slabs, in which the strand layout is uniform along the width of the section, the diffusion of the prestressing force in the

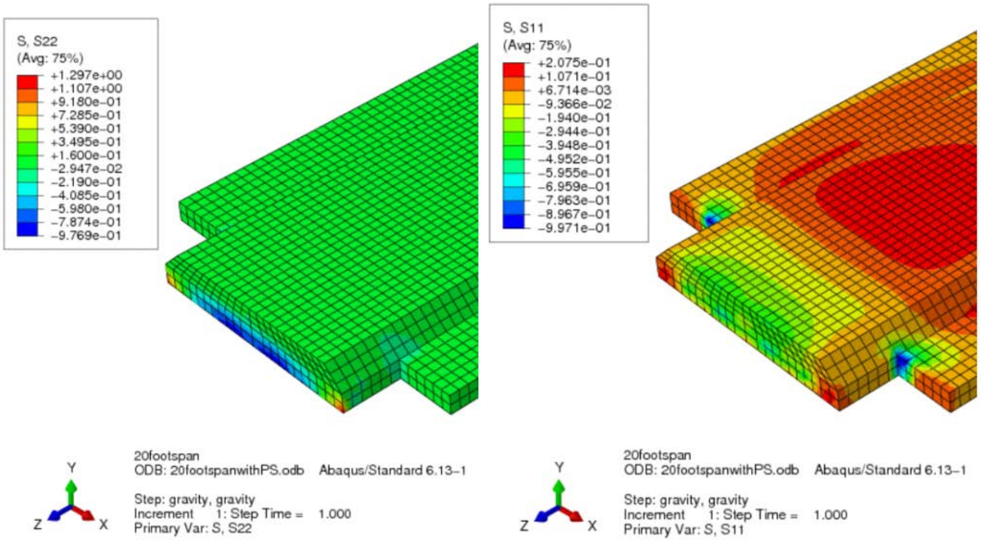

(a) **(b)**

Figure 39. Normal Stress Contours (a) Vertical Plane (b) Horizontal Plane for 20-ft Beam (units- ksi)

horizontal plane will not be applicable. The negligible magnitude of spalling stresses in the vertical plane also confirms the findings from previous research that the magnitude of spalling stresses is directly proportional to the eccentricity of the prestressing force.

60-ft Span

In this case, the magnitude of spalling stresses near the end of the beam exceeded the modulus of rupture of the precast beam at transfer (0.51 ksi) (Figure 40). The maximum tensile stress in the vertical direction was 0.83 ksi. Consequently, spalling stresses at the end zones of precast beams used for similar spans present a potential for cracking at the end zones. The magnitude of bursting stresses in the horizontal plane was lower than the modulus of rupture of the precast beam at transfer with the maximum tensile stress equal to 0.27 ksi. Accordingly, bursting stresses in the horizontal plane did not present a potential for cracking in the end zones.

Evaluation of AASHTO LFRD Specifications Method

Because the shape of the precast inverted T-beams with tapered webs is unique, engineering judgment should be used in implementing the AASHTO provisions (2013) for the pretensioned anchorage zones. The following questions need to be addressed:

1. Should the end zone reinforcing be provided in the vertical plane, horizontal plane or both?

2. Where should the end zone reinforcing be located?

AASHTO LRFD Specifications require end zone reinforcing in pretensioned anchorage zones, regardless of the span length, strand pattern, geometry of the precast member, eccentricity or magnitude of the prestressing force. Following is a comparison of end zone reinforcement designed based on the present AASHTO provisions, the finite element model results previously

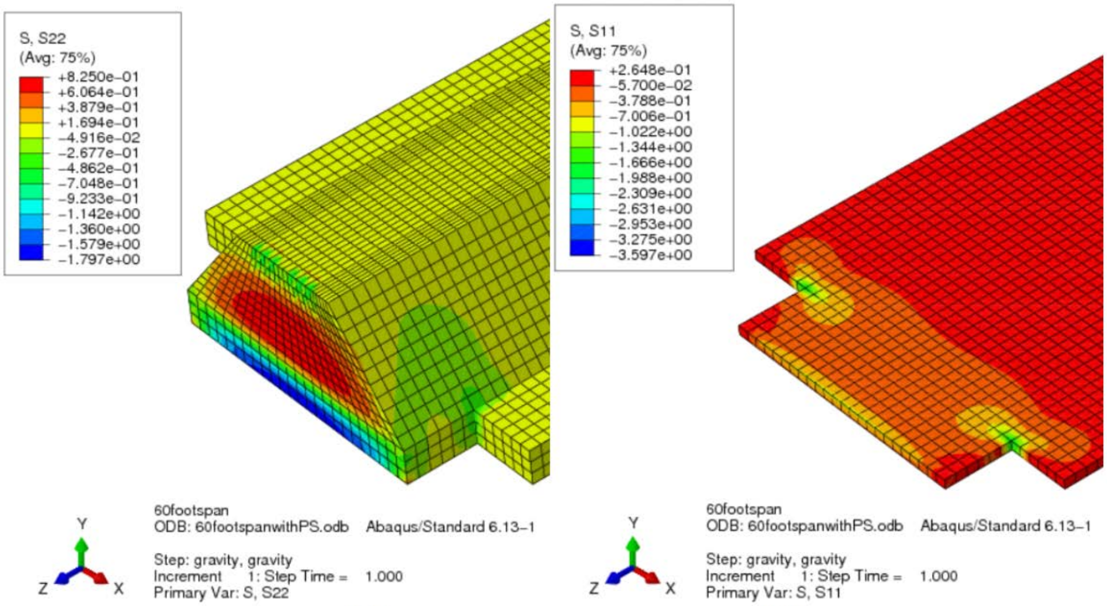

(a) (b)

Figure 40. Normal Stress Contours (a) Vertical Plane (b) Horizontal Plane for 60-ft Beam (units ksi)

discussed, and the recommendations of a recently completed NCHRP project (French et al., 2011). The three span lengths previously discussed are evaluated.

20-ft Span

Spalling and bursting stresses for the 20 ft span were lower than the modulus of rupture of the precast beam at transfer. Accordingly, end zone reinforcing is not required and the implementation of AASHTO provisions for pretensioned anchorage zones in the vertical and horizontal planes would be conservative. The total prestressing force for the 8 in deep precast beam is 434 kips. 4% of this force equals 17.36 kips. If an allowable steel stress of 20 ksi is used, then the required area of the steel in the end zones is 0.87 in^2. The vertical steel can be provided in one row of No.4 confinement steel and four legs of No.4 extended stirrups. The horizontal steel can be provided by the horizontal leg of the No.4 confinement reinforcing at 6 in on center (Figure 41(a)).

41.5-ft Span

The total prestressing force for the 18 in deep precast beam used in the 41.5 ft span U.S. 360 bridge is 1144 kips. Four percent of this force equals 45.76 kips. If an allowable steel stress of 20 ksi is used, then the required area of vertical steel in the end zones is 2.29 in^2. In addition, according to AASHTO provisions, this amount of steel is distributed over a distance of *h/4* from the end of the member. The area of vertical end zone reinforcing provided in the first row in the precast beams used in the U.S. 360 Bridge is 1.08 in^2 (four legs of No.4 extended stirrups and the vertical component of the two inclined legs of the No.4 confinement stirrups [Figure 12]). In addition, the first row of vertical steel is located at 2 in from the end of the precast beam. The second row of vertical steel provides the same area of steel and is located at 5 in from the end of the beam, which is past the prescribed *h/4* distance. The total area of vertical steel provided in

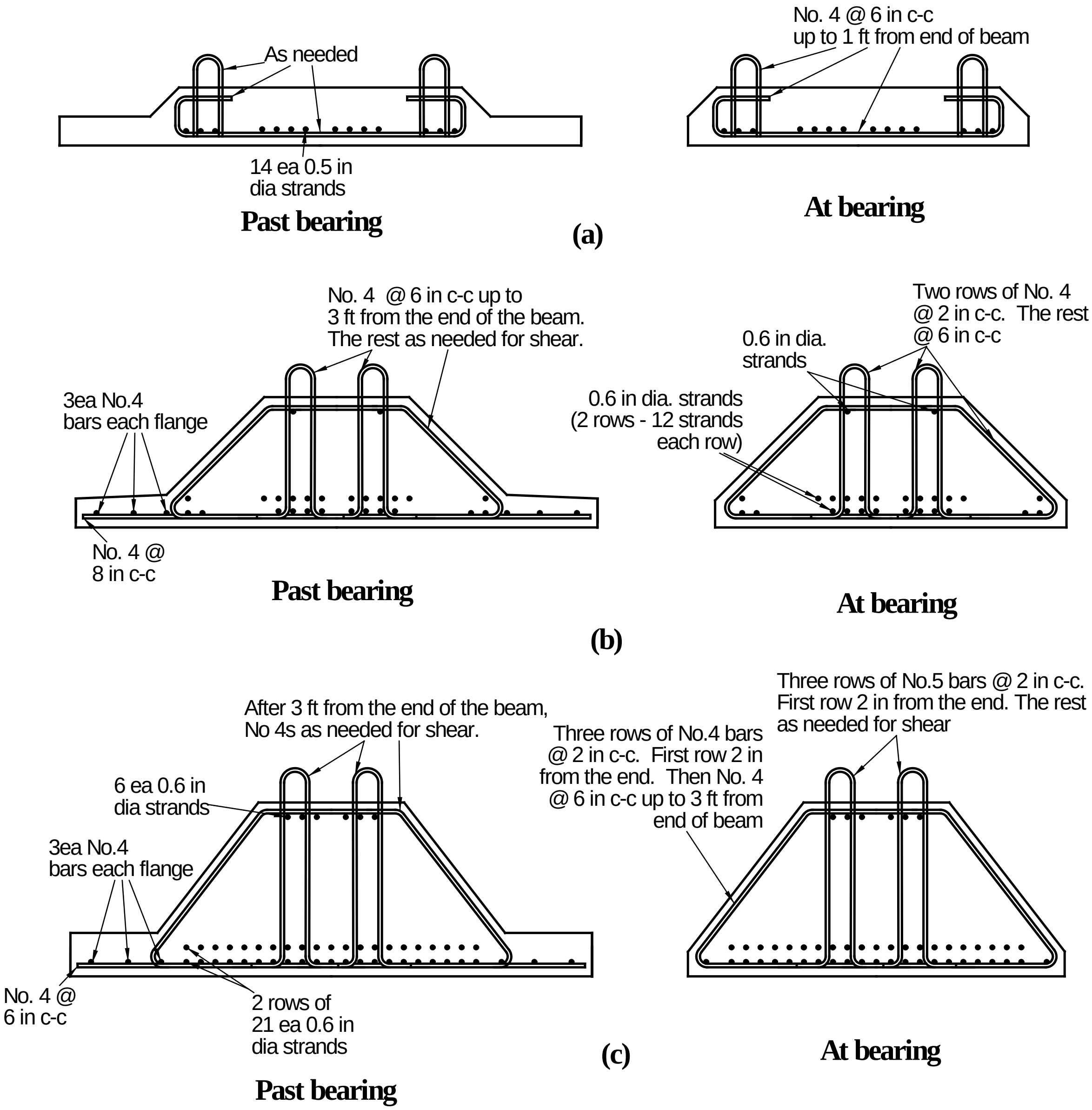

Figure 41. Summary of End Zone Reinforcing Details Calculated Based on Current AASHTO Provisions, (a) 20-ft Span, (b) 41.5-ft Span, (c) 60-ft Span. Note: ea = each, c-c = center-to-center, dia = diameter, @ = spaced at

the first two rows is 2.16 in^2, which is smaller than the AASHTO required 2.29 in^2. However, because the results of finite element analyses indicated that spalling stresses in the vertical plane were smaller than the modulus of rupture of the precast beam at transfer, using a slightly smaller area was deemed acceptable. In addition, to comply with the AASHTO placement requirement the position of the second row can be changed to 4 in from the end of the member rather than 5 in (Figure 41(b)).

Bursting stresses in the horizontal plane were approximately half of the spalling stresses in the vertical plane (0.20 ksi versus 0.40 ksi). Accordingly, it would be conservative to apply the 4% rule for sizing reinforcing in the horizontal plane. In addition, because the distribution of bursting stresses was relatively uniform within the disturbed region *h*, horizontal reinforcing can be distributed throughout a distance *h* from the end of the precast flange rather than *h/4.* For the U.S. 360 Bridge, the 2.29 in^2 of horizontal reinforcing determined using the 4% rule could be distributed over a distance of 6 ft past the precast flange. This leads to approximately 0.38 in^2/ft. The closed stirrups in the U.S. 360 Bridge consisted of No.4 at 6 in on center, for up to 1.5*d* from the end of the precast member (confinement steel) and No.4 at 12 in on center for the rest of the span. In addition, No.4 at 8 in on center transverse straight reinforcing steel was provided in the precast flanges. Accordingly, as a minimum, the provided amount of horizontal steel at the end zones was equal to 0.5 in^2/ft (Figure 41(b)).

In summary, it is conservative to size the vertical and horizontal steel at the end zones based on the 4% rule stipulated in AASHTO. The distribution of this reinforcing should be such that the vertical steel is located within a distance equal to *h/4*, where *h* is the depth of the member, and the horizontal steel is located within a distance equal to *h* from the end of the precast flange, where *h* is the width of the section.

60-ft Span

Because spalling stresses exceeded the modulus of rupture for the precast beam at transfer, vertical reinforcing at the end zones is required to control the widths of potential cracks. The vertical tensile force at the end zone can be calculated from the tension stress in the finite elements in the end zone. The tension stress above the modulus of rupture multiplied by the area of the elements is equal to 28.5 kips, whereas the force based on the 4 % rule is equal to 78.72 kips. Therefore, the amount of vertical steel can be conservatively calculated based on AASHTO provisions. The required area of vertical reinforcing in the end zones based on AASHTO provisions in this case is 3.94 in^2. This area of reinforcing can be provided by placing three rows of No.4 confinement steel and four legs of No.5 extended stirrups at 2 in on center. The total area of provided vertical steel in this case will be 4.57 in^2 compared to the required 3.94 in^2 (Figure 41(c)).

Because the magnitude of the bursting stresses in the horizontal plane did not exceed the modulus of rupture for the precast beam at transfer, reinforcing steel in the horizontal plane in the end zones is not required. Accordingly, the AASHTO provisions for pretensioned anchorage zones in the horizontal plane would yield a conservative design. The required area of horizontal reinforcing based on the 4% rule (3.94 in^2) can be partially provided by three rows of No.4 confinement reinforcing at 2 in on center and the rest of the confinement steel at 6 in on center. This steel area combined with No.4 transverse straight bars at 6 in on center yields a total area of bottom transverse steel of approximately 4.8 in^2, which is larger than the required 3.94 in^2 (Figure 41(c)).

Evaluation of the NCHRP Web-Only Document 173 Method

French et al. (2011) provide recommended equations for sizing end zone reinforcing in the vertical plane. The method presented by French et al. (2011) will be referred to herein as the NCHRP method. The equations for this method were presented previously in this report as Equations 19 through 23. Table 9 provides the input parameters required to calculate the

Table 9. Recommendations From NCHRP Web-Only Document 173*

	Span Length		
Parameter	**20 ft**	**41.5 ft**	**60 ft^**
h, in	8	18	24
P_i ,kips	417	1078	1968
A, in^2	460	757	1044
e, in	1.47	2.99	3.94
d_b, in	0.5	0.6	0.6
f_{ci} , ksi	5	5	5
f_s, ksi	20	20	20
σ_s ,ksi	0.036	0.106	NA
f_r , ksi	0.51	0.51	0.51
P_r , kips	NA	NA	78.72
A_s, in^2	Not Required	Not required	3.94

*French et al., 2011.
^Same as AASHTO.

required reinforcing based on the recommendations of NCHRP method for the three bridge spans and the associated results.

20-ft Span

For the 20-ft span, the NCHRP approach predicts negligible spalling stresses at the end face (0.036 ksi). The results from the NCHRP equations are in close agreement with the results from finite element analyses for the 8 in deep precast beam, which exhibited negligible spalling stresses. In addition, the conclusion that no vertical reinforcing is required is supported by the results from finite element analyses.

41.5-ft Span

The magnitude of spalling stresses predicted by the NCHRP method for the 41.5-ft span is equal to 0.106 ksi. This is lower than the magnitude of spalling stresses computed from the finite element models, which is 0.40 ksi. The NCHRP method yields a smaller spalling stress for this case, however, the conclusion that no vertical end zone reinforcing is needed is consistent with the one based on finite element analyses.

60-ft Span

For the 60-foot span, NCHRP recommendations are identical to the AASHTO provisions for pre-tensioned anchorage zones because the depth of the precast member for this span was 24 in.

Evaluation of Alternative Approach Using Strut-and-Tie Modeling

An alternative approach for pretensioned anchorage zone design is to use strut-and-tie modeling to determine spalling forces in the vertical plane and bursting forces in the horizontal plane. Several strut-and-tie models were investigated in the vertical and horizontal planes with the purpose of identifying the models that most closely replicated the results obtained from finite element analyses. One property of strut-and-tie models is that they ignore the contribution of concrete in tension and if chosen properly usually lead to conservative designs. Only the 41.5-ft span girder will be evaluated using strut-and-tie modeling.

Vertical Plane

Figure 42 shows the distribution of longitudinal normal stresses caused by the prestressing force at a distance *h* from the end of the precast member for the precast beams used in the U.S. 360 Bridge. The majority of the prestressing force was concentrated at the bottom two rows and consisted of 24 0.6 in diameter strands, each stressed to approximately 44 kips. This resulted in a prestressing force of 1055 kips 3 in above the bottom of the beam. The remaining two strands were located 2 in from the top of the precast beam. These two strands created a prestressing force of 88 kips. Figure 43 shows the distribution of the prestressing force in the vertical plane and the orientation of principal stress vectors. The maximum principal tensile stresses in the vertical plane are located at the end face of the precast beam.

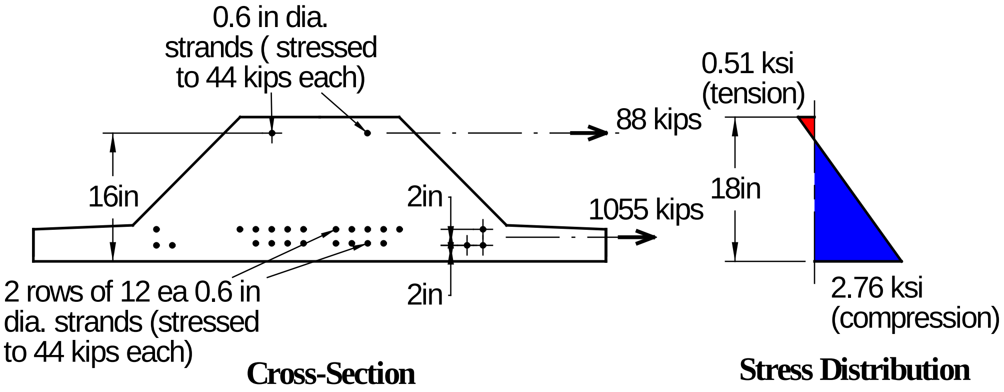

Figure 42. Distribution of Longitudinal Normal Stresses at the Ends of the Precast Beam. Note: dia. = diameter, ea = each

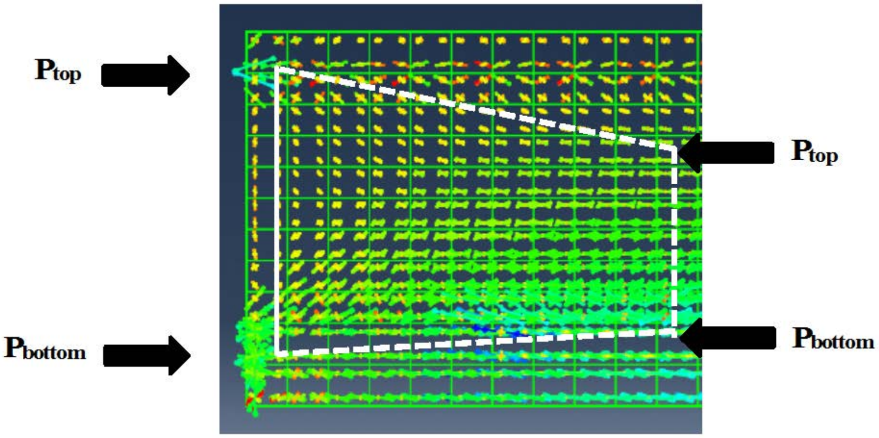

Figure 43. Principal Stress Vectors for 41.5-ft Span, Case 3 – Vertical Plane

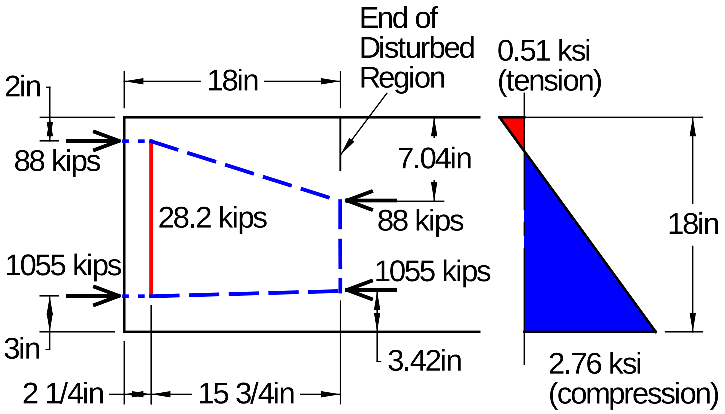

Figure 44. Strut-and-Tie Model for the Vertical Plane

Figure 43 also shows the same strut-and-tie model that was used in Figure 44 to estimate the magnitude of the spalling stresses at the end face of the precast beam. The longitudinal stress diagram at a distance *h* from the end of the beam was integrated to produce top and bottom horizontal forces that matched the magnitude of those applied at the end of the beam. Furthermore, this model includes only one tension tie, which closely matches the location of the spalling stresses at the end face of the precast beam.

The disadvantage of this model is that all the vertical steel intended to resist spalling stresses must be placed within 4.5 in (*h/4*) from the end of the beam. The tension force in the tie was 28.2 kips (as opposed to 45.7 kips determined using the 4% rule of AASHTO Provisions). If a 20 ksi allowable stress is used to determine the area of vertical steel then the required area is 1.41 in^2. The total vertical area of steel in the first row, used in the precast beams for the U.S. 360 Bridge, was 1.08 in^2, which is approximately 77% of the required steel area based on this strut-and-tie model. The second row of extended stirrups and confinement steel is the same as the first row, but is located 5 in from the end of the member, which is past the prescribed distance of *h/4* (4.5 in). However, because the results of finite element analyses for the 41.5ft span revealed that spalling stresses at the end of the beam were smaller than the modulus of rupture of concrete at transfer, such a distribution of steel at the end zones was deemed acceptable. In addition, the visual inspection of all fabricated precast beams confirmed that no cracking was observed at the end zones. Compared to the 4% AASHTO rule, the strut-and-tie model leads to designs that are more economical and less congested in the end zones. However, experimental testing is required to validate the suitability of this model for sizing vertical reinforcing in the end zones, especially for cases when spalling stresses exceed the modulus of rupture of concrete at transfer.

Horizontal Plane

Figure 45 illustrates the diffusion of the prestressing force introduced in the bottom two strand layers in the horizontal plane using principal stress vectors. Because the prestressing force at the bottom two strand layers was introduced within the footprint of the precast web, it will tend to distribute outwards toward the flanges as it is being transferred to the surrounding concrete. Also shown in this figure is one of the strut-and-tie models used to determine the magnitude of bursting stresses within the disturbed region.

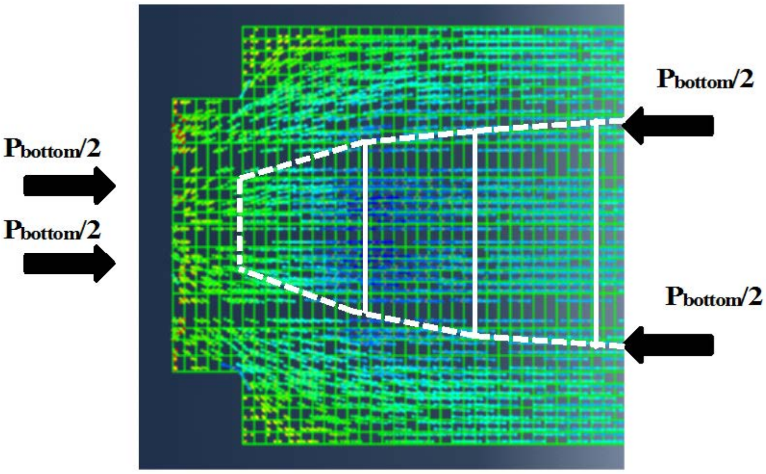

Figure 45. Principal Stress Vectors for 41.5-ft Span, Case 3 – Horizontal Plane

Three strut-and-tie models were investigated (Figure 46(a)-(c)). Model H1 is the simplest of the three and contains only one tension tie. The tension force in the tie is 92 kips, which is approximately 8.7 % of the total prestressing force in the bottom two strand layers. Model H2 contains two tension ties. The sum of tension forces in the ties of this model is 59 kips, which is 5.6% of the total prestressing force in the bottom two strand layers. Model H3 contains three tension ties throughout the disturbed region. The sum of tension forces in the ties is 83 kips, which is 7.87 % of the total prestressing force in the bottom two strand layers. Regardless of the model selected, the horizontal reinforcing can be distributed uniformly throughout the disturbed region.

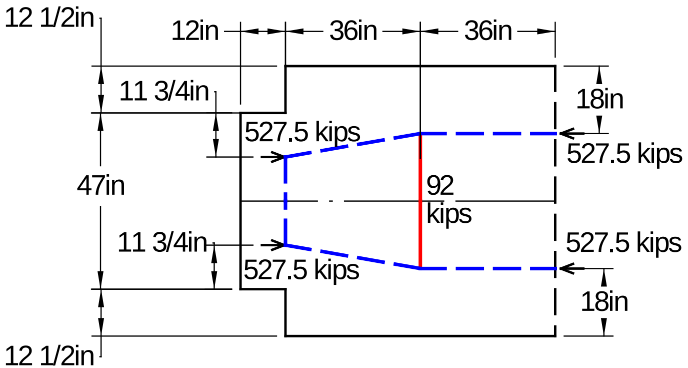

(a) Model H1

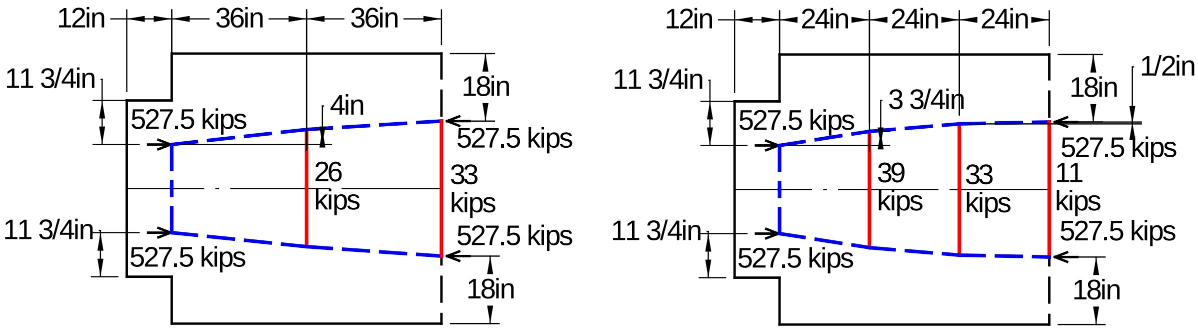

(b) Model H2

(c) Model H3

Figure 46. Strut-and-Tie Models for the Horizontal Plane

For a simple approximation of the bursting force for the horizontal direction, the approach for bursting forces in post-tensioned members in section 5.10.9.3 of the AASTHTO LRFD Specifications is more appropriate than the 4% rule. A simplified version of the equation presented is:

$$T_{burst} = \frac{P}{4}\left(1 - \frac{a}{h}\right) \quad \text{Eq. 27}$$

where

P = force applied by prestressing, kips
a = width of the bearing plate, in
h = height of member, in

In the case of the inverted T-beam, since there is no plate, the dimension "*a*" can be considered as the width of the member over which the prestressing force is applied, which is 47 in. The dimension "*h*" is the full width of the beam, 72 in. Using these dimensions with the full prestressing force of 1055 kips, results in a bursting force of 92 kips. This matches exactly the strut-and-tie model bursting force in Model H1 in Figure 46. The specifications require that the reinforcement for the required bursting force be distributed over the distance *h* from the loaded face.

Summary of Investigation of End Zone Stresses

Table 10 provides a summary of end zone reinforcing determined using the various methods described in this paper. The results of finite element analyses suggest that no end zone reinforcing is required for 20 ft or 41.5 ft span cases, but is required for the 60 ft span. As stated earlier, AASHTO LRFD Specifications require end zone reinforcing in pretensioned anchorage zones, regardless of the span length, strand pattern, geometry of the precast member, eccentricity or magnitude of the prestressing force. Table 10 provides the end zone reinforcing for the vertical and horizontal planes based on AASHTO. The results of the NCHRP method are consistent with the results of finite element analyses. For the 24 in deep precast beam used in the 60 ft span the NCHRP method predicts a higher amount of vertical reinforcing and can therefore be used conservatively in design. Only the 18 in deep precast beam used in the U.S. 360 Bridge (41.5 ft span) was evaluated using the strut-and-tie method. Compared to the 4% AASHTO rule, strut-and-tie model V1 leads to designs that are more economical and create less congestion in the end zones. However, experimental testing is required to validate the suitability of this model for sizing vertical reinforcing in the end zones, especially for cases when spalling stresses exceed the modulus of rupture of concrete at transfer. In the horizontal plane, strut-and-tie model H3 presents an even more conservative approach compared to the 4% AASHTO rule. If this model is selected, then the horizontal reinforcing can be distributed uniformly throughout the disturbed region.

Table 10. Area of End Zone Reinforcing Determined Using Various Methods, in^2

Design Method	20-ft span		41.5-ft span		60-ft span	
	Vertical	Horizontal	Vertical	Horizontal	Vertical	Horizontal
FEA*	Not required	Not required	Not required	Not required	1.43	Not required
AASHTO	0.87	0.87	2.29	2.29	3.94	3.94
NCHRP	Not required	Not addressed	Not required	Not addressed	3.94	Not addressed
Strut-and-Tie	Not evaluated	Not evaluated	1.41	4.15	Not evaluated	Not evaluated

*FEA = Finite Element Analysis.

Live Load Testing

The longitudinal strains recorded during the live load test and those computed from the two finite element models are shown in Figure 47 through Figure 50. During the live load test for truck position 1, BDI gages 14, 15, and 16 did not provide stable recordings. Accordingly, the data from these three gages were considered unreliable. At the end of the first test the connection between these gages and the nodes was checked and it was ensured that they were properly working prior to conducting the second test. Figure 47 shows that the response of the bridge measured in terms of longitudinal strains during the first test is bracketed reasonably well by the response obtained from the finite element model without barriers (parapets) and the model with one continuous barrier. The maximum longitudinal strain recorded during the first test was about 16 microstrain, which is almost half of that calculated using the beam line model and the LLDF assuming a cast-in-place slab span system (31 microstrain), which suggests that it would be conservative to design the inverted T-beam system assuming cast-in-place slab span behavior. The position of truck in Test 1 was such that the center of the truck aligned with the mid-width of the bridge. As a result, the computed response of the bridge based on the model without the barrier was symmetric about the mid-width of the bridge. As expected, the presence of the barrier in the model resulted in a computed response that was softer near the edge of the bridge without the barrier and stiffer near the edge with the barrier. Because of a lack of data from BDI gage 14, 15, and 16 such an observation could not be confirmed in the measured response.

The results from Test 2 and Test 3 corroborate some of the observations made in Test 1 (Figures 48 and 49). The measured response of the bridge in terms of longitudinal strains is bracketed reasonably well by the computed response obtained from the two finite element models. The maximum longitudinal strain measured in Test 2 and Test 3 was 16 to 17 microstrain. In both Test 2 and 3 the influence of the barrier in the computed response was more noticeable toward the end of the bridge where the barrier was installed and less noticeable toward the opposite end of the bridge. The measured response of the bridge was closer to the computed response obtained from the model with the continuous barrier.

The measured response of the bridge during Test 4, shown in Figure 50, was slightly stiffer than the computed response from the finite element models but still reasonably close considering the number of uncertainties that affect the actual behavior of the bridge. The highest measured longitudinal strain was about 17 microstrain, which was similar to those measured during the first three tests. The computed maximum longitudinal strains were slightly higher than the first three tests. As expected, these higher longitudinal strains were exhibited in the two exterior beams where the majority of the truck load was applied. In addition, there was not a significant difference between the computed responses with and without the barrier, especially

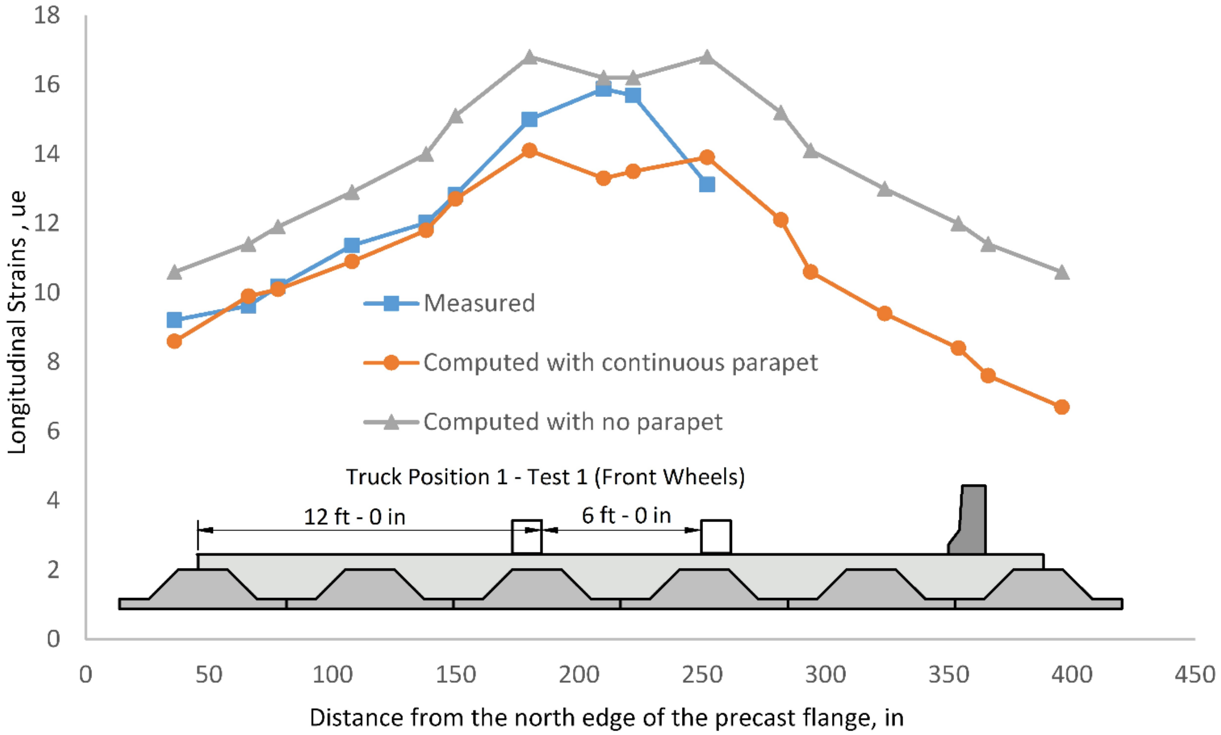

Figure 47. Longitudinal Strains in Each Girder – Truck Position 1

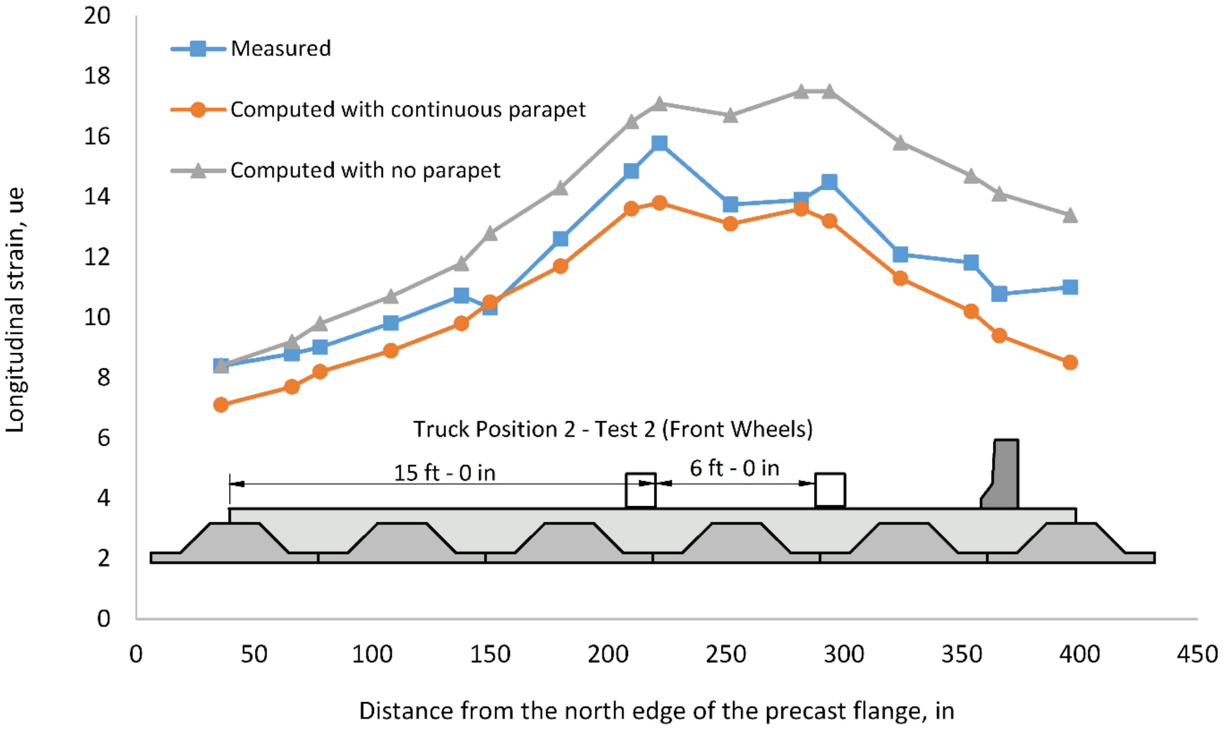

Figure 48. Longitudinal Strains in Each Girder – Truck Position 2

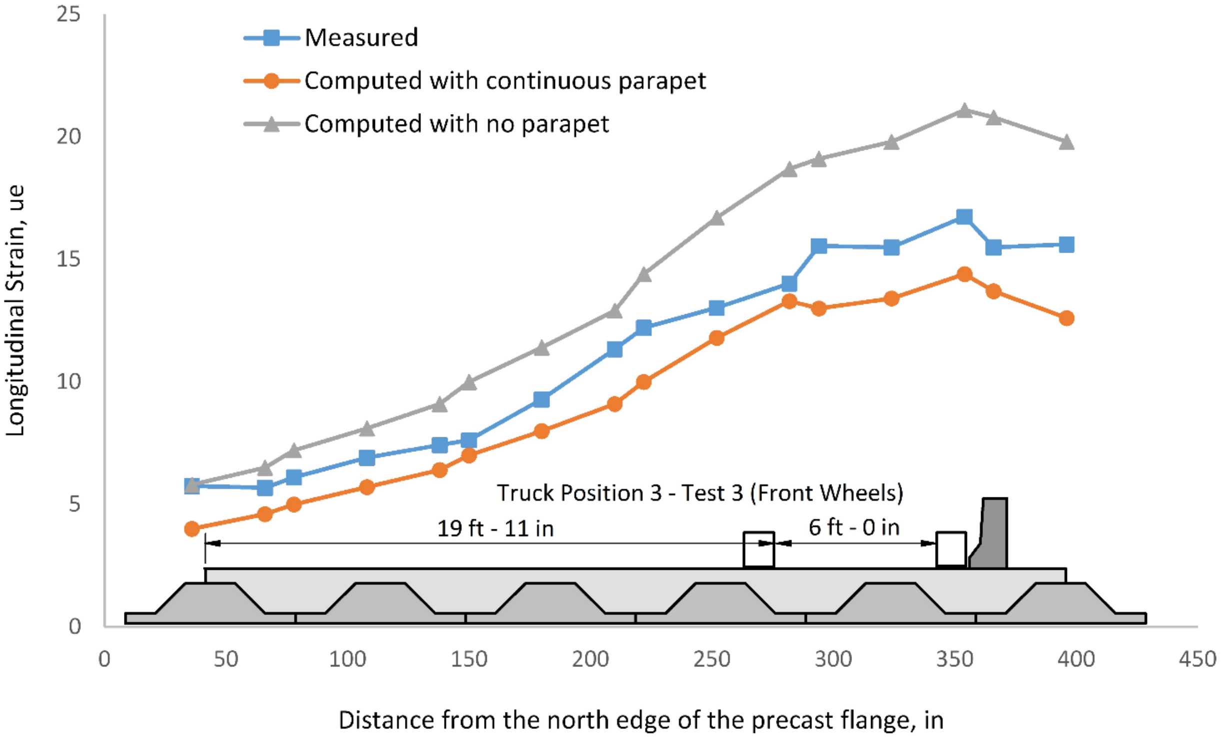

Figure 49. Longitudinal Strains in Each Girder – Truck Position 3

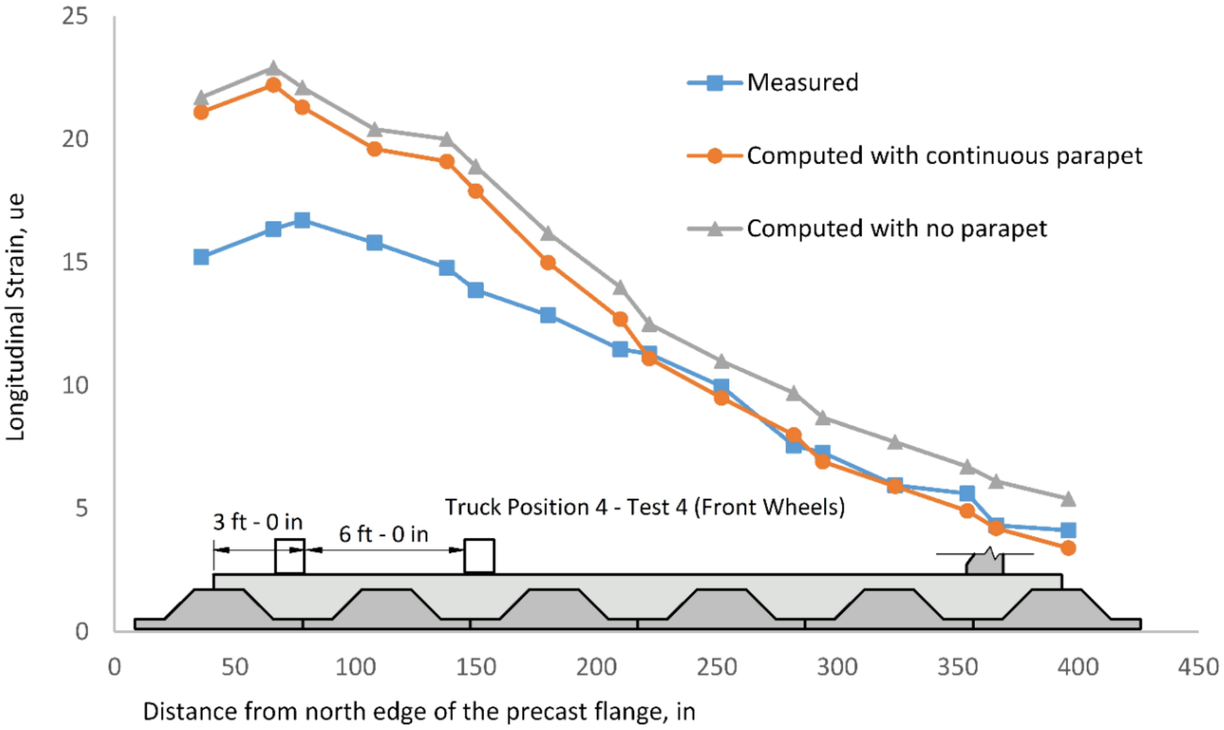

Figure 50. Longitudinal Strains in Each Girder – Truck Position 4

toward the end of the bridge without a barrier. This observation was also expected because the precast beams in the vicinity of the barrier were the farthest from the controlled vehicle and they were not as influential in their load sharing capabilities as were the rest of the precast beams. Therefore, the presence or lack of a barrier did not make a marked difference.

These results suggest that the behavior of the bridge can be simulated reasonably well using a finite element model that is created based on the assumptions stipulated earlier. The measured and computed longitudinal strains at mid-width of the precast beams were used to calculate LLDFs for moment using Equation 28.

$$LLDF_i = \frac{\varepsilon_i E_i S_i(n)}{\sum_{i=1}^{6} \varepsilon_i E_i S_i} \qquad \text{Eq. 28}$$

where

ε_i = longitudinal strain at mid-width of each inverted T-beam
E_i = modulus of elasticity of the precast beam
S_i = section modulus of the composite section for each composite beam
n = number of trucks used to load the bridge
$LLDF_i$ = Live Load Distribution Factor for each inverted T-beam

The LLDFs calculated using this approach were compared with those calculated based on AASHTO's methods. LLDFs based on the measured response could not be calculated for Test 1 because, as stated earlier, the strain data from BDI 14, 15 and 16 were discarded as unreliable. Figures 51 through 54 show that the difference between the measured and computed LLDFs for moment is very slight when the barrier rail is not considered. Note that the values based on measurements were calculated using the section moduli of the beams, not considering the barrier rail. For the FEM analysis in which a continuous barrier was assumed, the LLDFs for the exterior beam with the barrier were higher for truck positions 1, 2, and 3. This is due to the higher stiffness of the exterior beam with the barrier, which causes it to attract more moment. Because the added stiffness of the barrier rail is uncertain due to the connection to the beam, only the LLDFs obtained based on the assumption of no barrier are compared to LLDFs calculated using AASHTO methods.

Table 11 provides a summary of the LLDFs calculated based on the measured and computed behavior. For truck positions 1 and 2, the highest LLDF assuming no barrier rail was 0.22, which is much smaller than the AASHTO values of 0.39 for cast-in-place slab spans and 0.30 for adjacent box beam bridges. For truck positions 3 and 4, the highest LLDFs assuming no barrier rail were 0.26 and 0.27 respectively, which are also lower than AASHTO's factors. As can be seen the design of the inverted T-beam system for moment, for a one lane load case, can be conservatively based assuming a cast-in-place slab span or adjacent box structure behavior.

Because the behavior of the bridge superstructure system when subject to the controlled vehicle was linear elastic, the measured and computed longitudinal strains for truck positions 1+4, 2+4 and 3+4 were combined to account for the multiple presence effect. LLDFs for moment were computed using Equation 28 and are provided in Table 12. In addition, the maximum measured and computed LLDFs for one design lane loaded were multiplied by the multiple presence factor of 1.2 given in AASHTO as an alternative way to account for the

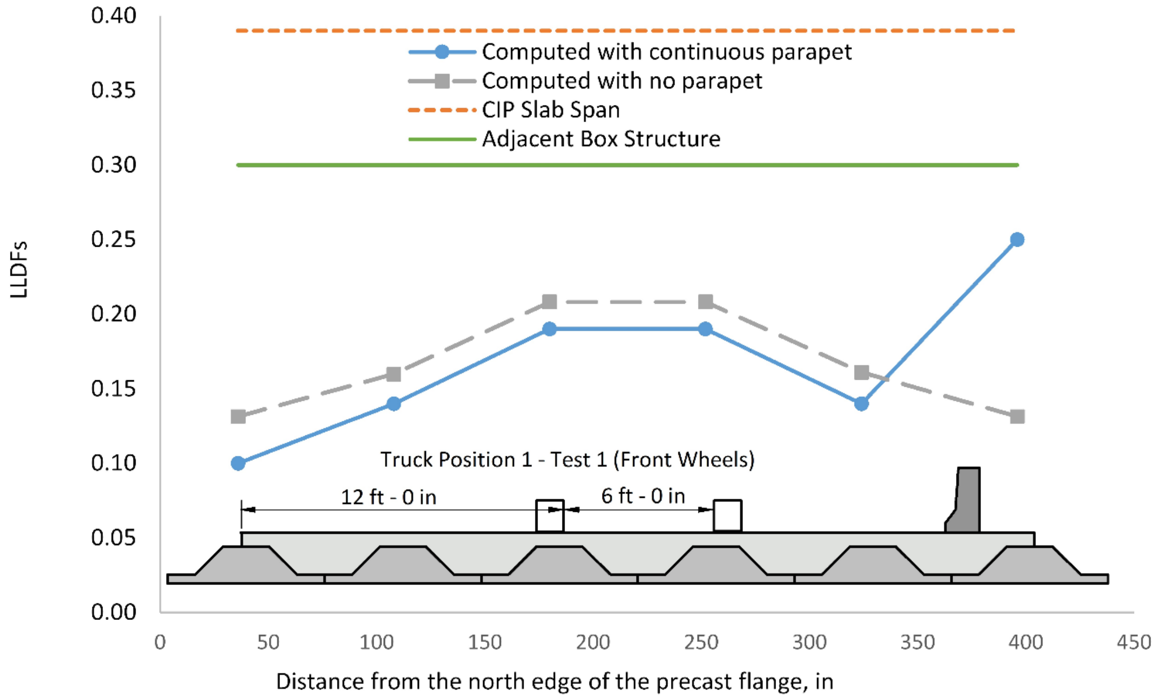

Figure 51. LLDFs in Each Girder – Truck Position 1

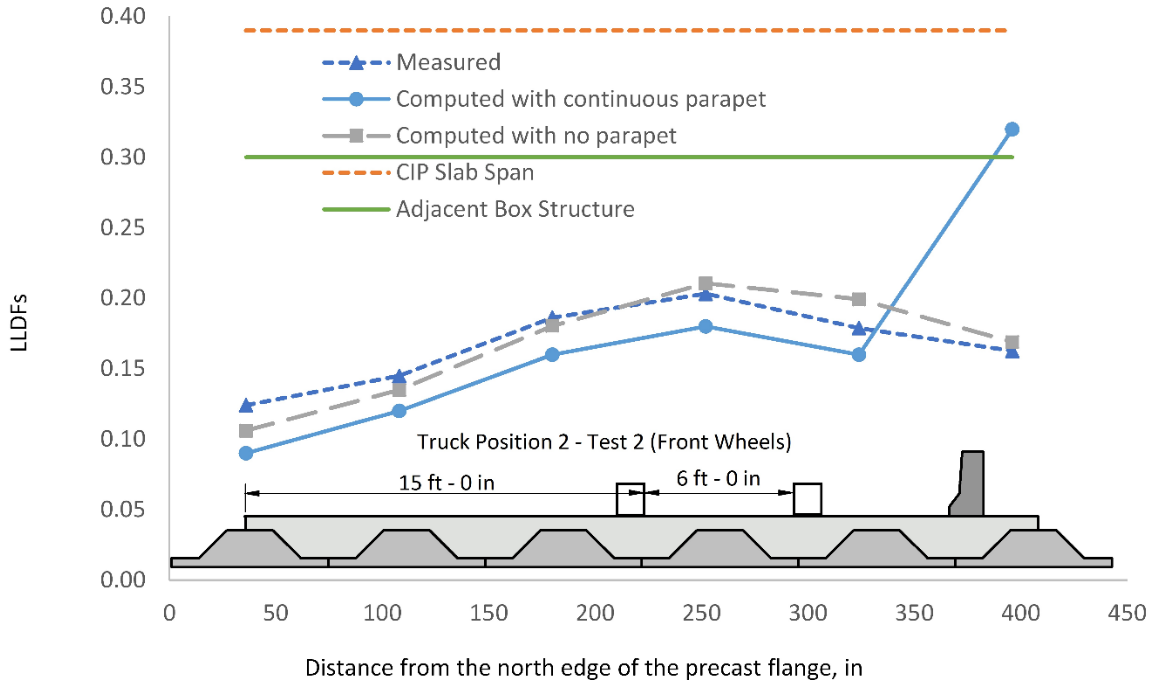

Figure 52. LLDFs in Each Girder – Truck Position 2

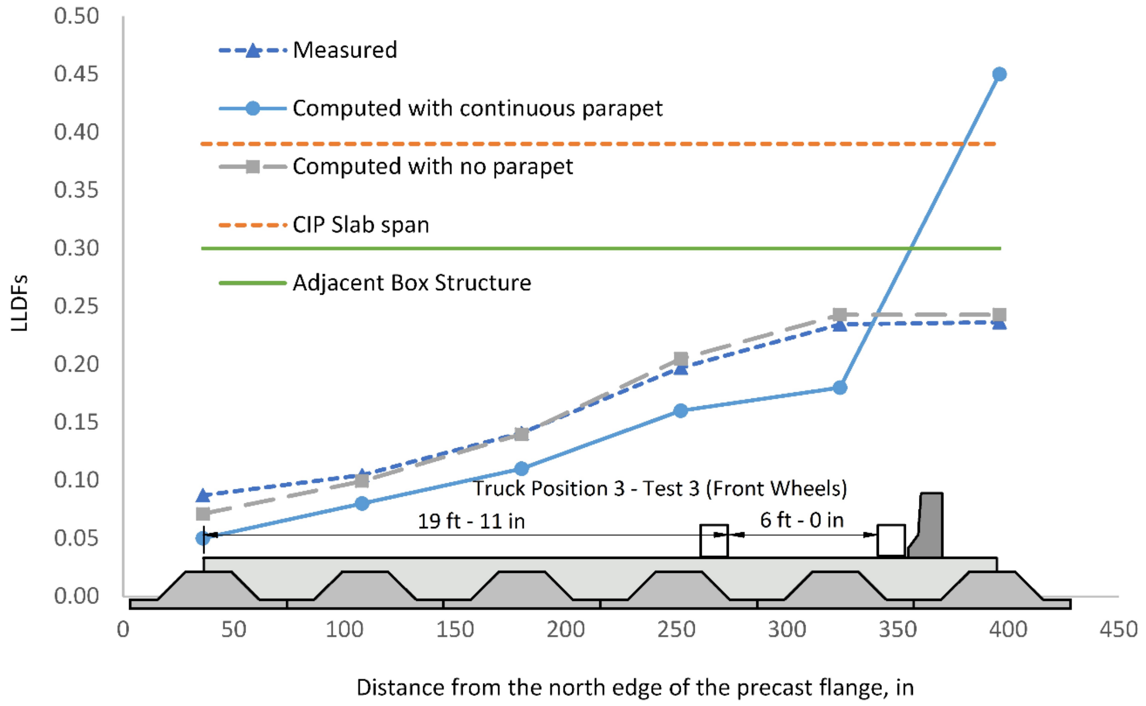

Figure 53. LLDFs in Each Girder – Truck Position 3

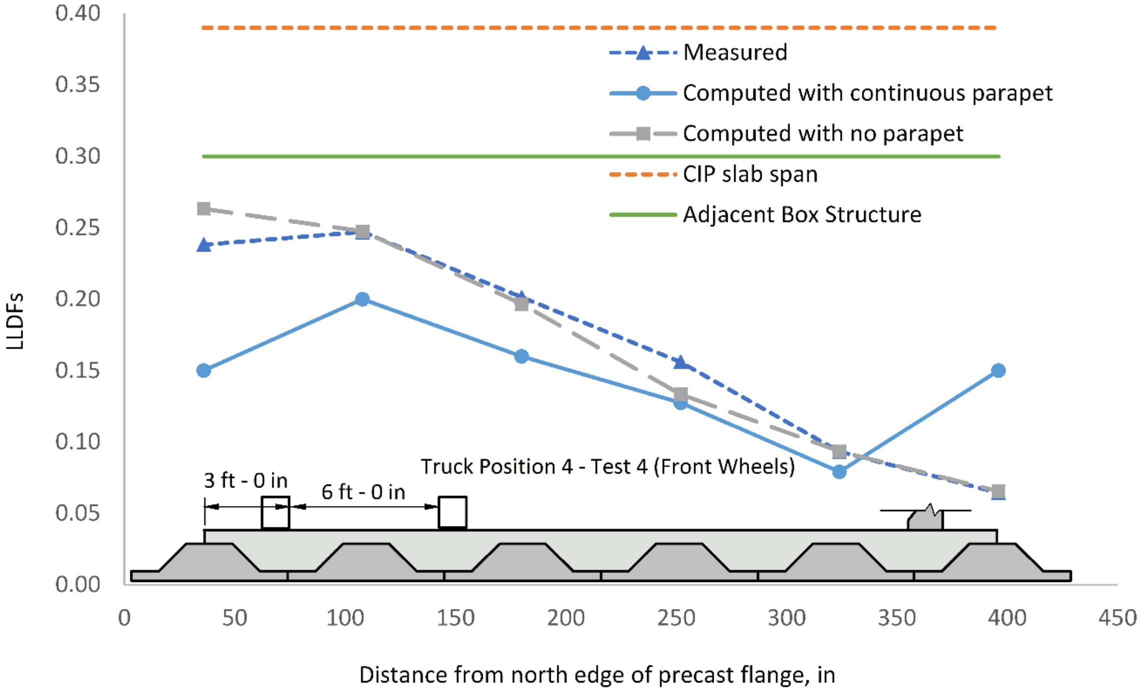

Figure 54. LLDFs in Each Girder – Truck Position 4

Table 11. Live Load Distribution Factors (Moment) – One Design Lane Loaded

	Adjacent Inverted T-beams with tapered webs				
Truck Position	**Measured**	**Computed with continuous parapet**	**Computed with no parapet**	**Cast-in-place slab spans**	**Adjacent voided/box structures**
1	NC*	0.25	0.22	**0.39**	**0.30**
2	0.22	0.32	0.22		
3	0.25	**0.45**	0.26		
4	**0.26**	0.26	**0.27**		

*****NC = not calculated because the last three gages recorded unreliable data

Note: Values in boldface are the maximum LLDF for moment for the given assumed structure type

Table 12. Live Load Distribution Factors (Moment) – Including Multiple Presence Effect

	Adjacent Inverted T-beams with tapered webs				
Truck Positions	**Measured**	**Computed with continuous parapet**	**Computed with no parapet**	**Cast-in-place slab spans**	**Adjacent voided/box structures**
1 + 4	NC*	0.41	**0.43**	**0.52**	**0.47**
2 + 4	**0.41**	0.44	0.41		
3 + 4	0.38	**0.58**	0.37		
Maximum LLDF x MPF^	0.31	0.54	0.32		

*****NC = not calculated because the last three gages recorded unreliable data

^MPF = Multiple Presence Factor

Note: Values in boldface are the maximum LLDF for moment for the given assumed structure type

multiple presence effect. The highest LLDF based on the measured response, without the consideration of the barrier rail, was 0.41 and was from the response with truck positions 2+4. The highest LLDF including the multiple presence effect for the computed responses was 0.43, and was based on the response without parapet for truck positions 1+4. LLDFs calculated based on AASHTO's methods assuming cast-in-place slab span and adjacent box structure behavior were 0.52 and 0.47, respectively.

Based on the measured and computed LLDFs, the design of composite bridges constructed with adjacent precast inverted T-beams with tapered webs can be designed based on AASHTO LLDFs calculated assuming cast-in-place slab span or adjacent box structure behavior. Although LLDFs for moment were higher in cases where the exterior beams were most heavily loaded, they were still lower than those calculated assuming cast-in-place slab span behavior. As stated earlier, the cast-in-place slab span method does not distinguish between an interior strip and an exterior strip and is therefore attractive because of its simplicity. In addition, in a completed bridge constructed with adjacent precast inverted T-beams and cast-in-place topping, the exterior beams are rectangular precast beams and the cast-in-place topping is extended to match the exterior face of the rectangular beam. Accordingly, the presence of these rectangular beams and the extension of the cast-in-place topping will provide additional load sharing capabilities for the precast inverted T-beams closest to the edge.

Because the simulated response obtained from the finite element models matched reasonably well with the measured response during the live load test, the finite element models were used to investigate additional cases in which the bridge was loaded with the controlled vehicle to create the maximum shear at the interior support. The investigation of these additional cases was required to determine whether different LLDFs for shear and moment are warranted as suggested by AASHTO's method for adjacent box structure system. The beam line model in RISA was used to determine the location of the controlled vehicle in the longitudinal direction that generates the highest vertical shear at the interior support. Once the position of the truck in the longitudinal direction was established, the 3D finite element models with and without the barrier were analyzed for the four truck positions used during the live load test. LLDFs for shear were calculated by dividing the interior reaction at each inverted T-beam by the sum of all interior reactions. Equation 29 presents the equation used for calculating LLDFs for shear. A summary of these LLDFs is provided in Table 13.

$$LLDF_i = \frac{R_i(n)}{\sum_{i=1}^{6} R_i} \qquad \text{Eq. 29}$$

where

R_i = vertical reaction at each inverted T-beam
$LLDF_i$ = Live Load Distribution Factor for each inverted T-beam

Table 13. Live Load Distribution Factors (Shear) – One Design Lane Loaded

	Adjacent Inverted T-beams with tapered webs			
Truck Position	**Computed with Continuous parapet**	**Computed with no parapet**	**Cast-in-place slab spans**	**Adjacent voided/box structures**
1	0.26	0.26	**0.39**	**0.50**
2	0.27	0.28		
3	0.33	0.33		
4	**0.35**	**0.34**		

Note: Values in boldface are the maximum LLDF for moment for the given assumed structure type

The maximum computed LLDFs for shear for one design lane loaded were 0.35 and 0.34 based on the model without and with the continuous barrier, respectively. The controlling truck position was again truck position 4 in which the exterior beams are loaded the most. LLDFs for shear are higher than those computed for moment (0.27) but still lower than the LLDFs calculated based on AASHTO's methods based on one design lane loaded.

To account for the multiple present effect, the reactions obtained from individual truck loading were superimposed for truck positions 1+4, 2+4 and 3+4. In addition, the maximum LLDFs for shear computed for one design lane loaded were multiplied by the multiple presence factor of 1.2 given in AASHTO as an alternative way to account for the multiple presence effect. The LLDFs are tabulated and presented in Table 14. The maximum computed LLDFs for shear including the multiple presence effect were 0.54 and 0.52 based on the model without and with the continuous barrier, respectively. Because the stiffness of the barrier rail cannot be counted on, only the LLDFs from the model without barriers are compared to AASHTO values. The maximum LLDF for shear with no barrier (0.52) is higher than the LLDF computed for moment (0.43), and also lower than the LLDFs calculated using AASHTO equations.

There is a noticeable difference between the two AASHTO methods for calculating LLDFs for shear. Because the method used for cast-in-place slab spans does not distinguish between LLDFs for shear and moment, the calculated LLDF for shear is the same as the one calculated for moment (0.52). If adjacent box structure behavior is assumed then the LLDF for

Table 14. Live Load Distribution Factors (Shear) – Including Multiple Presence Effect

Truck Positions	**Adjacent Inverted T-beams with tapered webs**		**Cast-in-place slab spans**	**Adjacent voided/box structures**
	Computed with Continuous parapet	**Computed with no parapet**		
1 + 4	**0.54**	**0.52**	**0.52**	**0.86**
2 + 4	0.48	0.48		
3 + 4	0.44	0.42		
Maximum LLDF x MPF^	0.42	0.41		

^MPF = Multiple Presence Factor

Note: Values in boldface are the maximum LLDF for shear for the given assumed structure type

shear is 0.86. These results suggest that the design of composite bridges constructed with adjacent precast inverted T-beams with tapered webs can be conservatively based on LLDFs calculated assuming cast-in-place slab span behavior. Even though the computed LLDFs for shear were slightly higher than those measured and computed for moment, this difference was not large enough to support AASHTO's method for adjacent box structure systems. A shear design using LLDFs for shear assuming adjacent box structure behavior would lead to overly conservative results.

Comparison of Phase I with the Completed Bridge and Other Bridges

The results presented in this section were based on field tests and analytical work conducted on Phase I of the U.S. 360 Bridge. It is reasonable to ask how these results can be related to the completed U.S. 360 Bridge and other bridges. Figure 55 shows transverse cross-sections of Phase I of the U.S. 360 Bridge, the completed U.S. 360 Bridge and Towlston Road Bridge constructed in Northern Virginia. The Towlston Road Bridge is the second application of the inverted T-beam system with tapered webs in Virginia and uses a simple-span, two-lane bridge.

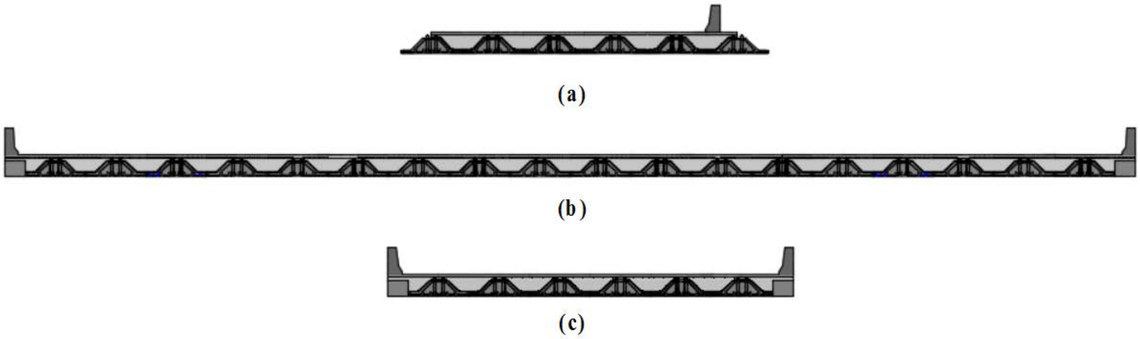
(a)

(b)

(c)

Figure 55. (a) Transverse Cross-Section of Phase I of the U.S. 360 Bridge, (b) Transverse Cross-Section of the Completed U.S. 360 Bridge, (c) Transverse Cross-Section of Towlston Road Bridge

Phase I of the U.S. 360 Bridge represents the least redundant superstructure from the stand point of being able to distribute live loads to the adjacent members. The difference between Phase I and the completed U.S. 360 Bridge is clear because the completed U.S. 360 Bridge features a greater number of beams, which can help share some of the applied truck loads. The Towlston Road Bridge is still more redundant than Phase I of the U.S. 360 Bridge, even though the number of precast inverted T-beams is the same, because it features two exterior rectangular precast beams, the cast-in-place topping is extended to match the exterior face of the rectangular beams and it includes two parapets. These additional features make the Towlston Road Bridge more redundant than Phase I of the U.S. 360 Bridge. Because the Towlston Road Bridge is a two-lane bridge it represents one of the narrowest applications in terms of bridge width for the inverted T-beam system.

Because other applications of the inverted T-beam system will feature bridges with at least two lanes, the conclusions drawn from the live load test conducted on Phase I of the U.S. 360 Bridge and simulations using finite element models can be conservatively applied to those cases.

CONCLUSIONS

Conclusions From Investigation Time-Dependent and Temperature Effects

- *Time-dependent and temperature effects can cause significant stresses in composite concrete bridge superstructures with precast inverted T-beams*.

- *Tensile stresses built-up due to time-dependent effects may be reduced if the concrete mix for the cast-in-place topping possesses low shrinkage and high creep properties*. While it is potentially onerous for the supplier to conduct creep tests for various mix designs, short-term shrinkage data (up to 28 days) is relatively simple to collect on a variety of mixes. This information will help the supplier create a database of shrinkage values for various mixes that could be used in future projects if the specifications require a mix with certain shrinkage parameters. The engineer of record can use one of the shrinkage models available in AASHTO or ACI 209 “Guide for Modeling and Calculating Shrinkage and Creep in Hardened Concrete” (ACI 209, 2008) to extrapolate the ultimate shrinkage strain based on strain data collected up to 28 days.

- *Compared to voided slabs and adjacent box girders, the inverted T-beam system reduces the tensile stresses in the cast-in-place topping caused by differential shrinkage by providing a smaller moment arm between the centroid of the cast-in-place topping and that of the precast beam*. (see Figure 8 and Figure 28).

- *The tapered webs of the precast inverted T-beams help to reduce the likelihood of deck cracking*.

- *Mild steel in the topping does not greatly influence the tensile stresses in the cast-in-place topping*. Mild steel does restrain free shrinkage and controls the cracking in the cast-in-place topping and helps distribute live loads in the transverse direction.

- *Accommodating longitudinal axial movement at the abutments of two-span continuous bridges reduces the tensile stresses due to differential shrinkage, negative temperature gradients and uniform decreases in temperature in the deck.*

- *The age of continuity between the inverted T-beams and the cast-in-place deck influences the amount of cracking in the deck*. The smallest likelihood of cracking occurs when the age of continuity is selected such that the competing effects of positive and negative restraint moment cancel each other as much as possible. High positive restraint moments negate the effects of negative live load moments and may render a continuous design even more expensive than a design based on simply supported beams. High negative restraint moments may result in excessive cracking on the bridge decks and reduce the service life of bridges. Although based on the analysis of a two-span continuous bridge with precast inverted T-beams, this conclusion generally applies to most types of composite bridges.

Conclusions From Investigation of End Zone Stresses

- *The precast inverted T-beams with tapered webs examined in this study that are 18 in deep or less do not require additional vertical reinforcing in the pretensioned anchorage zones*. The NCHRP method provided in French et al. (2011) may be used to evaluate the need for such reinforcing, while the AASHTO provisions (AASHTO, 2013) provide a conservative alternative for such beams.

- *For precast inverted T-beams with tapered webs that are deeper than 18 in, the vertical reinforcing in the end zones should be placed within a distance equal to h/4 from the end of the beam, or as close to end face as practically possible*. The distance *h* is the depth of the precast member. The magnitude of vertical tensile stresses at the end zones diminishes quickly past the first few inches from the end face, and the AASHTO provisions are conservative for these deeper sections. Vertical steel at the end zones can consist of stirrups as well as the vertical component of the AASHTO-required confinement steel.

- *Equation 27 is an appropriate method for determining the required reinforcing to resist bursting stresses that develop as the forces spread laterally.* The AASHTO required confinement steel can be used for this purpose given that this reinforcement needs to be provided for a distance up to 1.5*d* from the end of the member. In addition, the straight transverse bars in the precast flanges provided to resist the weight of wet concrete and transverse bending moments due to live loads can be also used to resist the bursting force. Alternatively, strut-and-tie models such as those shown in Figure 46 of this report can result in reinforcing requirements similar to those of Equation 27. The application of the 4% rule presented in AASHTO is not applicable for sizing reinforcing in the horizontal plane.

Conclusions From Live Load Testing

- *For inverted T-beam bridges with at least two lanes, AASHTO's method for calculating LLDFs for cast-in-place slab spans provides an acceptable upper bound for both moment and shear load distribution*. Assuming LLDFs for cast-in-place slab spans is attractive because of its simplicity and LLDFs for shear assuming adjacent box structure behavior are unnecessarily conservative.

- *The calculated LLDFs for moment and shear for exterior beams tend to be higher than interior beams under similar loading conditions*.

- *Regardless of exterior or interior location, the LLDFs for shear are higher than those calculated for moment.*

RECOMMENDATIONS

1. *VDOT's Structure and Bridge Division should use the recommendations for vertical end zone reinforcement presented by French et al. (2011) to design the vertical end zone reinforcement in inverted T-beams.* If analysis indicates that vertical reinforcing is needed, that reinforcement should be placed within a distance equal to *h/4* from the end of the beam, where *h* is the depth of the precast member, or as close to end face as practically possible. The reason is that spalling stresses at the end face are the dominant type of tensile stresses in terms of magnitude.

2. *VDOT's Structure and Bridge Division should use Equation 27 to size the reinforcing in the horizontal plane of pretensioned anchorage zones of precast inverted T-beams with tapered webs.* Using Equation 27, the horizontal reinforcing should be uniformly distributed within a distance *h* from the end of the precast flange. If using an alternative strut-and-tie model, the horizontal reinforcing should be distributed uniformly throughout the disturbed region.

3. *VDOT's Structure and Bridge Division should use LLDFs for moment and shear based on assuming cast-in-place slab span system behavior.*

4. *The Virginia Transportation Research Council should support additional research to determine the best arrangement and alignment of the reinforcement for skewed bridges.*

BENEFITS AND IMPLEMENTATION

Benefits

Full-depth cracks in traditional adjacent member systems such as box beams or voided slabs allow water and deicing salts a direct path to the underside of the bridge, where they can cause early initiation of corrosion in the prestressed beams. The benefits of the inverted T-beam system are improved durability compared to these traditional adjacent member bridges. The cast-in-place topping over the joint between the inverted T-members is deeper and more heavily reinforced than in the traditional systems. Therefore, if a crack does develop at the joint at the bottom of the cross-section, it is far less likely to propagate to the surface and result in a full-depth crack. Also, in particular, the tapered web cross-section studied in this research will be less prone to restrained shrinkage compared to an inverted T-beam with vertical webs.

As for the recommendations ensuing from the conclusions from this research, *Recommendations 1* and *2* will result in a savings of material and reduction in fabrication time, thus resulting in lower costs to build a bridge. The preferred live load in *Recommendation 3* will allow for the economical design of the inverted T-beam system, yet provide sufficiently conservative factors that will ensure the durability of the system. The knowledge gained from *Recommendation 4* will allow bridge engineers to use the inverted T-beam design in more projects beyond those bridges with no skew, thus enhanincing the overall durability of structures in VDOT's inventory.

Implementation

The inverted T-beam system has already been used in the Route 360 Bridge and the Towlston Road Bridge. This study provided the foundation for the development of VDOT standards for this type of system.

VDOT's State Structure and Bridge Engineer and his staff oversaw the implementation of *Recommendations 1* through *3* in terms of the development of standard design details and any associated special provisions (with assistance from Virginia Tech) for incorporation into the VDOT Structure and Bridge Manual for span lengths of 20 ft to 45 ft. These standards are now complete.

With regard to *Recommendation 4*, a follow-on study has already been initiated in conjunction with *Recommendation 8* from Part I of this report, which called for additional research to determine if the non-contact lap splice connection could be used on bridges with high volumes of truck traffic. The anticipated completion date for that study is January 2019.

ACKNOWLEDGMENTS

The authors gratefully acknowledge the guidance and assistance of Michael Brown and Bernie Kassner of the Virginia Transportation Research Council and Andy Zickler and Chris Lowe of VDOT's Structure and Bridge Division. The assistance of Matt Mercer, Doug Nelson, Kedar Halbe, Carrie Field, David Mokarem, Brett Farmer, and Dennis Huffman in the field and at the Murray Structural Engineering Laboratory at Virginia Tech is gratefully acknowledged. The opinions in this report are those of the authors and not necessarily those of the sponsor.

REFERENCES

American Association of State Highway and Transportation Officials. *AASHTO LRFD Bridge Design Specifications 6th Edition*. Washington, DC, 2013.

ABAQUS. *User's Manual Version 6.11-2*. Dassault Systemes Simulia Corp., Johnston, RI, 2012.

ACI Committee 209. *Guide for Modeling and Calculating Shrinkage and Creep in Hardened Concrete*. American Concrete Institute, Farmington Hills, MI, 2008.

Base, B.D. *An Investigation of Transmission Length in Pre-tensioned Concrete*. Research Report No. 5. Portland Cement Association, Chicago, IL, 1958.

Bell, C., Shield, C.K., and French. C.W. *Application of Precast Decks and Other Elements to Bridge Structures*. MN/RC 2006-37. Minnesota Department of Transportation, Saint Paul, 2006.

Dimaculangan, M.C., and Lesch, T. Minnesota's Precast Composite Slab Span System. *Aspire,* Summer 2010.

Fountain, R.S. *A Field Inspection of Prestressed Concrete Bridges.* Portland Cement Association, Chicago, IL, 1963.

French. C.W., Shield, C.K., Klasesus, D. Smith, M., Eriksson, W., Ma, J.Z., Zhu, P., Lewis, S., and Chapman, C.E. *Cast-in-Place Concrete Connections for Precast Deck Systems*. NCHRP Web-Only Document 173. Transportation Research Board, Washington, DC, 2011.

Freyermuth, C. Design of Continuous Highway Bridges with Precast, Prestressed Concrete Girders. *PCI Journal,* Vol. 14, No. 2 , April 1969, pp.14-39.

Gergely, P., Sozen, M.A., and Seiss, C.P. *The Effect of Reinforcement on Anchorage Zone Cracks in Prestressed Concrete Members.* Structural Research Series No. 271. University of Illinois, Urbana- Champaign, IL, 1963.

Gilbert, R.I. *Time Effects in Concrete Structures.* Elsevier, Amsterdam, The Netherlands, 1988.

Hagen, K., Ellis, S., Fishbein, J., Molnau, K., Wolhowe, E., and Dorgan, D. Development and Construction of a Precast Inverted T System for Expediting Minnesota Slab Span Bridge Projects. In *Proceedings of the PCI 2005 National Bridge Conference,* Palm Springs, CA, October 16-19, 2005.

Halverson, M., French. C., Shield, C. *Full-Depth Precast Concrete Bridge Deck System: Phase II.* MN/RC 2012-30. Minnesota Department of Transportation, Saint Paul, 2012.

Hawkins, N.M., and Shahawy, M. *Anchorage Zone Stresses in Prestressed Concrete Beams.* Structural Research Series No. 207. University of Illinois, Urbana- Champaign, IL, 1960.

Hill, J.C., and Lowe, C.M. *Route 360 Over Chickahominy River Bridge Replacements Hanover/Henrico Counties, Richmond District State Project 0360-964-120, B601, B606, B607& B608 - Federal Structure Identification Numbers 9469, 10014, 10015, 10016 UPC Number 17959 - Preliminary Structure Report, Plans and Estimates*. Virginia Department of Transportation, Structure & Bridge Division, Richmond, May 3, 2010.

Love, A.E.H. *A Treatise on the Mathematical Theory of Elasticity.* Cambridge University Press, Cambridge, UK, 1927.

Mattock, A. Precast-Prestressed Concrete Bridges 5: Creep and Shrinkage Studies. *Journal of the PCA Research*, May 1961, pp. 32-66.

Menkulasi, F., Cousins, T.E., Roberts-Wollmann, C.L. *Implementation of a Precast Inverted T-Beam System in Virginia: Part I: Laboratory Investigations*. VTRC 18-R7. Virginia Transportation Research Council, Charlottesville, 2017.

Menn, C. *Prestressed Concrete Bridges*. Translated and edited by Paul Gauvreau. Birkhauser, Verlag, Basel, Switzerland, 1990.

Oesterle, R., Glikin, J., and Larson, S. *Design of Simple-Span Precast Prestressed Bridge Girders Made Continuous (Final Report).* Construction Technology Laboratories, Inc., Skokie, IL, 1989.

Peterman, R.J., and Ramirez, J.A. Restraint Moments In Bridges with Full-Span Prestressed Concrete Form Panels. *PCI Journal,* Vol. 43, No. 1, January-February 1998, pp. 54-73.

Ralls, M.L., Tang, B., Bhide, S., Brecto, B., Calvert, E., Capers, H., Dorgan, D., Matsumotos, E., Napier, C., Nickas, W., and Russell, H. *Prefabricated Bridge Elements and Systems in Japan and Europe.* FHWA-PL-05-003. Federal Highway Administration, Washington, DC, 2005.

Smith, M., Erikkson, W., Shield, C., and French, C. Field and Laboratory Study of the Mn/DOT Precast Slab Span System. In *Proceedings of the 2007 Mid-Continent Transportation Research Symposium,* Ames, Iowa, August 2007.

Smith, M.J., Eriksson, W.D., Shield, C.K., and French, C.W. *Monitoring and Analysis of Mn/DOT Precast Composite Slab Span System (PCSSS)*. MN/RC 2008-41. Minnesota Department of Transportation, Saint Paul, 2008.

Uijl, J.A. *Tensile Stresses in the Transmission Zones of Hollow-Core Slabs Prestressed with Pretensioned Strands*. Report 5-83-10. Delft University of Technology, Department of Civil Engineering, The Netherlands, 1983.